Title

High Resolution Permittivity Sensing in THz CMOS Technology

Author

Yu, Hai

Publication Date

2024

Peer reviewed|Thesis/dissertation

High Resolution Permittivity Sensing in THz CMOS Technology

By

Hai Yu

DISSERTATION

Submitted in partial satisfaction of the requirements for the degree of

DOCTOR OF PHILOSOPHY

in

ELECTRICAL AND COMPUTER ENGINEERING

in the

OFFICE OF GRADUATE STUDIES

of the

UNIVERSITY OF CALIFORNIA

DAVIS

Approved:

Qun Jane Gu, Chair

Anh-Vu Pham

J. Sebastian Gomez-Diaz

Committee in Charge

2024

Contents

Abstract

Permittivity sensing has wide applications in a variety of industries such as petroleum, agriculture, food production, etc.. The complex permittivity serves as an effective indicator of the valuable information of the sample material such as their constitute, moisture or quality, which are critical in the process of product development, production, and treatment. The nondestructive nature of the permittivity sensing makes it highly cost-effective and enables it for real time material characterization. This calls for the adoption of CMOS technologies to achieve a high level of integration of signal processing capabilities for cost-effective and ubiquitous applications without sacrificing precision and accuracy. Therefore, numerous works featuring CMOS permittivity sensor have been developed. Among all aspects of CMOS permittivity sensing systems, high resolution sensing is of particular importance, which enables CMOS sensing in applications such as high precision biosensing, precision medicine, etc. High resolution sensing enables high throughput measurement, capturing fast process in real time, etc. To achieve high resolution, the prior art focuses on two key aspects: permittivity sensor's sensitivity boost and system noise reduction.

In the optical community, ultra-high sensitivity is achieved by utilizing resonator based sensors, whose resonant frequency is shifted by the permittivity of different MUT's. Sharp curvature and steep slope of the transmission coefficient of the high Q resonator sensors result in high sensitivity. Whispering gallery mode (WGM) resonators show particularly high sensitivity due to its high Q and the strong field interaction with the MUT's. However, the expensive and bulky tunable optical sources and the limited signal processing and readout capabilities severely constrain the applications of the high sensitivity optical sensors.

To advance the state of the arts of the high resolution permittivity sensors, this dissertation dedicates to the theory, design and implementation of sub-THz WGM resonator based CMOS permittivity sensor. Thanks to its short wavelength, the WGM resonator sensor at sub-THz possesses a compact form-factor, achieving a high level of integration with the CMOS transceivers (TRX). Like its optical counterparts, the compactness of the sub-THz sensor also enables high sensitivity detection while requiring a smaller amount of MUT samples than sensors working at GHz frequency range. The CMOS TRX generates the sub-THz signal to excite the WGM sensor and readout the signal to obtain the permittivity information.

The dissertation analyzes the EM mechanisms of the WGM resonator sensor, including the loss analysis and coupling condition analysis, lays theoretical foundations for the sensitivity optimization for high resolution sensing. A novel mechanism to detect complex permittivity using the WGM resonator sensor is proposed for the first time in the permittivity sensing and resonator sensor community. A low power permittivity sensing system at 160 GHz is prototyped to verify the permittivity sensing capability of the WGM resonator sensor integrated with the CMOS TRX IC, which demonstrates a permittivity sensing resolution of 0.098 for a integration time of 10 us with a power consumption of only 9 mW. A high resolution complex permittivity sensing system at 160 GHz is implemented that adopts a band-stop WGM disk resonator based sensor structure and multi-fold noise suppression techniques, which demonstrates a record of 0.05% complex sensing resolution within 14-us integration time and consumes 54 mW of DC power.

In the process of designing the high resolution permittivity sensing system, mathematical derivations are developed to predict the noise suppression effect of the three noise reduction techniques: the phase noise suppression by the coherent phase noise cancellation, the flicker noise suppression by the chopping scheme and the thermal noise suppression by the integrator. Since these three noise reduction techniques are commonly used in sensing / imaging systems, the developed derivation in this dissertation can be readily applied to predict the noise suppression effect numerically and to guide the design of the noise reduction circuitry.

Acknowledgments

I would like to thank my advisor Prof. Jane Gu for her consistent support and valuable advice throughout my Ph.D. journey. Her dedication, persistence and experience are enormously helpful for the work that we forged together.

I would like to thank the committee members of my dissertation, Prof. Anh-Vu Pham and Prof. Juan Sebastian Gomez-Diaz for taking their time to review my dissertation. I would like to sincerely thank Prof. Pham for his kind support and precious advice on my research project since the qualifying exam. I am also grateful for the precious guidance from Prof. Gomez-Diaz in the early stage of my project and helped set the tones for my later projects.

I would like convey my deep thank to Prof. Neville C. Luhmann Jr. for his priceless support in my hard time. I would like to thank Prof. Omeed Momeni and Prof. Dong Yu in the Physics department for their valuable advice. I would like to thank Ms. Lynette Lombardo for her warm care and coordination, and Dr. Calvin W. Domier for his kind assistance when we borrow equipment.

I would to thank Mr. Ryan Anderson, Dr. Chan Ho Kim, Dr. Yusha Bey, Dr. Siwei Li, Dr. Vishal Narang and Ms. Paula Lee for their valuable help in the CNM2. I would also like thank Prof. Mani Tripathi, Prof. Dong Yu, Bob Wang in the Physics Department for generouly granting the access to the flip-chip equipment and wire bonders for my sensing system packaging. I would like to thank Minji Zhu in CHFE UCLA for the sensor packaging.

I would like to express my sincere gratitude to the senior colleagues in our research group, Shilei Hao, Bo Yu, Jinbo Li, Tongning Hu, Xuan Ding. Their priceless advice and generous help facilitates my research progress in a indispensable way. I would like also thank my colleague Sajjad Sabbaghi, Zahra Mohseni for their assists for my research. I would like to express my special thank to Dr. Jingjun Chen, with whom I have valuable technical discussions over time and his kind assistance in the dissertation work. I would also like to thank my good friends and colleagues from our department Jo-Han Yu, Ying Chen, Xianzi Liu, Shasha Qiu, Hao Wang, Li Zhang, Xiaonan Jiang, Hao Wang, Cheng Li, Saleh Hassanzadehyamchi, Hamidreza Afzal, Can Cui, Nguyen Nguyen, Hemin Wu, Sicong Feng, for valuable technical discussions and supports as comrades thrusting towards our common goals.

I would also like to thank my close friends outside of the ECE department, Shunyang Wang, Jiahui Wei, Zimin Zheng, Dongjie Chen, Wentao Guo, Mingyang Zhou, Chao Wan for enriching my personality and maintaining a barely balanced life.

List of Figures

CHAPTER 1

Introduction

1.1. Permittivity Sensing

Permittivity is an important property of a dielectric material, describing the material's interaction with the electric field inside and around it. One of the most universal origins of the permittivity property of a material is the electrically polarized and bounded particles that constitute the dielectric material, as shown in FIGURE 1.1. These particles respond to externally applied electric field and stores and dissipates electric energy during the process.

A dielectric material's permittivity ϵ is generally complex, which can be expressed as

$$\epsilon = \epsilon' - j\epsilon''. \tag{1.1}$$

The real part ϵ' corresponds to the material's capability of storing electric field, and the imaginary part ϵ'' corresponds to the material's loss [**3**]. To simplify analysis numerically, permittivity can be normalized by free space permittivity ϵ_0, resulting in relative permittivity ϵ_r

$$\epsilon \equiv \frac{\epsilon}{\epsilon_0} = \epsilon_r' - j\epsilon_r'' \tag{1.2}$$

As a macroscopic description of material properties, permittivity's ties to numerous microscopic processes can give important information of the material under test, such as material type, purity, humidity, temperature, quantity, etc. In addition, these processes also make permittivity depend on the frequency of the externally applied electric field if the field is alternating with time. This gives different materials their permittivity spectral fingerprint. Consequently, permittivity sensing has wide application in various fields including material or mixture identification, biomedical examination, agriculture, production control, etc. [**4**].

In general, permittivity sensing system comprises three parts – signal generator, sensor and readout equipment. The signal generator excites the sensor with electromagnetic field so that the

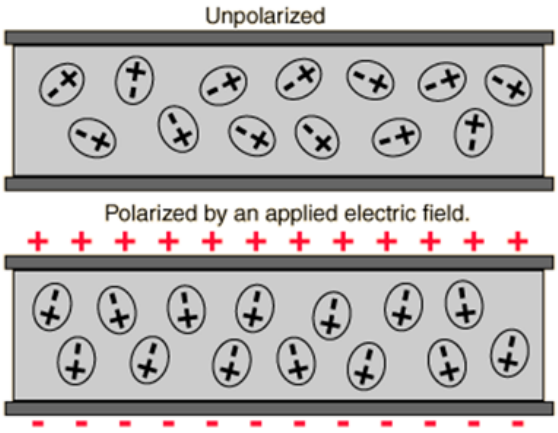

FIGURE 1.1. Mechanism and origin of permittivity of dielectric materials.

field can interact with the material under test (MUT) at the sensor. Thereby, the sensor transduces the permittivity of the MUT to some forms of electrical signal, be it change of intensity, time delay or frequency response, etc. Finally, the readout equipment receives the altered signal due to the field-matter interaction at the sensor and converts it to signals that are easy to display, process and store. To achieve high precision measurement, it is required to have low noise excitation from the signal generator, high sensitivity sensor, and low noise readout equipment. More specifically, for a sensor that transduces MUT permittivity to a certain electrical signal s to be detected by the readout equipment, the measurement precision of a sensing system can be evaluated by permittivity sensing resolution, which is the minimum detectable permittivity change for the sensing system, defined as

$$\delta_\epsilon = \frac{\delta_s}{Sen_s}. \tag{1.3}$$

δ_s is the minimum detectable signal s for the readout equipment, determined by the noise performance of the readout equipment. Sen_s is the sensitivity of the sensor, which is defined as the amount of s change due to unit permittivity change of the MUT loaded on the sensor

$$Sen_s \equiv \frac{\partial s}{\partial \epsilon}. \tag{1.4}$$

From Eqn. 1.3, in order to have good permittivity sensing resolution δ_ϵ, it is beneficial to have high sensitivity sensor and low noise readout equipment. Therefore, in order to improve sensing

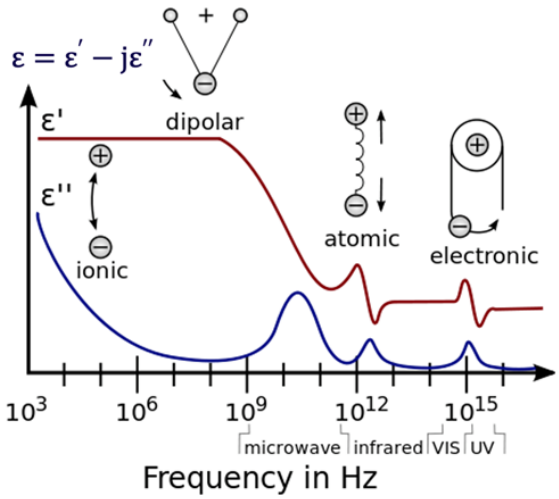

FIGURE 1.2. The frequency dependence of permittivity due to various microscopic processes in dielectric materials.

resolution, research efforts are being focused on these two aspects, regardless the mechanism or architecture of the various sensing systems. Existing permittivity sensing systems can be categorized in two types based on their working frequencies – optical sensing based on optical systems and radio frequency (RF) sensing based on electrical systems. They will be introduced and discussed in the following subsections.

1.1.1. Optical Permittivity Sensing. The earliest permittivity measurement can be traced back to the light refraction experiments. Through the study of light dispersion, it is observed that light's dispersion depends on the permittivity of the medium (or refractive index in optical terminology). Hence optical is naturally the most developed field of permittivity sensing and measurement. Combining with optic fiber technology, today's optical permittivity sensor achieves dominant sensing resolution thanks to its low loss resonators. Numerous optical devices are utilized as sensor, such as optic fiber, ring resonator and whispering gallery mode (WGM) sensors [**5**] [**6**] [**7**]. The record-keeping optical sensors are based on optical resonators [**8**] [**9**] [**10**] [**11**] [**12**]. An optical resonator's resonant frequency depends on the permittivity of the surrounding medium. A typical optical resonator sensor is shown in FIGURE 1.3, an optical spherical resonator coupled to a tapered optical fiber [**13**]. The intensity of the light transmission has a valley at resonance wavelength λ_r, and the resonant wavelength, or equivalently the resonant frequency shifts when analyte is

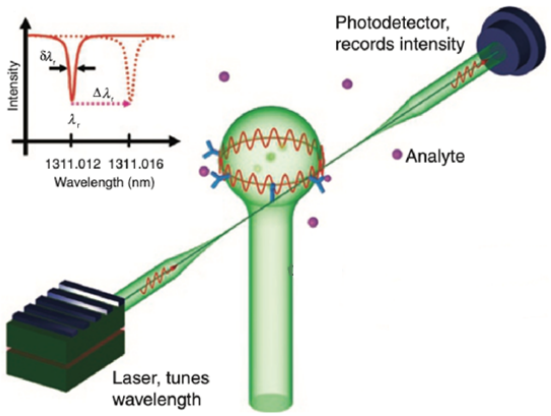

FIGURE 1.3. Whispering gallery mode resonator based optical sensor.

captured by the accepters pretreated on the resonator surface as a disturbance to its permittivity environment. $\delta\lambda$ denotes the full width half maximum of the resonance, which is determined by the loss of the resonator. The lower the loss, the smaller $\delta\lambda$ reduces to. Extremely small frequency shift can be detected if $\delta\lambda$ is small enough. The low loss optic fiber technology enables very narrow resonance, namely small $\delta\lambda$, hence low detection limit. [**8**] reports a sensing resolution to the order of $1 \times 10^{-7}\ \epsilon_r'$ from a microsphere resonator. [**14**]] reports a resolution of 1×10^{-6} using optical coupler as a sensor. [**9**] [**10**] [**11**] [**12**] achieve resolutions of $10^{-3} - 10^{-6}$with ring resonator sensor. However, optical sensing system requires bulky light source and detector. In addition, readout device needs to convert optical signal to electrical signal for processing. These drawbacks limit the wide deployment of optical permittivity sensors.

1.1.2. Electrical Permittivity Sensing. As another well-developed field, radio frequency and microwave engineering provide mature platform for permittivity measurement. Moreover, permittivity is a very relevant parameter of substrate and media in RF design. These gives strong motivation to permittivity measurement at RF frequencies. Also, based on complementary metal-oxide semiconductor (CMOS) technology, recent decades of RF integrated circuit (RFIC) development gives electrical sensing systems further advantages in terms of cost and size in addition to performance enhancement [**4**]. Sophisticated sensing system integrated on small silicon chips are suitable to be applied in various industries and fields. Consequently, CMOS electrical permittivity sensing has been a popular research area in the recent decades.

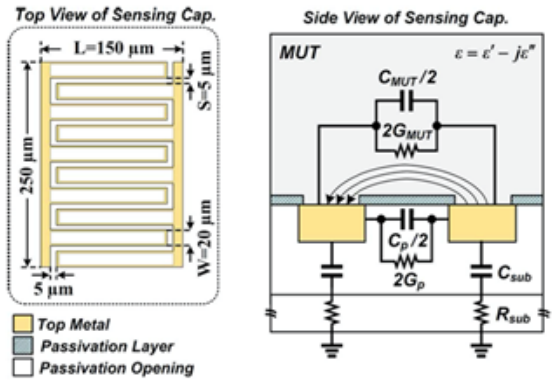

FIGURE 1.4. Integrated capacitor of VCO as sensing element.

One important category of existing sensing system is voltage-controlled oscillator (VCO) based [**15**] [**16**] [**17**] [**18**]. This type of sensing system merges the signal generator and sensor as one. The interdigit capacitor in the VCO serves as the sensor. The MUT will be put on top of the interdigit capacitor. Its capacitance is then a function of the MUT permittivity "felt" by the fringing field between the capacitor's fingers, as shown in FIGURE 1.4. Thus, the increase of MUT permittivity will increase VCO's capacitance, resulting in lower oscillating frequency. This mechanism applies to LC VCO [**15**] [**16**] [**18**] as well as ring VCO [**17**]. The oscillation frequency will then be detected by a frequency discriminator.

Unlike VCO-based sensing systems, other sensing systems have standalone sensors. The sensors take forms of capacitor, transmission structure, or resonance structure. Capacitor's admittance varies with external permittivity and therefore can be detected [**19**]. Transmission structures such as co-planar waveguide (CPW) have advantage of broadband sensing [**20**]. Resonant structures such as split-ring resonator have advantage of increased sensitivity at cost of narrowed bandwidth [**21**] [**22**]. The sensitivity increase is based on an enhanced field-matter interaction boosted by a factor of Q. Q is the quality factor of the resonator, describing the loss of the resonance

$$Q = 2\pi \times \frac{energy\ stored}{energy\ dissipated\ per\ cycle} \tag{1.5}$$

Hence higher Q increases effective field-matter interaction [**9**].

Despite the versatility given by the RFIC development, electrical sensing at radio frequency has mediocre sensing resolution due to the lack of high sensitivity sensors. This is because, unlike

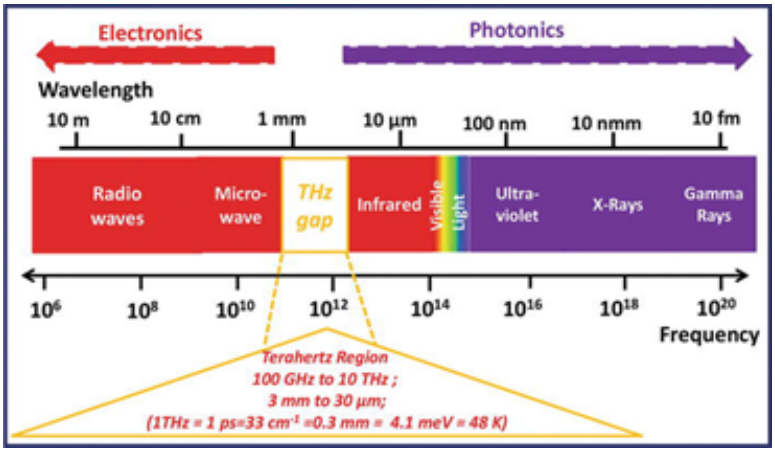

FIGURE 1.5. Terahertz frequencies on the EM spectrum.

optical resonators, conventional metal-insulator-metal microwave resonators suffer from higher loss. Low loss resonators such as ring resonator has large dimensions at radio frequency, defeating the advantage of compactness given by RFIC.

1.1.3. Sub-THz/THz Circuit and Systems. Terahertz (THz) frequencies sit between the optical and radio frequency frequencies, as shown in FIGURE 1.5. A unanimous definition for THz frequency range has not yet been reached. The strictest definition is 300 GHz – 3 THz, delimited by the upper operating frequency of WR-3 waveguide [**23**]. Hence academic often refers frequencies of 100 GHz – 300 GHz as sub-THz. Historically, sub-THz and THz are less used frequency range. Its energy is too low for photonic generation, but too high for electronic generation, therefore the name THz gap. However, recent millimeter-wave development in RFIC has been gradually filling the gap [**24**] [**25**] [**26**] [**27**] [**28**] [**29**] [**30**] [**31**] [**32**]. The small wavelength and compatibility to powerful CMOS technology gives sub-THz sensing systems unique advantages. [**33**] developed a reflection-based measurement setup to measure the permittivity of material in sub-THz frequency range. [**22**] made this solution integrated on a chip, utilizing the small wavelength of sub-THz signal. Further, [**34**] built a complete vector network analyzer for permittivity sensing on a single chip. However, the potential of sub-THz sensing is still far from being utilized. Like its successful optical counterpart, high quality but compact sensor can be realized in sub-THz to achieve extremely high sensitivity and therefore resolution. This makes sub-THz sensor a strong candidate to fill the sensing resolution gap between optical sensor and existing electrical sensor, as shown in FIGURE

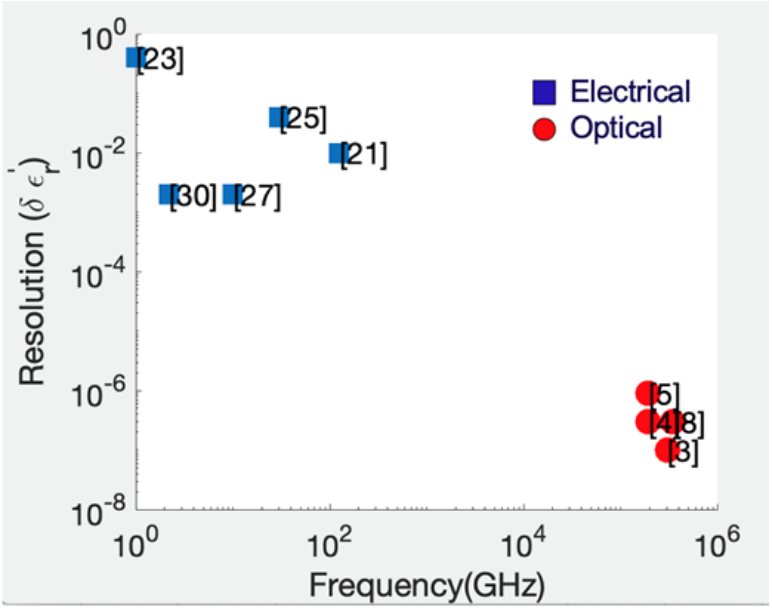

FIGURE 1.6. Sensing resolution of record optical and electrical sensors.

1.6. FIGURE 1.7 below summarizes the features of permittivity sensor at RF, optical and sub-THz. Based on the foregoing study, we propose a CMOS permittivity sensing system based on sub-THz resonator sensor. The following chapters will discuss in detail the resonator sensor and sensing system design in order to fully utilize the unique advantages of sub-THz permittivity sensing.

1.2. Dissertation Outline

This dissertation is organized as follows. Chapter 2 presents the fundamental EM theories of the WGM resonator sensor and the DWG platform upon which it is built. The fundamental loss and coupling mechanisms are discussed in detail.

Chapter 3 proposes a high sensitivity WGM disk resonator sensor structure, to be integrated in a high resolution complex permittivity sensing system with CMOS TRX. The complex sensing capability and the corresponding mechanism of the sensor are illustrated in detail. The optimization of its sensitivity, and its detailed design, implementation, fabrication and packaging procedures are also presented in this chapter.

Chapter 4 proposes a low power permittivity sensing system at 160 GHz. It features a band-pass WGM ring resonator based sensor integrated with CMOS TRX operating at 160 GHz. The sensing system can detect permittivity difference as small as 3×10^{-10} for a integration time of 10 us with

Sensing system	Resolution	Form Factor	Cost
Optical	very high	medium	medium
RF	medium	small	low
THz	high	very small	low

FIGURE 1.7. Sensing resolution of record optical and electrical sensors.

a power consumption of only 9 mW.

Chapter 5 proposes a high resolution complex permittivity sensing system at 160 GHz. It adopted a band-stop WGM disk resonator based sensor structure presented in Chapter 3. The TRX adopts multi-fold noise suppression techniques implemented in novel architecture, which enables a high SNR at the output of the system. The sensing system demonstrates a 0.05% complex sensing resolution within 14-us integration time and consumes 54 mW of DC power.

Chapter 6 draws conclusions for this dissertation and lays out possible direction for future work.

CHAPTER 2

Fundamentals of Sub-THz Whispering Gallery Mode Resonator Sensors

In this chapter, the fundamentals of the sub-THz WGM resonator sensors are introduced. Firstly, the rectangular dielectric waveguide which serves as the underlying platform for the resonator sensor, is introduced. Secondly, the operation of the WGM and its fundamental sensing mechanism as a permittivity sensor are presented. Then, the theory of the coupling between the resonator and the DWG and the loss mechanism of the resonator is presented. Finally, investigations that explore the different forms of the sensor to determine the optimal configuration that can achieve the highest possible permittivity sensitivity are summarized at the end of this chapter.

2.1. Dielectric Waveguide

In frequencies of sub-THz and above, dielectric waveguide is a good candidate for low loss signal transmission [**1**] [**35**]. In both [**1**] and [**35**], high-resistivity silicon is used as the the waveguide material due to its performance in terms of low attenuation constant and easiness of fabrication. More particularly, [**1**] developed a waveguide of high quality signal transmission based on a high-resistivity (HR) silicon, whose resistivity is $10,000\Omega \cdot cm$. The high resistivity ensures the low dielectric loss of the waveguide, and its loss tangent $tan\delta$ is determined to be 0.001 by comparing the simulation results and the measurement result. The electromagnetic waves are bounded and guided in the waveguide by total internal reflection at the side walls. The cross-section height $H = 500um$ and width $W = 300um$ are determined from EM simulation such that the waveguide transmits the E_{11}^{y} mode most effectively, as shown in FIGURE 2.1. And the mode E_{11}^{y} is chosen because its low loss transmission in the dielectric waveguide and easiness of coupling and excitation. The relatively high permittivity of silicon improves the EM field confinement, and thus further reducing propagation loss. Furthermore, easy access of the HR silicon wafer from the market and

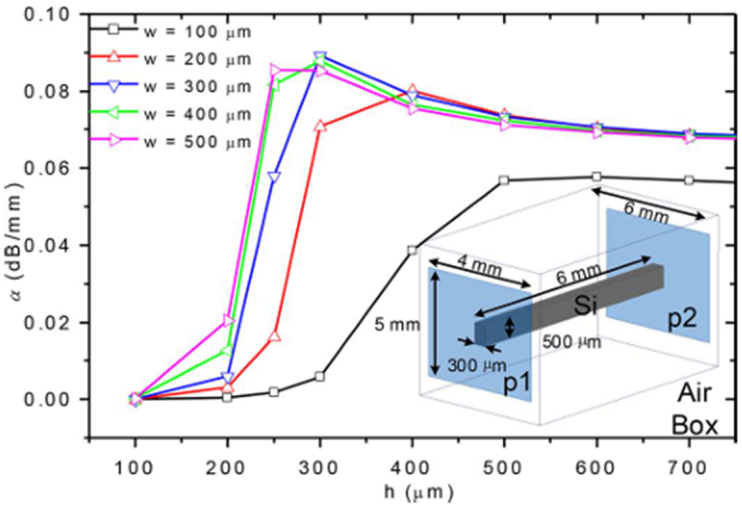

FIGURE 2.1. The attenuation coefficient of the DWG vs. the height of the waveguide with the HFSS simulation setup (p1 and p2 are wave ports) [**1**].

the mature process of silicon etching also suggests the adoption of this type of the waveguide in the permittivity sensing application.

The propagation of the sub-THz EM wave is chosen to be one of the fundamental mode of E_{11}^{y} because of the easiness of its excitation. The vertical polarization of the E_{11}^{y} mode makes microstrip line a natural candidate of excitation transmission line of the rectangular DWG. After all, sub-THz EM wave needs to be fed into the DWG via an effective coupling method to have low insertion loss as well as low return loss. [**2**] develops such a microstrip transition. The fundamental mechanism of such a transition is to match the impedance between the microstrip line and the DWG. From EM simulation, the wave impedance of the E_{11}^{y} mode propagating in the DWG of the dimension of $300um \times 500um$ is around 150Ω, and a smaller width results in lower wave impedance [**2**]. On the other hand, a 50Ω microstrip line is tapered to narrower width to increase its characteristic impedance to match that of the DWG. The DWG is placed over the tapered section of the microstrip line, where the vertical E field of the microstrip line couples to the tapered section of the DWG, as shown in FIGURE 2.2. This type of microstrip-to-DWG transition is easy to fabricate due to its planar structure and has a relatively low loss of 1.4 dB. Therefore, it is adopted in various DWG applications [**36**] [**37**] to enable chip-to-DWG communication. Based on the theory of this transition design, an improved co-planar waveguide (CPW)-to-DWG transition, which is more compact and

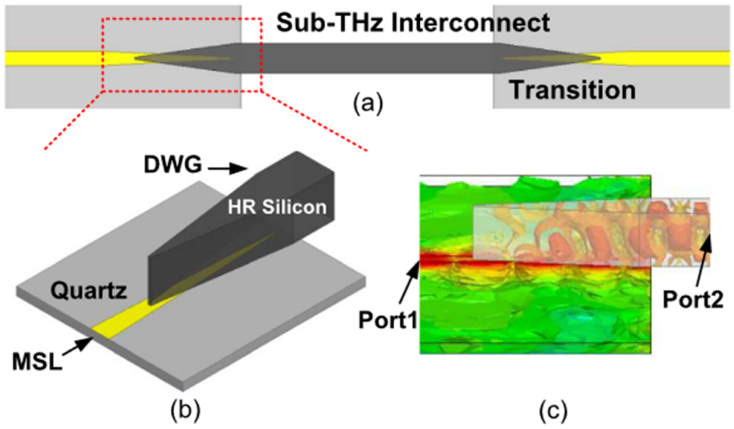

FIGURE 2.2. (a) Top view of the DWG with transition to MSL, (b) perspective view of the transition, (c) the magnitude of E-field distribution of the transition. [**2**]

easier to fabricate, is also developed and is discussed in detail in Section 3.4.1.

The rectangular dielectric waveguide cross section and geometries are shown in FIGURE 2.3. Region 1 is the core of the dielectric waveguide, with high relative permittivity, $\epsilon_{r,1} = 11.7 - j0.012$ in this work. Region 2 is the left and right side region of the waveguide, which is air in this design, with relative permittivity of $\epsilon_{r,2} = 1$. Region 3 is the top and bottom region of the waveguide with relative permittivity of $\epsilon'_{r,3}$. The electromagnetic field distribution of the E^y_{11} mode are shown in Fig. 3. k_x and k_y are the wave numbers of the mode in x and y directions, respectively. α_x and α_y are the attenuation coefficient of the evanescent fields that extend to the exterior or cladding regions of the waveguide due to the total internal reflection of the propagating wave inside the waveguide. The relations of the propagation coefficients are bounded by

$$\begin{cases} -k_x^2 - k_y^2 + k_0^2\epsilon'_{r,1} - \beta^2 = 0, \ \textit{Region 1} \\ \alpha_x^2 - k_y^2 + k_0^2\epsilon'_{r,2} - \beta^2 = 0, \quad \textit{Region 2} \\ -k_x^2 + \alpha_y^2 + k_0^2\epsilon'_{r,3} - \beta^2 = 0, \ \textit{Region 3} \end{cases} \tag{2.1}$$

where k_0 is the wave number of the plane wave in vacuum and β is the propagation constant of the guided wave or the wave number in z direction. Eqn. 2.1 is the controlling theory that determines the coupling between the waveguide and the WGM resonator and the fundamental permittivity

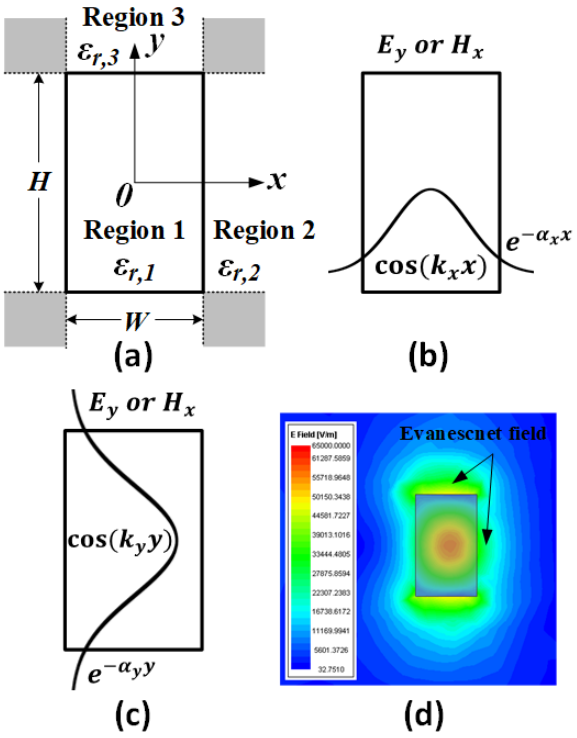

FIGURE 2.3. Dielectric waveguide (a) Cross-section dimensions (b) Field distributions of E_y or H_x along the x axis. (c) Field distributions of E_y or H_x along the y axis. (d) Simulated E field distributions of the waveguide cross section.

sensing mechanism of the WGM resonator, which is discussed in detail in the next sections.

2.2. Permittivity Sensing Mechanism of Whispering Gallery Mode Resonator

As presented in the Introduction, the WGM sensor proves ultra high sensitivity in optics platforms. The form of its adoption in the sub-THz DWG platform is shown in FIGURE 2.4. Place adjacent to the DWG, a disk-shaped dielectric resonator, made by the same dielectric material as the DWG, couples sub-THz EM wave from the DWG. This coupling between the DWG and the dielectric resonator results from the evanescent field in the Region 2 in FIGURE 2.3, which enables the coupling between two waveguides or a waveguide and a resonator placed at proximity. The decay rate α_x in x direction farther away from the waveguide dictates that larger distance between the waveguide and the resonator results in weaker coupling between the waveguide and the resonator.

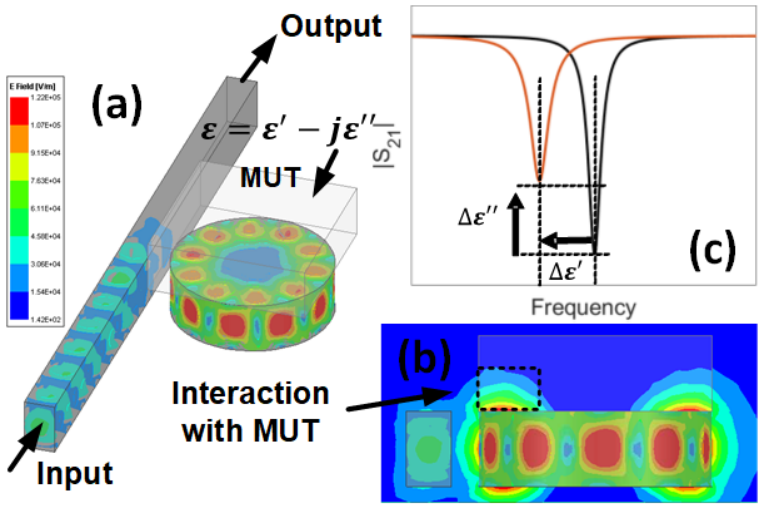

FIGURE 2.4. WGM sensor mechanism (a) E field of the WGM resonator sensor near resonance with (b) Front view of the E field of the resonator sensor. (c) Different transmission notches due to the complex permittivity of different MUT's.

After coupled into the resonator, the E_{11}^{y} mode wave is guided to circulate inside the resonator by the total internal reflections by the side wall of the disk resonator, hence the name whispering gallery mode, in analogy with the acoustic phenomenon in a rotunda [**38**]. When the wavelength of the circulating wave is exactly Nth fraction of the effective perimeter of the traveling path inside the resonator, the wave is trapped to accumulate to intensify, forming a high intensity WGM resonance, as shown in Fig, 4. The high intensity of the accumulated E field enables high sensitivity near field sensing [**?**]. The resonant wavelength is governed by the following equation

$$N \cdot \lambda_{res} = 2\pi r_{eff} \tag{2.2}$$

where N is the number of wavelengths in the resonator (or the mode number) and r_{eff} is the circulating radius of the resonant mode, which dependents on the radius of the resonator disk. The resonant wavelength and hence the resonant frequency can be impacted by the effective real permittivity, ϵ'_{eff}, which is determined by the disk material and its proximate dielectric environment,

$$N \cdot \frac{v_{eff}}{f_{res}} = 2\pi r_{eff}$$

$$f_{res} = \frac{N \cdot c}{2\pi r_{eff}\sqrt{\epsilon'_{eff}}}, \tag{2.3}$$

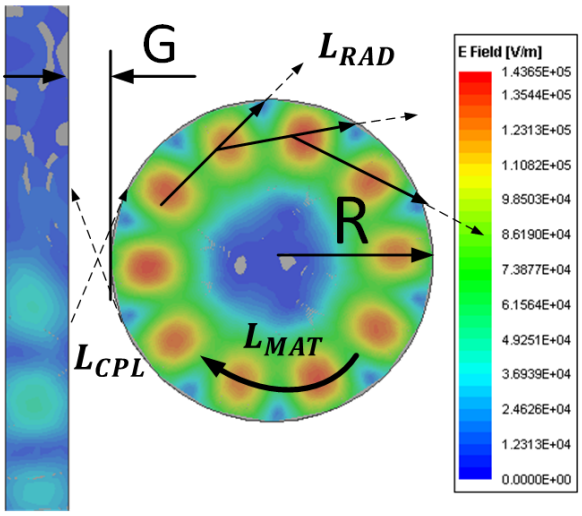

FIGURE 2.5. Top view of the E field of the WGM resonator near the resonance and loss attribution.

where v_{eff} is the effective velocity of the guided wave, and c is the speed of light in vacuum. Eqn. 2.3 reveals the fundamental mechanism by which the real permittivity of the MUT impact the transmission notch.

On the other hand, the imaginary permittivity of the MUT impact the transmission notch's depth by changing the loss of the resonator. The loss of the resonator comes from three major sources: radiation loss L_{RAD}, material loss L_{MAT}, and coupling loss L_{CPL}, as shown in Fig. 4. The radiation loss L_{RAD} is unique for the dielectric waveguide due to the internal reflections on the side wall boundary. L_{MAT} is the loss caused by the interaction of the EM field with the dielectric material, both the resonator itself and the MUT placed on the top of the resonator. L_{CPL} is the energy loss due to the wave coupling back to the feeding waveguide when it travels to the proximity of the waveguide after integer number of circulation in the resonator.

The best way to quantify the loss of the resonator is through its quality factor Q. The different losses can be associated and categorized with different Q's. The radiation loss can be represented by $1/Q_{RAD} \sim L_{RAD}$, and the material loss can be represented by $1/Q_{MAT} \sim L_{MAT}$. These two loss mechanisms can be combined and is called intrinsic loss, as they are the losses originated from the resonator itself, without being loaded by the feed waveguide. The corresponding Q is then

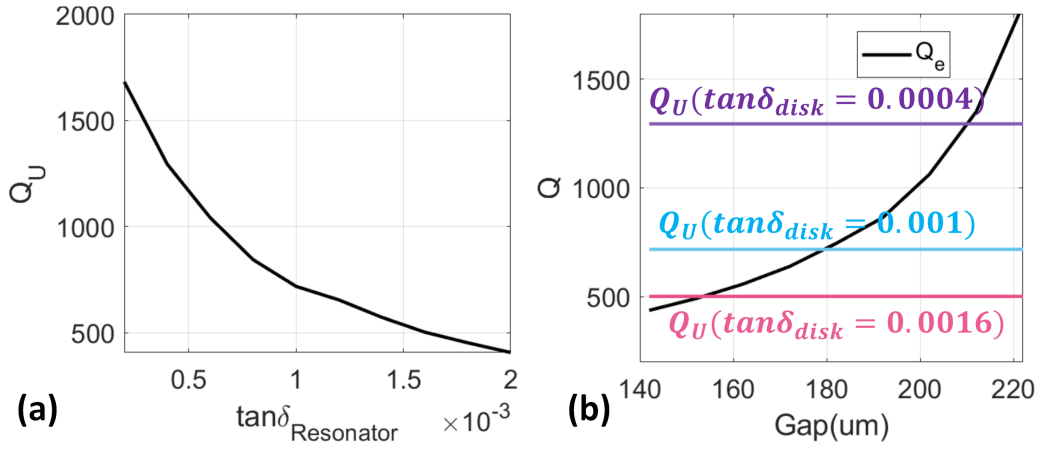

FIGURE 2.6. (a) Intrinsic Q vs. loss tangent of the material of the resonator (b) External Q vs. the ring gap G.

called intrinsic Q, Q_0, or unloaded Q, Q_U, and can be expressed as

$$Q_U = \frac{1}{Q_{RAD}} + \frac{1}{Q_{MAT}}, \tag{2.4}$$

The material loss, or Q_{MAT} can be directly impacted by the loss of the dielectric resonator material, which can be quantified by the loss tangent of the material, $tan\delta_{Resonator}$. The dependence of the intrinsic quality factor Q_U on $tan\delta_{Resonator}$ is simulated by changing the $tan\delta_{Resonator}$ of the resonator's material, as shown in FIGURE 2.6 (a). For HR silicon, whose loss tangent is 0.001, $Q_U \approx 730$.

The coupling loss is represented by external quality factor, $1/Q_e \sim L_{CPL}$. Since Q_e reflects the power loss through the coupling between the resonator and the waveguide, it has a dependence on the gap size G between the resonator and the waveguide, and the relationship is determined from the HFSS simulation, as shown in FIGURE 2.6 (b). For larger gaps between the waveguide and the resonator, the loss due to the coupling with the waveguide is lower and therefore Q_e increases correspondingly. The simulated intrinsic quality factor Q_U with different material loss is also plotted in the same figure. As expected, Q_U does not change with the gap, since it is determined by the internal loss of the resonator.

As can be seen from Eqn. 2.4, besides the material loss, Q_U is also impacted by the radiation loss. Since the radiation loss is caused by the internal reflection at the outer side wall of the resonator,

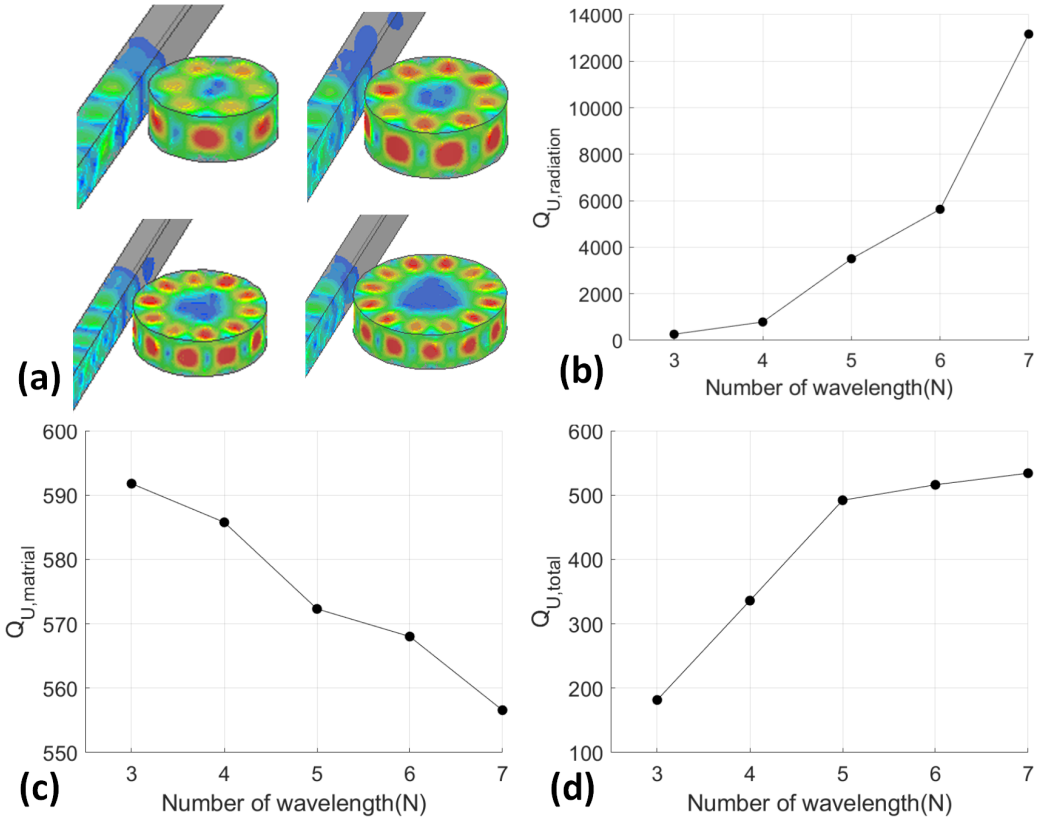

FIGURE 2.7. Quality factors vs. different number of resonant wavelength (a) E field of different number of wavelengths (b) Q_{RAD} vs. number of wavelengths. (c) Q_{MAT} vs. number of wavelengths. (d)Q_0 vs. number of wavelengths.

it can be reduced by the curvature of the side wall [**1**]. In the case of the WGM resonator, it is apparent that the side wall curvature can be reduced by increasing the perimeter and therefore the radius of the resonator. To have a fair comparison of the resonator's performance, the resonant frequency should be kept the same while changing the radius of the resonator. According to Eqn. 2.3, to keep the resonant frequency unchanged, namely the resonant wavelength unchanged, the number of wavelengths N that resonates inside the resonator should be changing with the radius, as shown in FIGURE 2.7. FIGURE 2.7 (a) shows four example cases of different number of circulating wavelengths of N = 3, 4, 5, and 6, which all resonate around 160 GHz. The corresponding radius are 535 um, 667 um, 797 um and 923um, respectively. FIGURE 2.7 (b) shows the simulated Q_{RAD} vs. the increasing number of resonating wavelengths, namely the increasing resonator radius. It can be seen that the radiation loss reduces with larger resonator radius, which is expected from the

theory [**39**]. On the other hand, the material loss is also observed to increase with the resonator radius, as shown in the simulation result in FIGURE 2.7 (c), in which Q_{MAT} drops with larger N. This is because, with larger radius, the traveling distance is longer for the EM wave within the resonator to complete one loop of circulation. This is nonetheless a relatively weak dependence, under the simulation setting of $tan\delta_{Resonator} = tan\delta_{HRSi} = 0.001$, as Q_{MAT} only drops from 590 to 560 as the radius increases from 535 um to 923 um, while, as a comparison Q_{RAD} increases from 200 to 13000, by more than 60 times. Hence, it is beneficial for the overall Q_U to increase the radius of the resonator. This is also verified in the plot of FIGURE 2.7 (d), where Q_U is simulated for increasing resonator radius. It can be observed by comparing FIGURE 2.7 (b), (c) and (d) that Q_U is dominated by Q_{RAD} when $N < 5$, and for $N > 5$, Q_U is primarily determined by Q_{MAT}, as dictated by their relationship specified in Eqn. 2.4. This also explains the saturation behavior of Q_U when $N > 5$. For $N > 5$, it is not as beneficial to increase the resonator radius because the sensor size becomes larger, which undermines the advantage of compactness of the sub-THz sensor. Therefore, based on the foregoing investigation, all of the WGM resonators in the rest of the investigation and implementations adopts N = 5 as a balance point between the quality factor and the resonator size.

When coupled to the DWG, the total loss of the resonator can then be expressed by loaded Q, Q_L, as

$$Q_L = \frac{1}{Q_e} + \frac{1}{Q_U} = \frac{1}{Q_e} + \frac{1}{Q_{RAD}} + \frac{1}{Q_{MAT}}, \tag{2.5}$$

As can be seen from Eqn. 2.5, Q_L can be impacted by both Q_U and Q_e. The loaded Q of the resonator can be determined by $Q_L = f_{res}/BW_{3dB}$ from simulation or measurement, where BW_{3dB} is the 3-dB bandwidth of the transmission notch of the resonance, as shown in FIGURE 2.8 (a).

From the general microwave resonator theory, the coupling condition between the resonator and the feeding DWG can be varied by changing the gap between the two. A coupling factor is defined in [**40**] as

$$g = \frac{Q_U}{Q_e}. \tag{2.6}$$

It is known that a coupling condition between the feeding waveguide and the resonator called critical coupling exists when $Q_U = Q_e$, or $g = 1$. At critical coupling, all power of the EM wave in

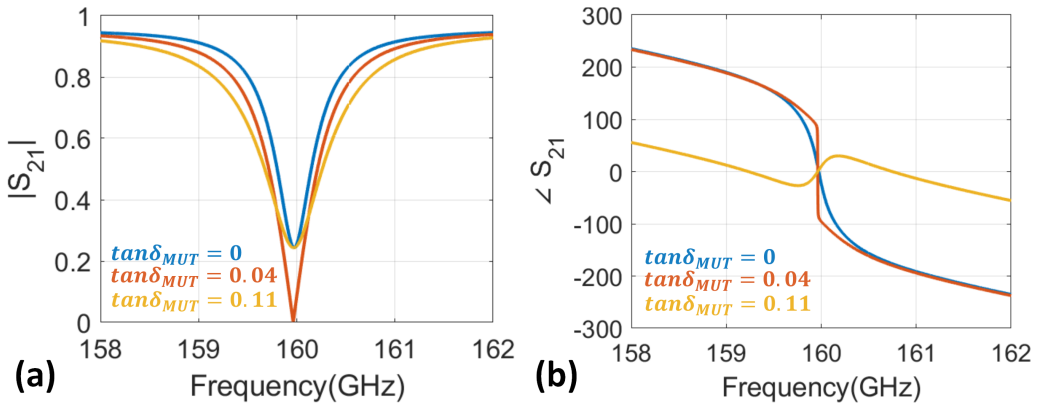

FIGURE 2.8. S_{21} of the resonator under different coupling conditions.

the DWG is be coupled into the resonator and dissipated by the radiation and material loss of the resonator, resulting a zero transmission at the resonant frequency, as shown in FIGURE 2.8 (a) (red curve). When the intrinsic loss of the resonator is lower than the coupling loss, namely $Q_U > Q_e$ or $g > 1$, the coupling condition is called over-coupling. This case is simulated by reducing the material loss of the resonator from the critical coupling case while keeping the resonator gap G unchanged, as shown by the blue curve in FIGURE 2.8 (a). In the contrary, when the intrinsic loss of the resonator is higher than the coupling loss, namely $Q_U < Q_e$, or $g < 1$, the coupling condition is called under-coupling. This case is simulated by increasing the material loss of the resonator from the critical coupling case while keeping the resonator gap G unchanged, as shown by the yellow curve in FIGURE 2.8 (a). It can be observed that, under the over-coupling and under-coupling condition, the transmission at resonant frequency cannot be zero. This property motivates the proper design of the coupling between the resonator and the waveguide to be at critical coupling to improve permittivity sensitivity, which is further discussed in Chapter 3. It is also observed that the phase response of the resonator also differs under different coupling conditions, as shown in FIGURE 2.8 (b). At critical coupling (red curve), the phase transition is sharp (in theory a 180° jump) at the resonant frequency. In the over-coupling condition (blue curve), the phase reduces faster at resonant frequency, resulting in a large and positive group delay, which is defined as $-d\angle S_{21}/d\omega$. In the under-coupling condition (yellow curve), the group delay reverse its sign near the resonant frequency. The phase response to the different coupling conditions due to the change

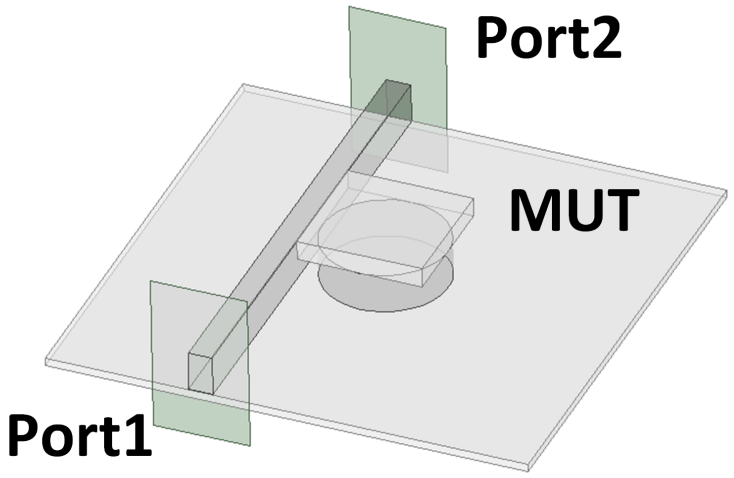

FIGURE 2.9. WGM resonator sensor simulation setup in HFSS.

of the loss of the resonator serves as the fundamental mechanism for the phase-detection based permittivity sensing, as discussed in detail in the following section.

2.3. Magnitude Detection vs. Phase Detection

As a complex number, the transmission S_{21} of the resonator sensor has significant responses of both magnitude and phase near its resonant frequency. To investigate this phenomenon, the WGM resonator sensor with an MUT placed on top is simulated in the HFSS. The HFSS setup is shown in FIGURE 2.9. The HR silicon DWG and resonator are placed on a quartz substrate, with two wave ports as the input and the output. The permittivity of the MUT placed on the top of the resonator is changed and the magnitude of the transmission $|S_{21}|$ and the phase of the transmission $\angle S_{21}$ are simulated, as shown in FIGURE 2.10. As the real permittivity ϵ_r' of the MUT changes from 2.1 to 2.5, the resonant frequency reduces from 162.78 GHz to 162.2 GHz, governed by Eqn. 2.3. From the simulation results in FIGURE 2.10 (a), the frequencies of the transmission notch reduces as ϵ_r' increases. Similarly, $\angle S_{21}$ demonstrates the resonant frequency shift in FIGURE 2.10 (b), as the abrupt phase jumps associated with the resonant frequencies move to lower frequencies for larger ϵ_r'. Generally speaking, the measurement or detection of either $|S_{21}|$ and $\angle S_{21}$ can be used to detect the resonant frequency change, and thus the permittivity difference of the different MUT's. However, the most common detection scheme is still magnitude based [**41**] [**42**] [**43**]. The reason is

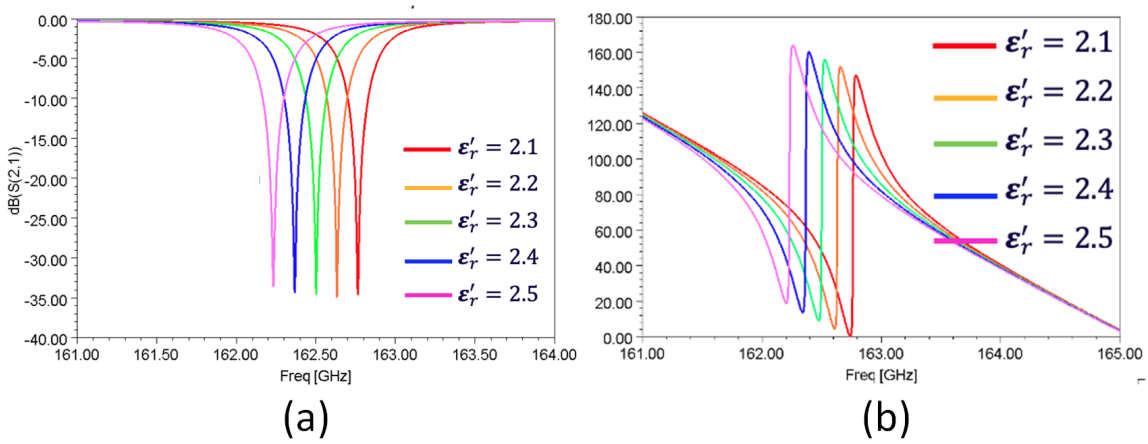

FIGURE 2.10. Magnitude and phase of the transmission for MUT with different permittivity (a) $|S_{21}|$ (b) $\angle S_{21}$.

that the magnitude of the transmission is generally easier to measure, especially for the optics, the phase measurement of the laser is rather difficult. Nonetheless, the sharp phase transition at the resonant frequency is alluring and suggests high permittivity sensitivity. The sharp phase transition means a small resonant frequency shift caused by a small permittivity difference would result in a large phase difference between the input and the output of the sensor. Since phase detection is manageable in electrical systems, it appears promising to utilize the phase of the WGM resonator to detect small permittivity difference, namely high permittivity sensitivity and sensing resolution. The following investigation evaluates the permittivity sensitivity of the phase detection scheme and compares that with the magnitude detection scheme.

To quantify and compare the sensitivity for the magnitude detection and the phase detection scheme, a set of simulations are conducted that emulate the sensor's response in a magnitude-detection based sensing system and in a phase-detection based sensing system, respectively. First, the EM simulation of the WGM sensor based on the setup in FIGURE 2.9 provides the S_{21} response of WGM sensor for two different cases: $\epsilon'_{r,MUT} = 3$ and $\epsilon'_{r,MUT} = 3.00001$. The resonant frequency shifts to lower values by 14 kHz. The S-parameters of these two simulations are imported in circuit simulator. The corresponding test bench is shown in FIGURE 2.11 (a). In the circuit simulation test bench, the source with 50 Ohm internal impedance excites the sensor with a 20 mV CW tone, whose frequency is swept from 159 GHz to 161 GHz. The magnitude and the phase of the

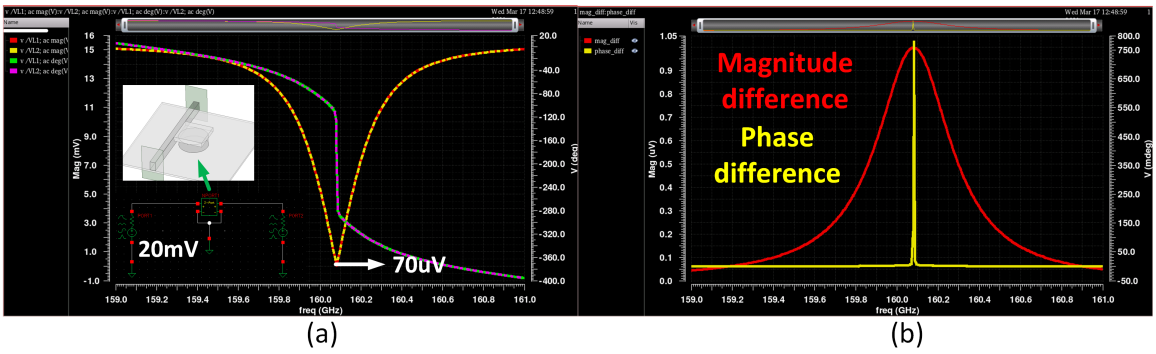

FIGURE 2.11. Sensor output for $\epsilon_r = 3$ and $\epsilon_r = 3.00001$ with 20 mV input sine wave excitation (a) Output magnitude and phase. (b) Difference of the output magnitude and phase.

signals at the output of the sensor, which is a 50 Ohm load, are plotted in FIGURE 2.11 (a). The red and the yellow curves are the magnitudes of the output signals of the case $\epsilon'_{r,MUT} = 3$ and $\epsilon'_{r,MUT} = 3.00001$, respectively. The green and the pink curves are the phases of the output signals of the case $\epsilon'_{r,MUT} = 3$ and $\epsilon'_{r,MUT} = 3.00001$, respectively. The curves are closely overlapped, due to the very small frequency shift from the small permittivity difference. At the resonant frequency, the magnitudes display transmission notch, with only 70 uV delivered to the load. The phases also display a sharp jump of near 180° because the WGM resonator in the simulation is designed to be in the critical coupling condition. The magnitudes and the phases of the case $\epsilon'_{r,MUT} = 3.00001$ are subtracted from the case $\epsilon'_{r,MUT} = 3$ and the magnitude of the results are shown in FIGURE 2.11 (b). It can be observed that, for the MUT permittivity difference of 0.00001, the sensor's output signals show a 1 uV of magnitude difference and a 0.78° phase difference under a 20 mV CW excitation. To evaluate the signal strength of a voltage magnitude (1 uV) and a phase (0.78°) on a equal footing, a phasor representation of the signals are drawn in FIGURE 2.12 (a). FIGURE 2.11 shows the simulation results. The yellow vector represents the signal at the output of the sensor at the resonant frequency for the case of $\epsilon'_{r,MUT} = 3$, which is called the reference signal or the reference vector in this analysis. The green vector represents the signal at the output of the sensor at the resonant frequency for the case of $\epsilon'_{r,MUT} = 3.00001$, which is called the sensing signal or the sensing vector in this analysis. The magnitude difference of the two vectors is denoted by Δv and the phase difference is $\Delta\phi$. In a practical phase measurement system, the phase difference

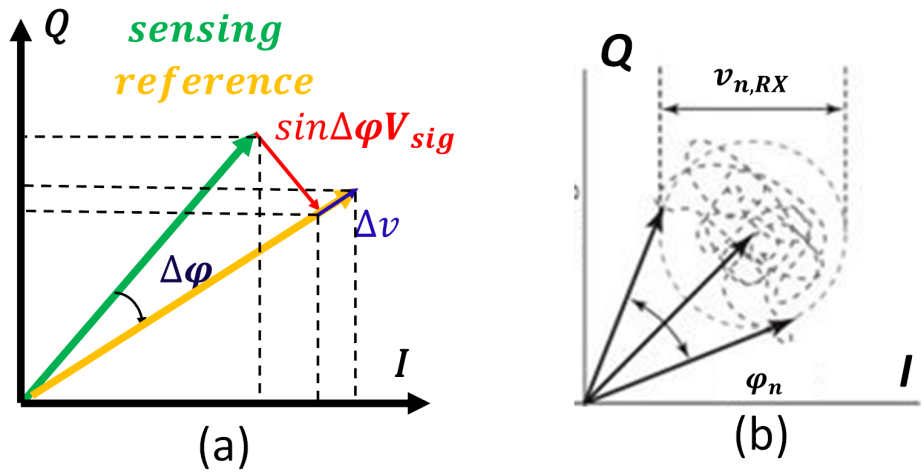

FIGURE 2.12. Phasor representation of the magnitude and the phase of (a) Signal (b) Noise.

of two signals is derived from the vector $sin\Delta\phi \cdot V_{sig}$, which is essentially a voltage or magnitude quantity, where V_{sig} is the magnitude of the reference of the reference vector, which is around 70 uV in this analysis, shown in FIGURE 2.11 (a). The quantity $sin\Delta\phi \cdot V_{sig}$ is an approximation of the magnitude of the vector difference of the sensing vector and the reference vector, under the condition in which $\Delta\phi$ is small. Since $\Delta\phi$ is eventually derived in the measurement from the quantity $sin\Delta\phi \cdot V_{sig}$, the comparison between Δv and $sin\Delta\phi \cdot V_{sig}$ is effectively equivalent to the comparison between Δv and $\Delta\phi$ when $\Delta\phi$ is small. From the simulation results shown in FIGURE 2.11, $sin\Delta\phi \cdot V_{sig} = 0.977uV$. This value is approximately equal to Δv, which is 1 uV. This shows that the WGM sensor's magnitude and phase response are nearly the same in the signal strength standing point.

This conclusion can be further proved from the SNR analysis of the magnitude signal and the phase signal in a potential measurement system. The SNR of a magnitude measurement system can be represented by

$$SNR_v = \frac{\Delta v}{v_n} = \frac{\Delta v}{v_{n,RX}}, \tag{2.7}$$

where $v_{n,RX}$ is the rms voltage noise of the magnitude measurement system. On the other hand, the SNR of a phase measurement system can be represented by

$$SNR_{\phi} = \frac{\Delta\phi}{\phi_n} = \frac{\Delta\phi \cdot V_{sig}}{v_{n,RX}}, \tag{2.8}$$

where ϕ_n is the rms phase fluctuation or phase noise of the phase measurement system. The phase fluctuation of a measurement system can be represented by the phase uncertainty of a signal vector, as shown in the phasor diagram in FIGURE 2.11 (b). The uncertainty of a measured signal vector is modeled as a small noisy vector being superposed to a deterministic signal vector. The end-point of the sum vector draws a cloud of uncertainty due to the noise component. The resulting rms magnitude uncertainty of the measured signal vector is the diameter of the rms end-point cloud, denoted as $v_{n,RX}$, which is essentially the voltage noise of the measurement RX. The phase uncertainty of the measurement RX is the phase span of the signal vector across the rms end-point cloud, denoted as ϕ_n. When ϕ_n is small, which is usually the case for noise, it can be approximately represented as $v_{n,RX}/V_{sig}$ [**44**]. By comparing SNR_v and SNR_{ϕ}, it can be observed that the denominators are the same, which is the voltage noise of the measurement RX. To compare the SNR of the magnitude and the phase detection scheme, the ratio of the SNR's are calculated using the values from the simulation in FIGURE 2.11,

$$\frac{SNR_{\phi}}{SNR_v} = \frac{\Delta\phi \cdot V_{sig}}{\Delta v} = \frac{0.014rad \cdot 70uV}{1uV} = 0.977, \tag{2.9}$$

The identical results from the two analysis processes above stems from the mechanism based on which signal phase or phase difference are measured in practical phase measurement system. For signal whose magnitude is small, the quantity that its angle is derived from is also small. Therefore, for the WGM sensor, the fact that its sharp phase transition locates at the transmission notch leads to a overall small phase signal strength. The weak transmission at the resonant frequency nullifies the seemingly high sensitivity phase response. To conclude, for the case of WGM resonator as a permittivity sensor, its phase response has no sensitivity advantage over its magnitude response. In other words, a sensing system based on phase detection has no SNR advantage over a magnitude detection sensing system. Besides, it can be observed from FIGURE 2.11 (b) that the phase difference (yellow curve) has a very narrow frequency span, whose FWHM is only 2 MHz, as

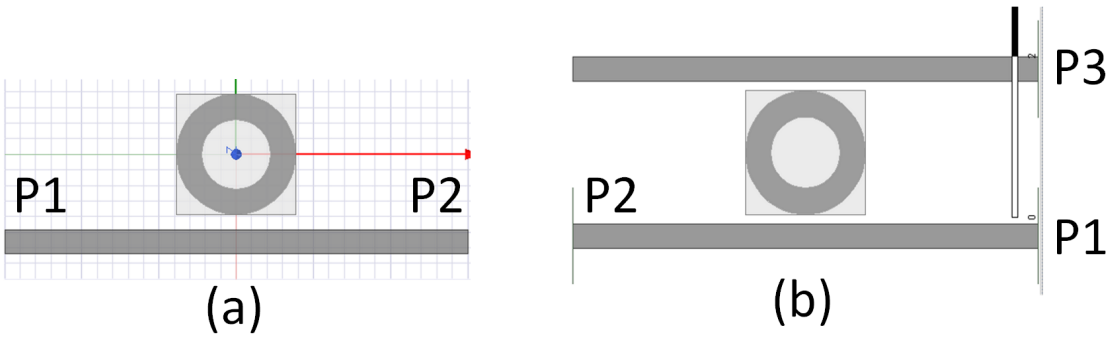

FIGURE 2.13. Top view of the WGM resonator sensor in configurations of (a) band-stop and (b)bandpass.

comparing to the magnitude difference (red curve)'s 200 MHz.The small usable frequency range of the phase difference further discourages the adoption of phase detection scheme. Hence, both of the sensing systems developed in this dissertation are magnitude detection systems.

2.4. Band-Stop Sensor vs. Band-Pass Sensor

It is ubiquitous for the WGM resonator sensor to be used in bandstop configuration [**45**] [**46**] as well as in bandpass configuration [**47**] [**48**]. FIGURE 2.11 shows the top views of the two configurations in HFSS simulation setup. Between the two configurations, there is no known conclusions that one is advantageous over the other in terms of sensitivity. Indeed, on a theoretical grounding, there is no underlying difference between the two except for the direction change of the signal propagation. The relevant factors for the sensitivity, such as loss, field intensity, are on the same level. However, the sensitivity comparison of the two in terms of phase response is not yet discussed in the literature. Therefore, the investigations are conducted to compare the sensitivity of the two configuration in both magnitude and phase response and are summarized below. FIGURE 2.14 (a) and (c) show $|S_{21}|$ and $\angle S_{21}$ of the WGM resonator sensor in the bandstop configuration for different loss and different coupling conditions. To the right, FIGURE 2.14 (b) and (d) show the derivatives of $|S_{21}|$ and $\angle S_{21}$, representing the slope, or the magnitude and phase sensitivity of the WGM resonator. It can be seen that both the maximum magnitude sensitivity and the maximum phase sensitivity occur around the critical coupling point. FIGURE 2.15 (a) and (c) show $|S_{21}|$

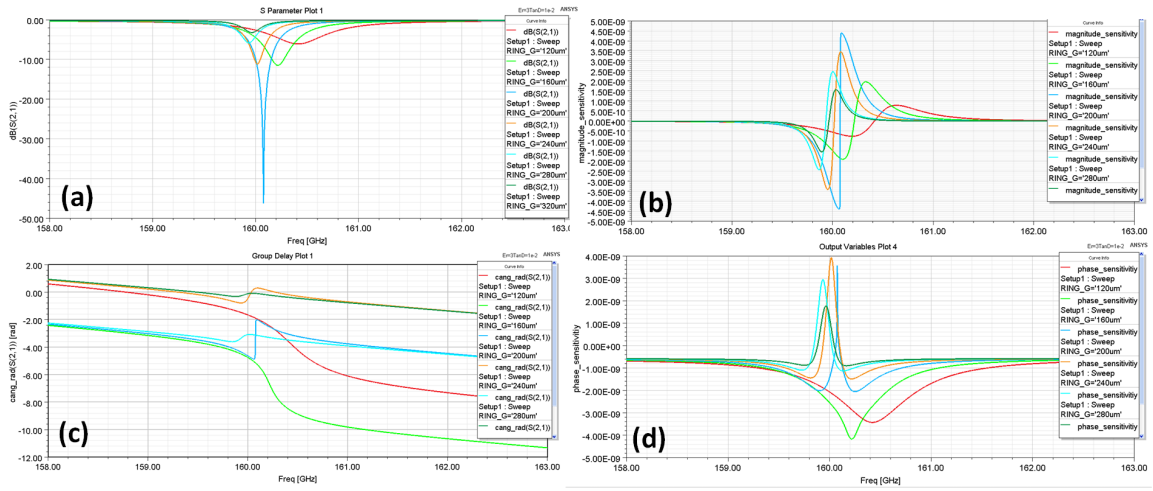

FIGURE 2.14. HFSS simulation results of the bandpass configuration for different gap widths between the resonator and the waveguide (a) $|S_{21}|$. (b)The derivative of $|S_{21}|$ over frequency. (b) The derivative of $|S_{21}|$ over frequency. (c) $\angle S_{21}$. (d)The derivative of $\angle S_{21}$ over frequency.

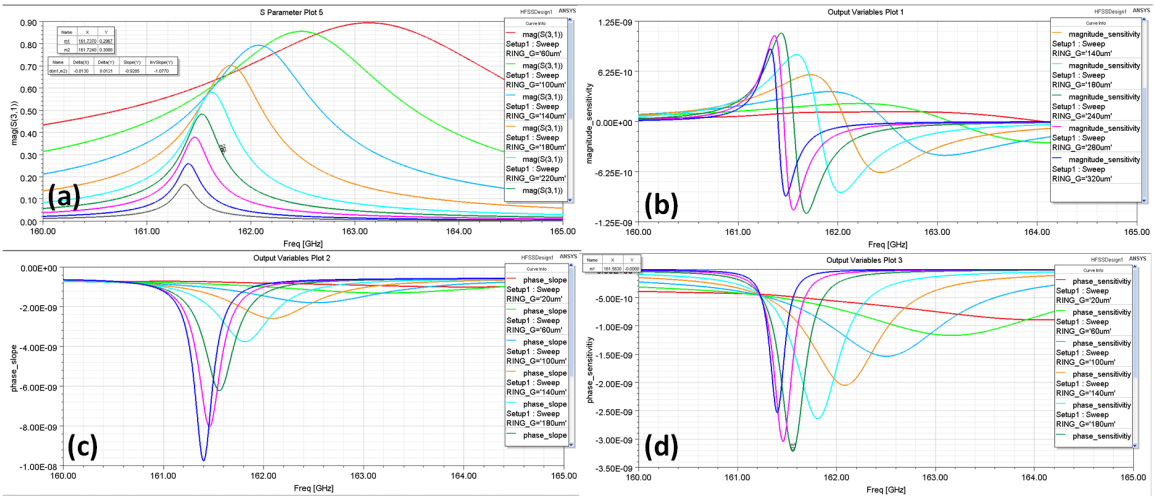

FIGURE 2.15. HFSS simulation results of the bandpass configuration for different gap widths between the resonator and the waveguide(a) $|S_{21}|$. (b)The derivative of $|S_{21}|$ over frequency. (b) The derivative of $|S_{21}|$ over frequency. (c) $\angle S_{21}$. (d)The derivative of $\angle S_{21}$ over frequency.

and $\angle S_{21}$ of the WGM resonator sensor in the bandpass configuration for different loss and different coupling conditions. To the right, FIGURE 2.14 (b) and (d) show the derivatives of $|S_{21}|$ and $\angle S_{21}$, representing the slope, or the magnitude and phase sensitivity of the WGM resonator. Different from the bandstop counterparts, neither of the the maximum magnitude sensitivity nor

	Bandstop (gap = 200um)	Bandpass (gap = 250um)
Max mag sens.	4.5nV/Hz	1.1nV/Hz
Max phase sens.	4nV/Hz	3.2nV/Hz

FIGURE 2.16. HFSS simulation results of the bandpass configuration for different gap widths between the resonator and the waveguide(a) $|S_{21}|$. (b)The derivative of $|S_{21}|$ over frequency. (b) The derivative of $|S_{21}|$ over frequency. (c) $\angle S_{21}$. (d)The derivative of $\angle S_{21}$ over frequency.

the maximum phase sensitivity occur around the critical coupling point. They occur at the balance points of the loaded Q and the insertion loss.

FIGURE 2.16 summarizes the maximum magnitude sensitivity and the maximum phase sensitivity of the bandstop and the bandpass configurations. It shows that the bandstop configuration has better performance in terms of sensitivity for both magnitude and phase detection schemes. This is expected to some extent because the bandpass configuration naturally has higher loss due to one more coupling to the waveguide at the output port. This extra loss brings down both the quality factor, resulting duller slope and curvature of the curve, as well as the insertion loss, leading to weaker signal strength. Nevertheless, the bandpass configuration is still adopted in the sensing system presented in Chapter 4, due to the unique architecture of the receiver of the sensing system, while the bandstop configuration is adopted in the sensing system presented in Chapter 5 for its high sensitivity and smaller form factor.

2.5. Disk Resonator Sensor vs. Ring Resonator Sensor

In optics, various forms of WGM resonators have been reported, including disk, ring, sphere, hemisphere, toroid, etc., as summarized in this review [**38**]. The performance, particularly the Q of the resonator varies with the forms of the resonator. It is not to have a fair comparison among them, though, because the materials, dimensions and methods of fabrication are all different for the different forms. Therefore, the primary considerations on choosing the form of the WGM resonator is the implementation and fabrications. Given the low cost fabrication flow of silicon etching, the most suitable forms of the WGM resonator are the disk and the ring. The properties

and performance of the disk resonator and the ring resonators are investigated and compared in the following. Given the excitation method from the E_1^y1 DWG, the mode that resonates in the resonators are the same for the disk and the ring resonator, as shown in FIGURE 2.17. The most prominent contrast is the resonant frequencies between the two type of the resonators. With the same outer radius of 797 um and the same number of resonant wavelengths of 5, the disk resonator's resonant frequency is 158 GHz, which is $\tilde{5}$ GHz lower than that of the ring resonator. This is predictable from Eqn. 2.3. It can be seen from the top view that, comparing with the disk, the center region of the ring resonator is replaced with air. Therefore, the average permittivity experienced by the resonant mode is lowered by the air region, resulting in higher resonant frequency. Another property which is impacted by this form difference is the quality factor of the resonator. The EM field in the center region of the disk resonator experiences higher material loss than its ring counterpart, which has air in its center region. Nonetheless, this turns out to be a relatively weak effect, as being determined from the EM simulations. Q_L of the resonator is simulated for different ring widths, with a fixed outer ring radius of 797 um, and the results are shown in FIGURE 2.17 (c). As the ring width increases from 300 um to 797 um, Q_L drops slightly from 250 to 230, since for higher ring width, more EM fields are in the dielectric material of the resonator and less in the air. Note that the ring resonator becomes a disk resonator when its ring widths increases to the outer radius of the resonator of 797 um. Based on the sensitivity analysis in the next Chapter, resonator with higher Q_L has higher permittivity sensitivity. Therefore, the ring resonator has slightly higher permittivity sensitivity comparing to the disk resonator. Nonetheless, from the simulation of FIGURE 2.17 (c), its is a relatively weak dependence. The choice of the resonator form is mainly based on other factors, such as the form of the MUT sample. For example, if the MUT sample is in liquid form, disk is more suitable as it can hold the liquid drop on its top surface. Otherwise, without a holding surface in the center region, the liquid leaks through the air gap between the bottom of the ring resonator and the substrate. However, the MUT samples are in solid form, the two resonator forms should works equally well in the measurement point of view. Therefore, in the low power permittivity sensing system prototype presented in Chapter 4, the ring resonators are adopted as the permittivity sensor. And in the high resolution complex permittivity

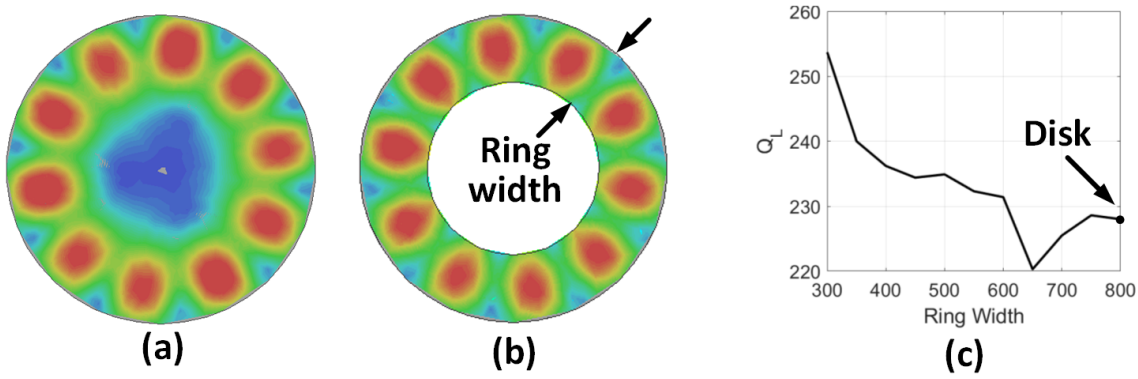

FIGURE 2.17. HFSS simulations of the disk and the ring WGM resonator (a) Top view of the magnitude of the E field in a disk resonator in resonance. (b) Top view of the magnitude of the E field in a ring resonator in resonance. (c) Resonator Q_L vs. the width of the ring resonator.

sensing system prototype presented in Chapter 5, disk resonators are used as the permittivity sensor to have the potential capability of measuring liquid MUT samples.

CHAPTER 3

High Sensitivity Whispering Gallery Mode Complex Permittivity Sensors

This chapter discusses the design and analysis of the high sensitivity complex permittivity sensors that are utilized in the high resolution complex permittivity sensing system. The sensor has complex permittivity sensing capability, and its sensitivity is optimized based on the theory and principle presented in Chapter 2. Its non-ideality and implementation are also recorded in the last sections of this chapter.

3.1. Complex Permittivity Sensing Mechanism

As discussed in Chapter 2 and shown in FIGURE 2.4, the WGM resonator sensor has different transmissions, or S_{21}, when MUT's with different permittivity are placed on the sensor top. This transmission difference can be utilized to infer the permittivity of the MUT. In order to achieve this, two identical WGM resonator sensors with coupling waveguides are used in a complimentary configuration, as shown in FIGURE 3.1. forming a sensing path and a reference path. A reference MUT with known permittivity, MUT_{REF}, is placed on the sensor of the reference path, while an MUT with unknown permittivity, MUT_{SEN}, is placed on the sensor of the sensing path. Due to the permittivity difference of the two MUT's, the transmissions of the two resonator sensors and therefore the two paths are different, and the transmission difference, ΔS_{21}, can be measured to get the information of the permittivity difference. The permittivity of the unknown material MUT_{SEN}, ϵ_{SEN}, can then be readily calculated based on the permittivity of the known material MUT_{REF}, ϵ_{REF}, and the permittivity difference, $\Delta\epsilon$, between the two. Namely, $\epsilon_{SEN} = \epsilon_{REF} + \Delta\epsilon$.

As illustrated in FIGURE 2.4, the transmission of the WGM resonator sensor has two unique and distinguishable responses for the MUT's with different real permittivity difference $\Delta\epsilon_r'$ and

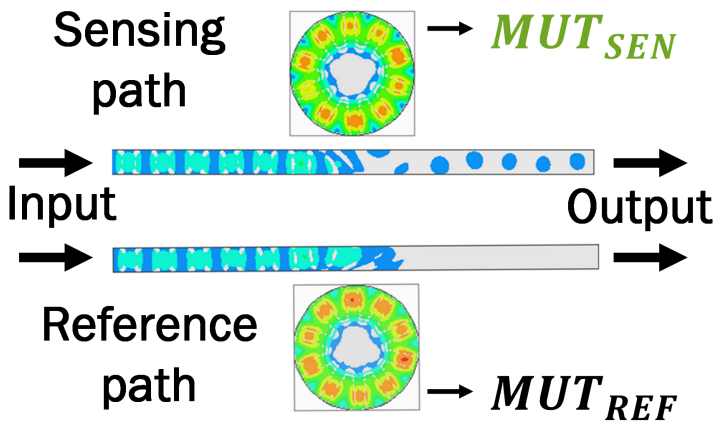

FIGURE 3.1. The complimentary configuration of a sensing path and a reference path utilizing identical WGM sensors to get the transmission difference or ΔS_{21} of the two paths and hence the permittivity difference of the different MUT samples on the two sensors.

imaginary permittivity difference $\Delta\epsilon_r''$, respectively. It is a natural results from the fact that the real and the imaginary permittivity of the MUT are two distinct and "orthogonal" properties of the materials. The term "orthogonal" stems from the analogy between ϵ_r' and ϵ_r'' and their circuit equivalence, a capacitor C and a resistor R, respectively, whose impedance have a 90 degree phase difference. This orthogonality can be indeed observed from ΔS_{21} of the resonator sensors when MUT's with different permittivity are placed on the sensors' top, as shown in the simulation results in FIGURE 3.2. In this set of simulations, S_{21} of the WGM resonator sensors are simulated when a reference MUT with permittivity $\epsilon_r = 2 - 0.001$ are placed on the sensor of the reference path and 3 other different MUT's with permittivity $\epsilon_r = 2 - 0.051$, $\epsilon_r = 2.5 - 0.001$ and $\epsilon_r = 2.5 - 0.051$ placed on the sensing path in sequence. As shown in FIGURE 3.2 (a), the $|S_{21}|$ of the sensors with the different MUT have different notch frequencies or notch depths. For MUT_{SEN} with higher ϵ_r'' than MUT_{REF}, the resonance notch is shallower, as shown by the orange $|S_{21}|$ curve. This is because the higher loss that the MUT introduces into the resonance pushes the resonator further away from the critical coupling condition, a mechanism discussed in detail in Chapter 2 (FIGURE 2.8). For MUT_{SEN} with higher ϵ_r' than MUT_{REF}, the resonance notch shifts to lower frequencies, as shown by the yellow $|S_{21}|$ curve, a phenomenon predicted by Eqn. 2.3. For MUT_{SEN} with higher ϵ_r'' as well as ϵ_r' than MUT_{REF}, the resonance notch is shallower and shifts to lower frequencies at the

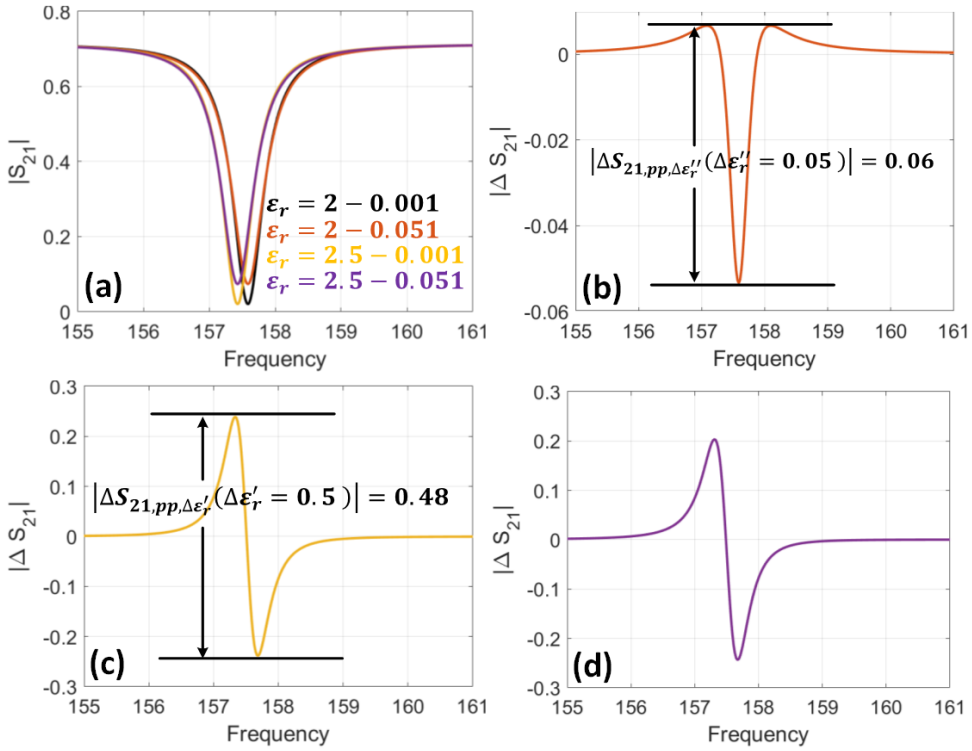

FIGURE 3.2. S_{21} of the resonator sensor with MUT's of wide range of permittivity.

same time, as shown by the purple $|S_{21}|$ curve, which is a combined response of the previous two cases.

The transmission differences, $\Delta S_{21} = S_{21,SEN} - S_{21,REF}$ of the three different MUT_{SEN} and MUT_{REF} are plotted in FIGURE 3.2 (b), (c) and (d). It is observed that, when the MUT_{SEN} and MUT_{REF} have the same ϵ'_r and have only ϵ''_r difference, the corresponding ΔS_{21} waveform shows even symmetry around the resonant frequency, as shown in FIGURE 3.2 (b). The peak-to-peak amplitude of the even waveform, $\Delta S_{21,\Delta\epsilon''_r}$, is found to be proportional to $\Delta\epsilon''_r$. This originates from the fact that a larger $\Delta\epsilon''_r$ between MUT_{SEN} and MUT_{REF} results in a larger resonant notch depth difference between the S_{21} waveforms, and hence a difference waveform with larger amplitude. In this particular simulation, the amplitude is 0.06 due to a $\Delta\epsilon''_r$ of 0.05. On the other hand, when the MUT_{SEN} and MUT_{REF} have the same ϵ''_r and have only ϵ'_r difference, the corresponding ΔS_{21} waveform shows odd symmetry around the resonant frequency, as shown in FIGURE 3.2 (c). Similar to the $\Delta\epsilon''_r$ case, a larger $\Delta\epsilon'_r$ between MUT_{SEN} and MUT_{REF} results in a greater difference of the resonant frequencies of the sensing path sensor and the reference path sensor and

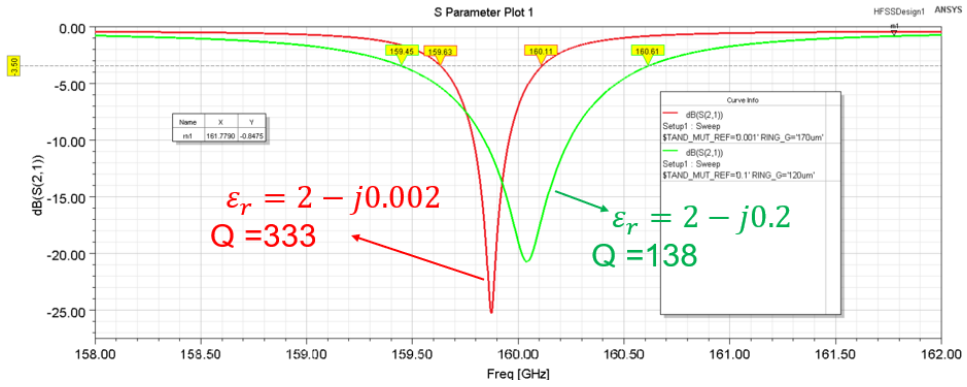

FIGURE 3.3. The impact of the loss of the MUT on resonator's quality factor.

thus a larger peak-to-peak amplitude of the odd waveform, $\Delta S_{21,\Delta\epsilon_r'}$. In this particular simulation, the amplitude is 0.48 due to a $\Delta\epsilon_r'$ of 0.5. When $\Delta\epsilon_r$ is a complex number, namely, both ϵ_r' and ϵ_r'' of the MUT_{SEN} and the MUT_{REF} are different, which corresponds to the case of the purple curve in FIGURE 3.2 (a), the resulting ΔS_{21} waveform has neither even nor odd symmetry, as shown in FIGURE 3.2 (d). And it is found that the waveform in in FIGURE 3.2 (d) is the sum of the waveforms of FIGURE 3.2 (b) and FIGURE 3.2 (c). This property of the sensor response provides the foundation of its complex sensing capability by curve fitting. The sensitivity of the WGM sensor can be defined readily as

$$Sen_{\epsilon_r'} \overset{\text{def}}{=} \frac{|\Delta S_{21,pp,\Delta\epsilon_r'}|}{\Delta\epsilon_r'},\ Sen_{\epsilon_r''} \overset{\text{def}}{=} \frac{|\Delta S_{21,pp,\Delta\epsilon_r''}|}{\Delta\epsilon_r''} \tag{3.1}$$

where $\Delta\epsilon_r'$ and $\Delta\epsilon_r''$ are the real and imaginary permittivity difference between the reference and sensing material that cause the corresponding waveform amplitudes $|\Delta S_{21,pp,\Delta\epsilon_r'}|$ and $|\Delta S_{21,pp,\Delta\epsilon_r''}|$. The sensitivities are optimized when the resonators have high Q. As shown in FIGURE 3.3, higher resonator Q factor leads to steeper slope, which produce large response even for small $\Delta\epsilon_r'$ and $\Delta\epsilon_r''$. Another method to improve the sensitivity is to place the sensor near critical coupling with the feeding waveguide. Detailed sensitivity analysis is presented in the following subsection.

3.2. Sensitivity Analysis

The complex permittivity sensitivity of the WGM resonator sensor can be optimized by improving the intrinsic quality factor, Q_U, and optimizing the coupling condition.

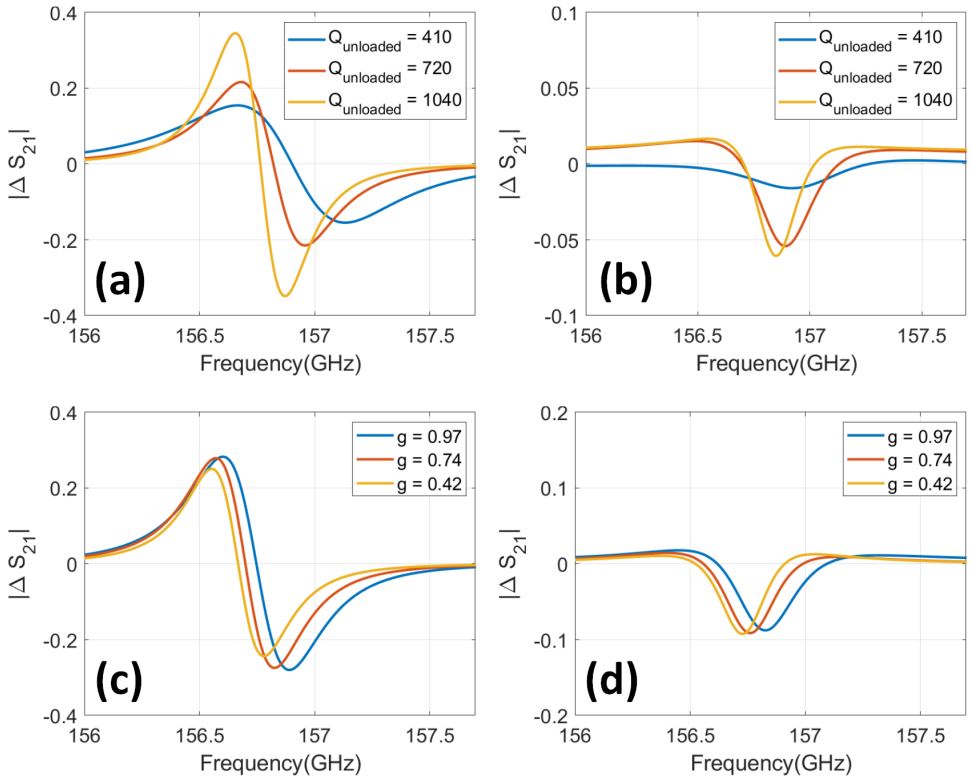

FIGURE 3.4. The dependence of the complex permittivity sensitivity of the resonator sensor on resonator Q and coupling conditions. (a)$Sen_{\epsilon_r'}$ vs. Q_U. (b) $Sen_{\epsilon_r''}$ vs. Q_U. (c)$Sen_{\epsilon_r'}$ vs. g (d)$Sen_{\epsilon_r''}$ vs. g.

FIGURE 3.4 (a) shows the dependence of real permittivity sensitivity $Sen_{\epsilon_r'}$ on Q_U, in which Q_U is adjusted by changing the loss tangent of the WGM resonator while keeping $g = 1$. For a constant $\Delta\epsilon_r' = 0.1$ between MUT_{SEN} and MUT_{REF}, higher Q_U results in a higher $|\Delta S_{21,pp,\Delta\epsilon_r'}|$, and thus higher real permittivity sensitivity $Sen_{\epsilon_r'}$ per definition in Eqn. 3.1. This results from the sharper slope of the S_{21} curves from resonators with higher Q_U. In the simulated Q_U range, $Sen_{\epsilon_r'}$ improves proportionally with Q_U. FIGURE 3.4 (b) shows the dependence of imaginary permittivity sensitivity $Sen_{\epsilon_r''}$ on Q_U, given a constant $\Delta\epsilon_r'' = 0.01$ between MUT_{SEN} and MUT_{REF}. It can be observed that, sensors with higher Q_U results in higher ΔS_{21} amplitude, $|\Delta S_{21,pp,\Delta\epsilon_r''}|$, and therefore a higher $Sen_{\epsilon_r''}$. Notice that FIGURE 3.4 (b) shows a slower improvement in $|\Delta S_{21,pp,\Delta\epsilon_r''}|$ and thus in $Sen_{\epsilon_r''}$ in higher Q_U range. This results from the fact that the resonator loss is dominated by the material loss of the MUT, and therefore the reduction of the material loss does not further help the improvement of the overall Q_U of the resonator sensor. FIGURE 3.4 (c) shows

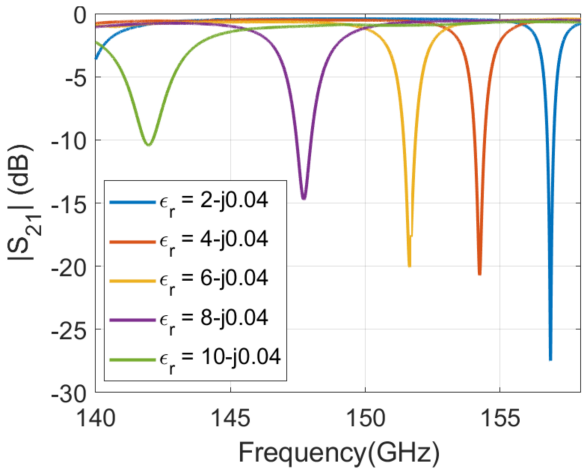

FIGURE 3.5. S_{21} of the WGM resonator sensor with MUT's of $\epsilon_r' = 2 - 10$ and $\epsilon_r'' = 0.04$.

the dependence of $Sen_{\epsilon_r'}$ on the coupling coefficient defined in Eqn. 2.6. It can be observed that a coupling condition closer to critical coupling, namely $g \approx 1$, leads to a higher $|\Delta S_{21,pp,\Delta\epsilon_r'}|$, and thus a higher real permittivity sensitivity $Sen_{\epsilon_r'}$. However, comparing with FIGURE 3.4 (a), the dependence of $Sen_{\epsilon_r'}$ on coupling is relatively weaker than its dependence on Q_U. Lastly, FIGURE 3.4 (d) shows negligible correlation between $Sen_{\epsilon_r''}$ and coupling condition.

As a summary, to achieve the best complex permittivity sensitivity, the WGM sensor should have high Q and should couple to the feeding DWG in critical coupling condition.

3.3. Nonideality Analysis

In this section, an important nonideality of the WGM resonator complex permittivity sensor is analyzed. From the foregoing theoretical analysis of the WGM resonator sensor, the WGM resonator sensor's response to ϵ_r' change is the frequency shift of the notch center frequency, and its response to ϵ_r'' change is the change of the notch depth. In general, these two distinguished types of responses can be observed when $\Delta\epsilon_r'$ and $\Delta\epsilon_r''$ are small (typically $\Delta\epsilon_r' < 0.1$ and $\Delta\epsilon_r'' < 0.01$). On the other hand, when $\Delta\epsilon_r'$ and $\Delta\epsilon_r''$ are larger, certain second-order effect becomes significant. More specifically, large $\Delta\epsilon_r'$ will cause notch depth difference and large $\Delta\epsilon_r''$ will cause resonant frequency shift. For example, as shown in FIGURE 3.5, while $\epsilon_r'' = 0.04$ remains unchanged, the increase of ϵ_r' not only shifts the resonant notch to lower frequencies, but also raises the notch depth and broadens the 3-dB bandwidth of the resonance. It appears that increasing ϵ_r' also increases the loss

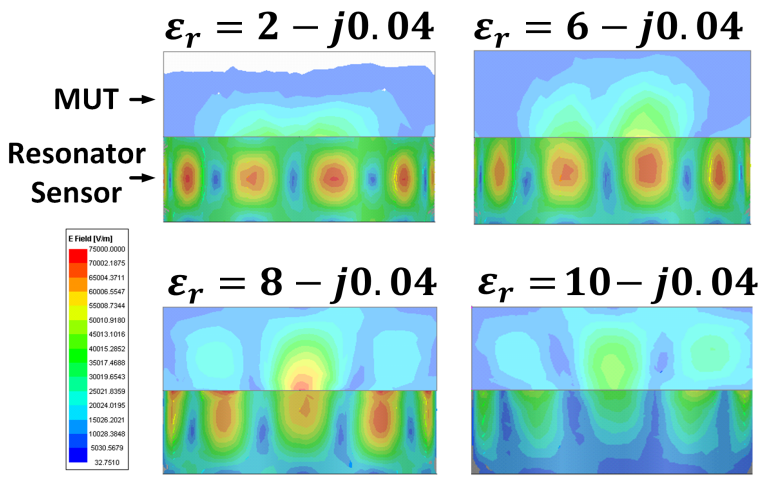

FIGURE 3.6. Side view of the resonator's E field with MUT of different real permittivity.

of the resonance, a response only expected from the increase of ϵ_r''.

This phenomenon can be explained by looking at the EM fields in the resonator and in the MUT samples. As shown in FIGURE 3.6, 4 different MUT samples with different ϵ_r' but same $\epsilon_r'' = 0.04$ is placed on top of the resonator sensor. It can be observed that for higher ϵ_r', the EM fields tend to extend more into the MUT samples. This can be explained intuitively by the lower ϵ_r' contrast at the boundary of the top surface of the resonator sensor in case of MUT samples with higher ϵ_r'. Given the HR-Si resonator sensor's permittivity of $\epsilon_r = 11.7 - 0.012$, the lower permittivity contrast lowers the field confinement due to the total internal reflection at the top surface of the resonator sensor. Quantitatively, this phenomenon can be explained by Eqn. 2.1. In Region 3 of FIGURE 2.3, where the MUT sample is placed, in order to satisfy the constitutive equations of the wavenumbers in Region 3, a lower α_y results from a higher $\epsilon_{r,3}'$, which means lower field attenuation in y direction and thus more fields in Region 3, namely inside the MUT samples. This is the reason that MUT samples with higher ϵ_r' appear to "suck" the EM field into the sample from the resonator, as can be observed from FIGURE 3.6.To achieve higher sensitivity, low loss material is chosen for the resonator sensor. And thus in general, the MUT samples has higher loss than the resonator material, and therefore more field extends to the MUT samples leads to a higher loss, and hence lower resonance notch and broader 3-dB bandwidth of the resonance, a phenomenon revealed by FIGURE 3.5.

This nonideality of "coupling" between the sensor's response to large $\Delta\epsilon_r'$ and $\Delta\epsilon_r''$ prevents the analytical method to direct obtain $\Delta\epsilon_r$ from the ΔS_{21} curves. Curve fitting or look-up-table method can be used to infer the $\Delta\epsilon_r$ information from the simulated or measured ΔS_{21} curves. This section concludes the theoretical analysis of the WGM sensor. The following section discuss the practical implementation of a WGM sensor that is integrated in a high resolution complex permittivity sensing system.

3.4. Sensor Implementation

This section presents the implementation of a WGM resonator sensor which is particularly designed and implemented for a high resolution complex permittivity sensing system, which comprises a pair of complementary paths for the sensing and the reference signals and a LO feedforward path for the LO signal. More details of the motivations of the 3-path structure is discussed in Chapter 5.

3.4.1. Coupler Design and Sensor Assemble. The HR-Si DWG and the WGM resonator sensor need access to the THz source circuitry to receive excitation signals and pass the signal to the readout circuitry to process its response. More particularly, for the high resolution complex permittivity sensing system discussed in Chapter 5, the sub-THz signal should be transmitted from an integrated CMOS TX to the DWG from port 1, as shown in FIGURE 2.9, and then received by the CMOS RX from the DWG from port 2. We proposed a CPW-DWG coupler as an intermediate transmission structure to couple the sub-THz signal between the DWG and the CMOS IC's, as shown in FIGURE 3.7. Using a piece of 100-um thick quartz as substrate, the CPW is connected to the chip output pad via bonding wires. More details about the bonding wires are discussed in Subsection 5.4.1. The bonding wires are connecting the CPW on chip with the CPW on the quartz substrate, forming a GSGSGSG array for the 3 signal paths of the sensing path, the reference path and the LO path.

Comparing to the microstrip line coupler adopted in [**2**], the CPW coupler has the following advantages. First, it supports multiple paths inter-connect with the CMOS IC. By comparison, the microstrip line coupler requires an AC ground structure at the two sides of the signal path, preventing a parallel array of the signal paths. Secondly, on a 100-um thick quartz substrate, in

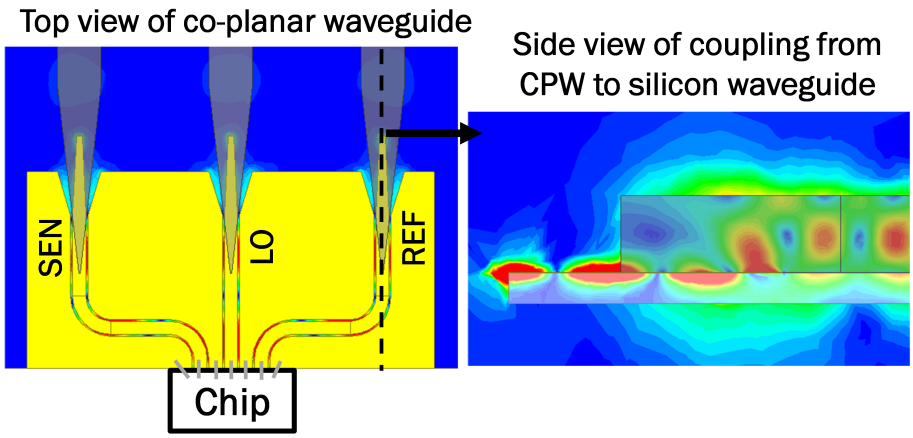

FIGURE 3.7. Top view of the interconnect of CMOS IC with DWG.

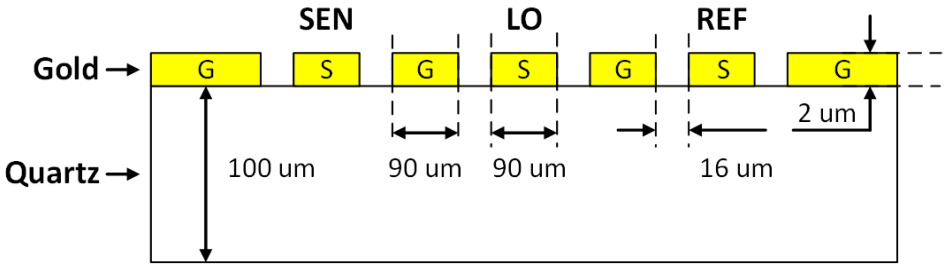

FIGURE 3.8. Cross section and dimensions of the CPW on quartz substrate (not drawn to scale).

order to have a 50 Ω characteristic impedance, a microstrip line needs to have a line width as wide as 150 um. This is larger than the quarter wavelength at 160-GHz frequency on a quartz substrate whose relative permittivity is $\epsilon = 3.78 - j0.0008$. With such a wide line width, loss due to mode conversion may occur. On the contrary, the characteristic impedance of the CPW can be controlled by the gap width between the signal line and the ground line, and therefore the signal line width can be narrower than the quarter wavelength to avoid potential mode conversion issue. The cross section and the dimensions of the CPW is shown in FIGURE 3.8. In order to have a 50 Ω characteristic impedance, the gap between the signal path and the ground metal is chosen to be 16 um and the width of the signal path is 90 um. The characteristic impedance has a relatively weak dependence on the signal path width than the gap, and the signal paths width and the ground path widths are determined to comply with the GSG pad dimensions of the CMOS IC. Lastly, the CPW coupler does not require a ground plane at the back side of the quartz substrate, halving the

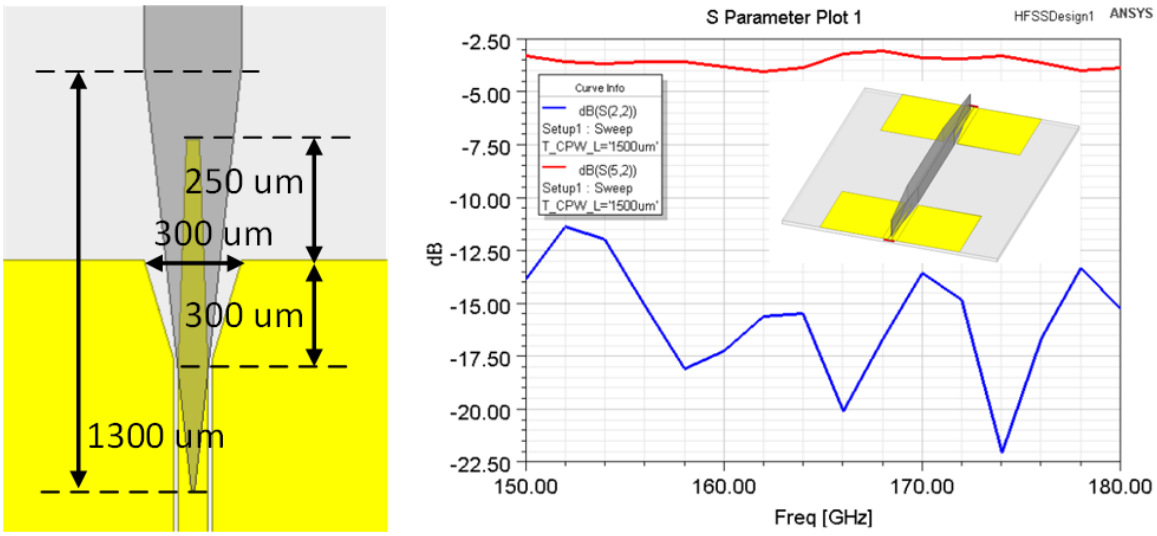

FIGURE 3.9. Finalized CPW-DWG coupler design and simulated insertion loss (red) and return loss (blue).

fabrication steps. The requirement for the thickness of the quartz substrate is also greatly relaxed for the CPW coupler comparing to the microstrip counter parts. The substrate thickness should be greater or equal to 100 um to be mechanically strong to facilitate the fabrication and packaging process. The CPW is to be realized by gold film on the quartz substrate and its thickness should be much larger than the skin depth in gold at sub-THz frequencies, which can be calculated by

$$\delta = \sqrt{\frac{1}{\pi f \mu \sigma}}. \tag{3.2}$$

where μ is the permeability of the gold film and sigma is the conductivity of gold. The skin depth is calculated to be below 200 nm for frequencies above 100 GHz. Therefore the CPW film thickness is determined to be 2 um to minimize its attenuation to the sub-THz signals. The fabrication process for the CPW coupler is described in the subsection of 3.4.3.

As shown by the EM field in the top view and the side view of the CPW coupler in FIGURE 3.7, the sub-THz signal couples into the DWG from the CPW through near field coupling. The design methodology of the coupling section is wave-impedance matching [**2**], as can be inferred from the taper sections of both the DWG and the CPW parts. The wave impedance of the $E_1^y 1$ mode propagating in the DWG along the vertical integration line is around 150 Ω, and hence the CPW's gap is increased in the taper section to increase its characteristic impedance. The detailed

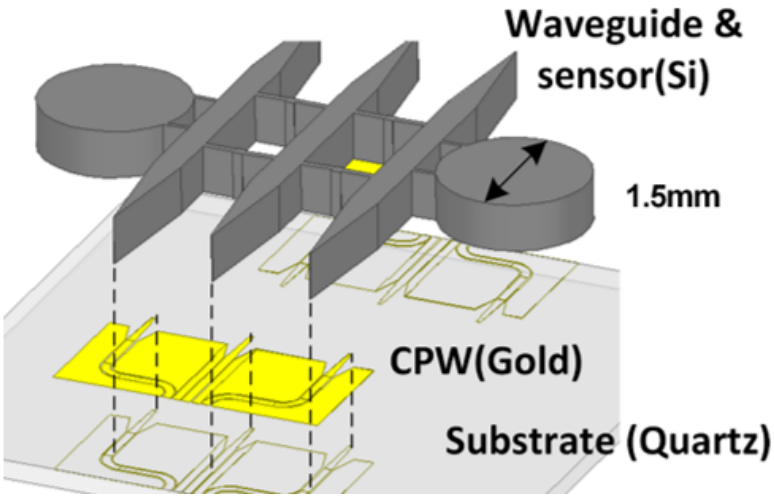

FIGURE 3.10. Sensor structure assemble.

dimensions of the coupler section are shown in FIGURE 3.9. The dimensions are optimized to have a low insertion loss and low return loss in the frequency range of interest, which is 150 GHz - 180 GHz in this particular implementation. The end-to-end structure of such a coupler is simulated to show the loss of the CPW-DWG coupler, as shown in FIGURE 3.9. After calibrating the path loss of the individual DWG and CPW section, the coupling loss of each of the CPW-DWG coupler is around 1.6 dB. The return loss is below -10 dB in the frequency range.

FIGURE 3.10 illustrates the assemble of the complete sensor structure that is used in the high resolution complex permittivity sensing system. The CPW realized by gold film is deposited on the top surface of the 100-um thick quartz substrate. And the HR-Si sensor structure needs to be glued on top of the CPW coupler with good alignment with the CPW coupler to achieve low coupling loss. The assemble process of the HR-Si sensor structure with the CPW on the quartz substrate is done with a flip-chip bonder Fineplacer by Finetech, which is a manual aligner / bonder that can achieve an alignment accuracy below 1 um. From simulation, a misalignment of 5 um between the center line of the DWG and the CPW will cause a increase of insertion loss of 3 dB. The assembled complete sensor structure is shown in FIGURE 3.11. Its performance is presented in the next subsection.

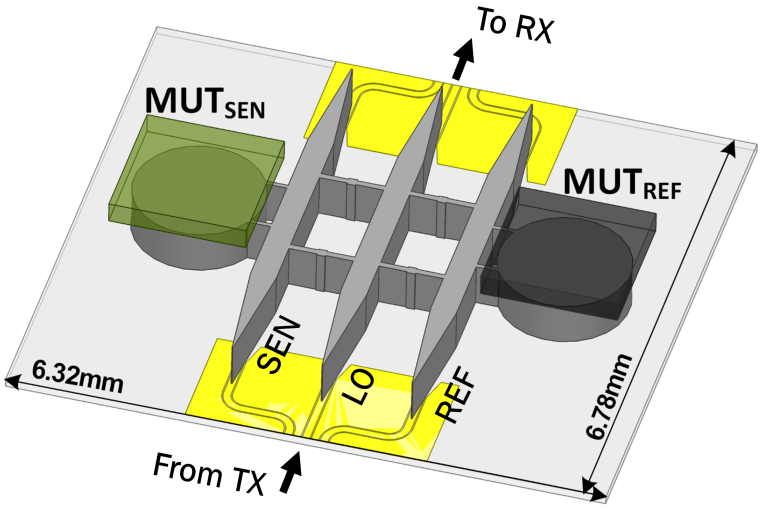

FIGURE 3.11. Complete sensor structure.

3.4.2. Sensor Performance. The complete sensor structure used in the high resolution complex permittivity sensing system described in Chapter 5 is shown in FIGURE 3.11, with MUT samples placed on top of the resonator sensors. The sensing path and the reference paths are identical mirrors of each other. The disk radius is determined to be 750 um to balance its quality factor and the size of the sensor. This radius also makes sure that the sensors' resonant frequencies are in the range of 150 GHz - 160 GHz for MUT samples with permittivity in the range of $\epsilon' = 1 - 6$. The gap between the resonator disk and the feeding DWG is 160 um to have the resonator be near critical coupling condition for MUT samples with with permittivity in the range of $\epsilon' = 1 - 6$ and $\epsilon'' = 0 - 0.1$.

As can be seen in FIGURE 3.11, both of the disks and the feeding DWG are connected with two narrow HR-Si arms. The purpose is to hold the WGM resonator disks with the DWG with fixed gap to ensure critical coupling by design. The width of the arm should be minimized to reduce its impact on the performance of the sensors. Their widths are determined to be 40 um to have enough mechanical strength to withstand common handling forces in the process of the fabrication. The two arms should also be placed far apart from each other to facilitate the fabrication process, described in more detail in the Subsection 3.4.3. Additional four arms are also added to hold the sensing and the reference paths DWG with the LO path DWG. In this way, the entire

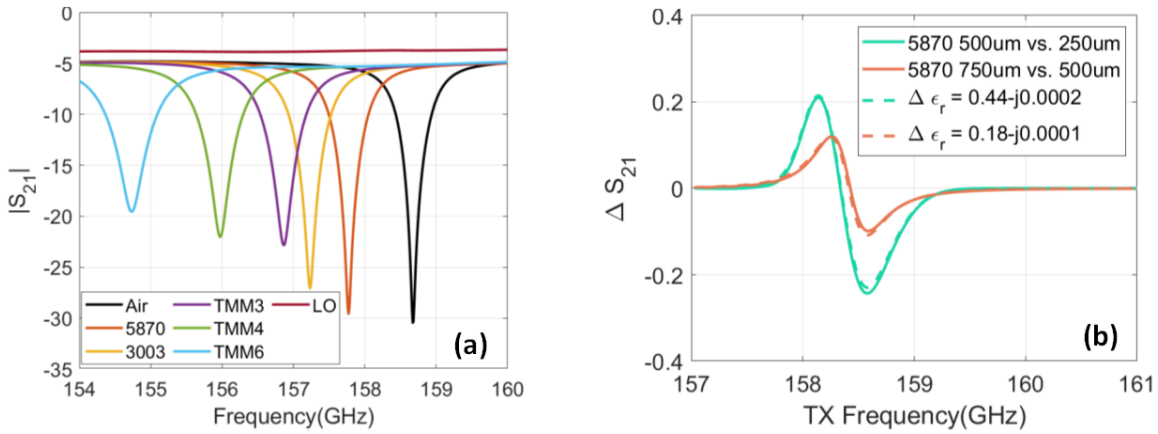

FIGURE 3.12. Measurement Setup (a) Block diagram. (b) Top view of the sensing area with MUT samples placed on top of the sensors in the progress of measurement.

sensor structure forms one single piece, which greatly facilitates the fabrication process and the alignment in the packaging process. The distances between the DWG are determined to be 800 um, far enough to make the coupling between the DWG negligible. The entire sensor structure has a dimension of 6.32 mm x 6.78 mm. With the sensing path and the reference path being identical, the simulated S_{21}'s of the sensing path of the sensor structure with different MUT samples are shown in FIGURE 3.12. The resultant Q is 246, which leads to the permittivity sensitivity of $Sen_{\epsilon_r'} = 0.96$ and $Sen_{\epsilon_r''} = 1.2$. 250-um-thick Rogers laminate samples are used as MUT's. The horizontal dimensions of the MUT's are 2 mm by 2 mm, to ensure full coverage of the sensor disk, as shown in FIGURE 3.11. As shown in FIGURE 3.12(a), to measure dielectric material with $\epsilon' < 6$, the operation frequency range requirement for the TRX IC is 6 GHz. Also, the LO path has an insertion loss of 4 dB, with 1.6-dB loss coming from the coupler of each side. As also shown in FIGURE 3.12(a), the Q of the sensor drops for MUT with larger ϵ_r'. Higher ϵ_r' of the MUT lowers the ϵ_r' contrast at the boundary between the sensor and the MUT, leading to less field confinement in the sensor and resulting in higher loss and hence lower Q. And higher ϵ_r'' directly lowers the Q of the resonator. The resultant lowered sensitivity leads to worse resolution, as shown by Eqn. 5.9. From simulation, a permittivity range of $\epsilon_r' = 1 - 6$ and $\epsilon_r'' = 0 - 0.1$ ensures a system resolution better than 0.1%.

The MUT sample's thickness can also affect the transmission. Thicker sample of the same material allows more evanescent field to extend from the resonator sensor to the sample, therefore

changing the effective permittivity experienced by the resonator. FIGURE 3.12(b) shows the simulated transmission difference of the sensing and the reference path when Rogers 5870 samples with different thickness are placed on the sensing and the reference paths. The transmission difference caused by the different thickness of the same material type can be equivalent to certain permittivity difference of material samples with the same thickness. Further more, it is observed from simulation that, when the sample thickness exceeds 1 mm, however, the sensor is insensitive to sample thickness variation. This is because the evanescent field decays fast inside the sample and there is negligible field above the height of 1 mm. Therefore, for accurate permittivity measurement, the sample should be prepared to have a thickness larger than 1 mm. On the other hand, the sensor is insensitive to the horizontal dimensions of the MUT samples as long as the sample covers the entire top surface of the sensor disk.

3.4.3. Sensor Fabrication and Measurement. The sensor is fabricated in the cleanroom of the University of California, Davis, Center for Nano and Micro Manufacturing (CNM2). The HR-Si sensor structure is fabricated via deep silicon etching. The sensor structure, which is the area to be preserved, is covered and protected by photoresists patterned via lithography process. The exposed areas are etched away by the etching plasma in the deep silicon etching process. More detailed procedures are described in [**1**]. 120 sensor samples are patterned on a single 4-inch HR-Si wafer, with a dimension variations in the range of +- 20 um, to compensate the random dimension variations caused by uncertainty of the density distribution of the etching plasma. FIGURE 3.13(a) shows the matrix of 120 sensor structures on a HR-Si wafer after the deep silicon etching. The white regions on the wafer are the regions where the silicon is etched away. The non-uniform plasma causes the dimensions of the sensors to deviate from the designed values. For example, some samples' resonator disks are under-etched and therefore has a larger diameters, which result in lower resonant frequency than the designed resonant frequency. Among the non-uniform 120 samples, about 20 with the resonant frequencies in the designed range are picked. Another non-ideality caused by the non-uniformity of the etching process is the slight dimension difference between the WGM resonator disks of the sensing path and the reference of the same sensor structure. This results in different intrinsic resonant frequencies of the sensing path sensor and the reference path sensor, which means that a resonant frequency difference between the two paths can be observed

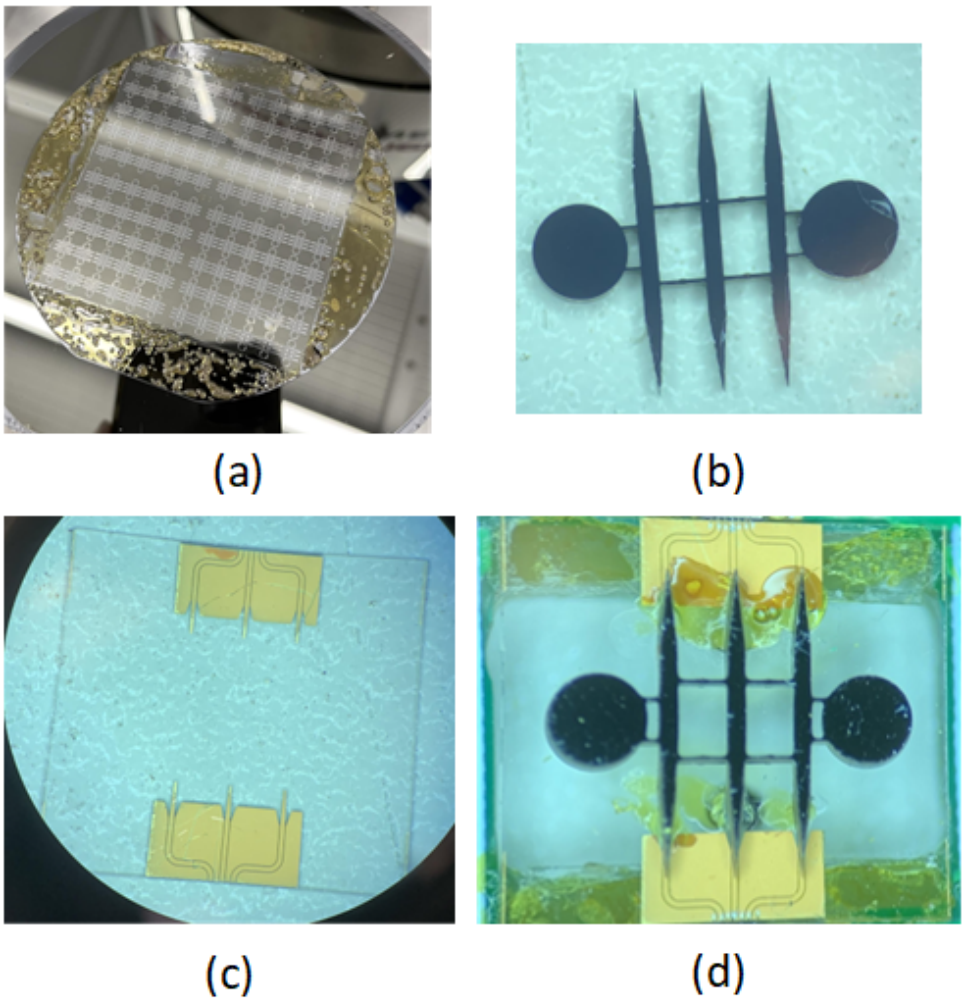

FIGURE 3.13. Sensor structure fabrication (a) Array of the sensors on a HR-Si wafer after deep silicon etching. (b) HR-Si sensor. (c) CPW on the 100-um thick quartz substrate. (d) Assembled sensor structure with HR-Si sensor attached to the substrate with BCB as the glue.

even when no MUT's are on neither of the sensor disks. From the measurement of multiple samples, an average of 50 MHz-frequency difference between the sensing path and the reference path is observed. This frequency offset, however, can be calibrated out since it is static. FIGURE 3.13(b) shows one of the sensor structure samples taken from the wafer after the completion of the deep silicon etching process.

The CPW coupler on the 100-um thick quartz substrate in fabricated in the university cleanroom through steps of lithography, electron-beam evaporation and gold plating. The steps are the same

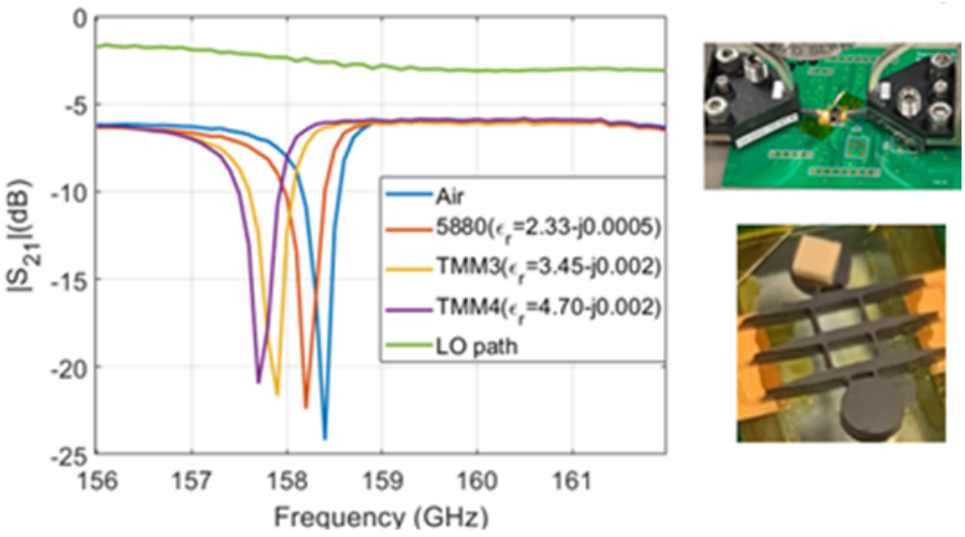

FIGURE 3.14. Sensor measurement.

as described in [**2**]. The fabricated quartz substrate with the CPW coupler is shown in FIGURE 3.13(c).

The mounting of the HR-Si sensor structure with the quartz substrate is completed in the UC Davis FIT lab of the Physics Department. A flip-chip bonder Fineplacer by Finetech is used to align and mount the HR-Si sensor structure with the CPW coupler on the quartz substrate. Benzocyclobutene (BCB) is used as the adhesive to bond sensor structure and the substrate together. The complete sensor after the bonding is shown in FIGURE 3.13(d).

The S-parameters of the complete sensor is then measured using network analyzer with G-band (140 GHz - 220 GHz) frequency extender and G-band probes, as shown in FIGURE 3.14. Rogers substrate materials are used as MUT samples and are placed on top of the sensor disk of the sensing path. The MUT samples available in the lab has smaller dimensions than the sensor disk, and are unable to cover the entire top surface of the sensor. This results in smaller frequency shifts comparing to the simulation results in which samples with dimensions that are large enough to cover the entire sensor disks are used. Another issue with the MUT with smaller dimensions than the disk is that the measurement results also depend on the positioning of the MUT samples on the top of the sensor disk. It is observed from the measurement that the sensitivity is lower when the MUT samples are placed at the center of the disk and otherwise higher when placed near the edge

of the sensor disk. This is because the evanescent E field is distributed near the outer perimeter of the sensor disk, as shown in FIGURE 2.4

CHAPTER 4

Low Power Permittivity Sensing System

This work demonstrated a novel sensing system that features state-of-the-art resolution of low loss dielectric constant measurement at sub-THz due to the design of the novel sub-THz dielectric ring resonator sensor and the low noise sub-THz receiver. Dielectric ring resonator has been proven to have high sensitivity in optical domain, and it is adopted in this work due to its high quality factor and high sensitivity at sub-THz frequency comparing to metal-insulator-metal transmission line structure such as microstrip line based resonator. In the proposed sensing system, a CMOS sub-THz transmitter provides excitation and thus eliminates the need for external high frequency source. A CMOS sub-THz receiver that detects small power difference eliminates the need for high speed readout equipment. The high sensitivity ring resonator sensor and the low noise receiver bring down the minimum dielectric constant change ($\Delta\epsilon_r$) detection limit to 3.10×10-4 for a integration time of 10us. The system consumes 9 mW DC power.

4.1. Sensing System Design

FIGURE 4.1 shows the diagram of the dielectric sensing system. The sensing system consists of a transmitter, a sensor, and a receiver. The transmitter (TX) is a fundamental frequency oscillator, which generates a 162 GHz continuous wave (CW) tone and feeds it to the sensor. The sensor is essentially a resonator that resonates around 160 GHz when no MUT is present.

Different MUT's with different dielectric constants shift the sensor resonant frequency, thus resulting in different attenuation of the 162 GHz sinusoidal tone generated by the TX. The receiver (RX) then detects the power level of the tone at the sensor output and converts the attenuated 162GHz CW signal's power to a low frequency output voltage signal for easy processing. The higher the MUT sample dielectric constant, the lower the sensor's resonant frequency shifts down. Thus, with higher dielectric constant MUT sample, the 162GHz sinusoidal tone is further away from the sensor resonant frequency, getting higher attenuation and resulting in lower power detected by the

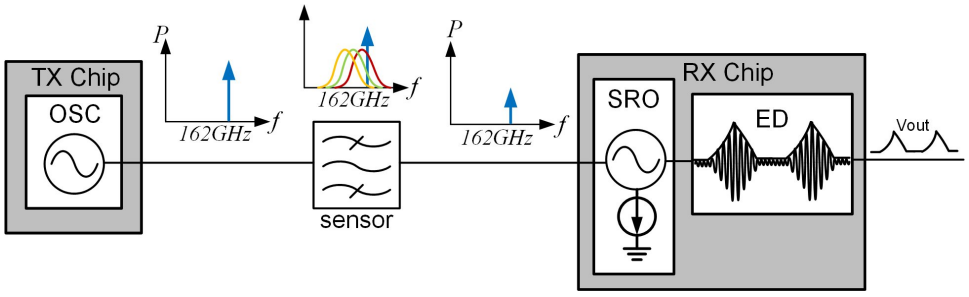

FIGURE 4.1. Sensor measurement.

receiver, which is thus reflected by the receiver output voltage.

The ring resonator based sensor essentially transduces dielectric constant difference into attenuation difference, and thus the output power difference for a given input power. Here we define sensor transduction ST to be the output power difference due to unit dielectric constant change for a given input power:

$$sensor\ transduction = S_T = \frac{\partial P_{out}}{\partial \epsilon_r}|_{P_{in}} \tag{4.1}$$

The key specification of the proposed sensing system is the minimum detectable dielectric constant change, or resolution. It is determined by the ratio of receiver sensitivity, or the minimum detectable signal of the receiver, ΔP_{min}, and the sensor transduction:

$$resolution = \frac{receiver\ sensitivity}{sensor\ transduction} = \frac{\Delta P_{min}}{\frac{\partial P_{out}}{\partial \epsilon_r}|_{P_{in}}} \tag{4.2}$$

4.2. Sensor Design

The ring resonator based sensor is the core sensing component of this sensing system. It is essentially a band pass filter realized by a silicon dielectric ring resonator coupled to rectangular silicon dielectric waveguide mounted on a quartz substrate, as shown in FIGURE 4.2. The gray structure is the silicon waveguide and the two white cubes are samples of MUT that are put on the top of the two identical rings, which is the sensing area. Input signal is fed from port 1 and propagates along the microstrip line before it couples to the waveguide through the transition [**49**]. Signal is picked-up by the ring from input waveguide and dropped to the middle waveguide at the rings resonant frequency, as shown by the E field distribution in the inset of FIGURE 4.2. For signal frequency away from the ring's resonant frequency, the coupling between the waveguide and

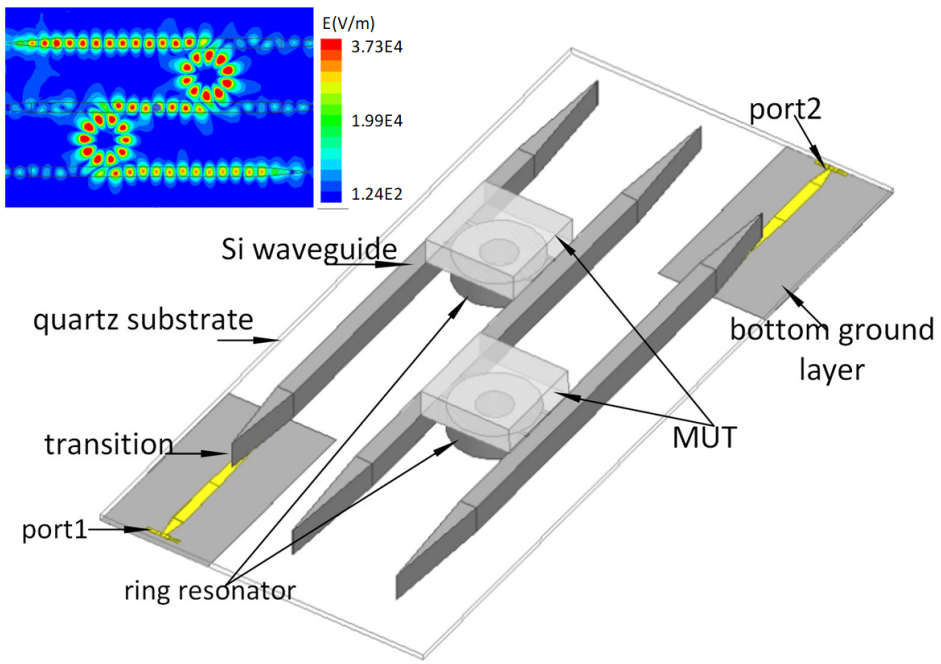

FIGURE 4.2. 3-D model of the band pass WGM ring resonator sensor, and the E field distribution at resonant frequency (inset).

the ring is weaker, resulting in a larger attenuation. The signal is then coupled to the output waveguide by the second ring in the same manner and propagates to port 2. The tapered ends of the silicon waveguides serve as impedance matching to prevent the signal from reflecting back to introduce unintended interference.

The ring's resonant frequency is affected by the effective dielectric constant of the wave travelling in the ring, same as the equation describing the WGM disk resonator, Eqn. 2.3. Also similar to the disk resonator sensor, for a given mode m, when the rings' dielectric constant environment increases, the resonant frequency decreases.

Here we define 3 key specifications in order to maximize the sensor transduction S_T defined in Eqn. 4.1:

$$S_T \propto S_{sens} \cdot I_{rsnt} \cdot Q_L \tag{4.3}$$

S_{sens} is defined to be the sensitivity of resonator sensor, quantified by the resonance frequency shift per unit dielectric constant change:

$$S_{sens} = \frac{\partial f_r}{\partial \epsilon_r} \tag{4.4}$$

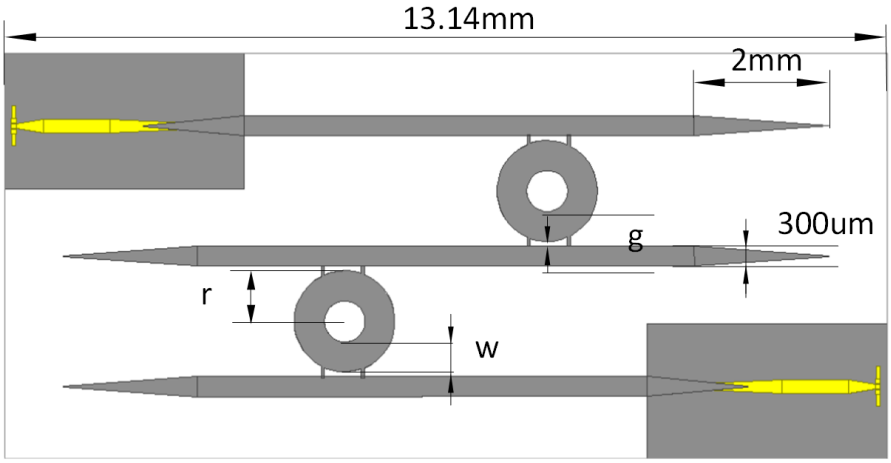

FIGURE 4.3. Dimensions of the band pass WGM ring resonator sensor.

I_{rsnt} is defined here to be the resonance intensity of the ring resonator, which can be quantified by the out-of-band rejection of the resonator:

$$I_{rsnt} = \frac{|S_{21}|_{max}}{|S_{21}|_{min}} \tag{4.5}$$

where $|S_{21}|_{max}$ and $|S_{21}|_{min}$ are the maximum and minimum respectively of the magnitude of S_{21} in the frequency range of interest as shown in FIGURE 4.4.

Q_L is the loaded quality factor of the ring resonator, describing the sharpness of the resonance:

$$Q_L = \frac{f_r}{BW_{3dB}} \tag{4.6}$$

The relationship between these key specifications to the dimension of the sensor is described as follows. The sensitivity is proportional to the sensing area of the ring resonator. Therefore, larger ring radius r and width w are desired. w also determines the mode's cross section profile and should be close to that of the waveguide's to avoid mismatch and thus improving coupling. The resonance intensity is largely determined by the coupling between the ring and the waveguide, or in terms of design parameter, the gap g between the ring and the waveguide. Maximum resonance intensity happens when critical coupling between the ring and the waveguide is achieved [**35**]. Q_L is limited by the unloaded quality factor Q_U, namely the loss of the ring itself, and external quality factor

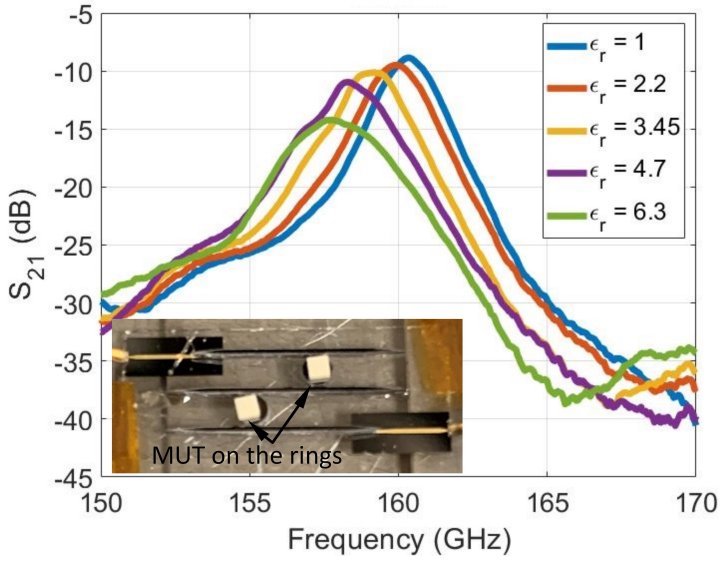

FIGURE 4.4. Measured S_{21} of the WGM ring resonator sensor with different MUT samples placed on top of the ring sensor.

Q_e, namely the loss of the waveguide structure:

$$\frac{1}{Q_L} = \frac{1}{Q_e} + \frac{1}{Q_U} \tag{4.7}$$

As scattering loss is the dominant factor of the loss of the ring, larger ring leads to more loss due to longer trip distance for the wave travelling inside the ring. Due to the loss of the loading waveguide, stronger coupling, namely smaller g, further lowers Q_e, and consequently, Q_L. To achieve optimal sensor transduction, the radius r, ring width w and gap g were found by simulation to be 760 um, 460 um and 65um, respectively. The sensor is fabricated in the cleanroom and has a size of 13.14 mm $\times$ 6 mm. Its sensitivity is verified by sensing low loss dielectric material with known dielectric constant, as shown in FIGURE 4.4. The S_{21} with different dielectric being sensed is measured with Network Analyzer (Keysight N5247A) with G band extender. The resonator sensor sensitivity is 0.3 GHz frequency shift per unit dielectric constant change. The resonance intensity is 30 dB and the peak Q_L is 86.7. The drop of quality factor and resonance intensity for higher dielectric MUT is due to the wavelength mismatch between the waves in the waveguide and in the ring. FIGURE 4.5 shows the sensor's attenuation to a 162 GHz signal and the sensor's output power for a -6 dBm input power. As the dielectric constant of the MUT changes from 1 to 2.2, the output power

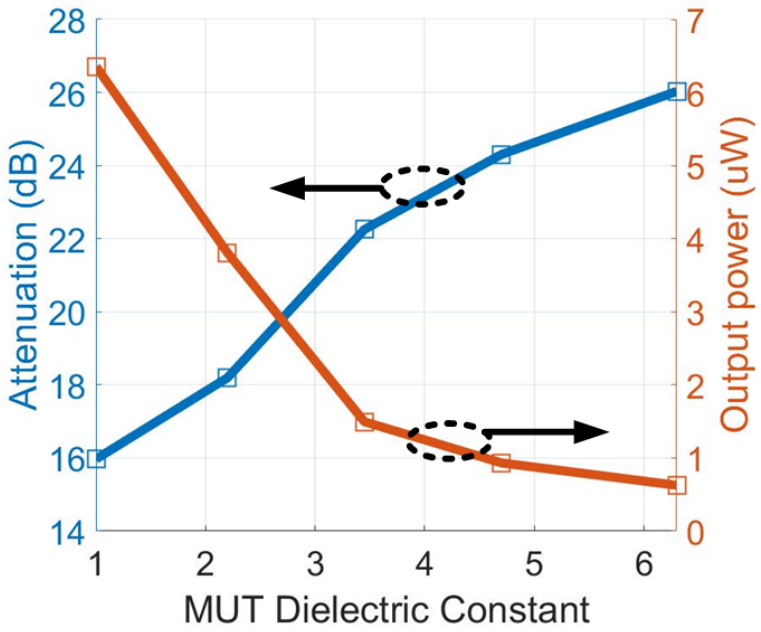

FIGURE 4.5. Attenuation to 162 GHz signal and sensor output power given -6 dBm input power.

decreases from 6.35 uW to 3.80 uW. Based on Eqn. 4.1, this corresponds to a sensor transduction of 2.55 uW per unit dielectric constant change. Similarly, the worst sensor transduction is found to be 0.31 uW per unit dielectric constant change when the MUT dielectric constant change from 5 to 6. The sensing mechanism suggests that the transduction is also a function of the MUT loss and thickness. Simulation shows that the attenuation increases less than 0.1 dB when MUT loss tangent increases 0.01. Namely, to achieve a detection limit of 3.10×10^{-4}, the loss tangent difference of the MUT's should be less than 0.0001. Also, when the MUT sample's thickness is larger than 1 mm, the thickness variation has negligible effects on the sensing result.

4.3. Transceiver design

To effectively detect miniature change of the power level of the received tone due to small dielectric constant change of the MUT, a low-noise receiver around 162GHz is required. The topology adopted in this work is a super-regenerative receiver. Due to its Q-enhancement property, it can achieve very high sensitivity with a moderate noise figure by limiting its bandwidth [**50**] [**51**]. In this work, super regenerative receiver takes the form of a cross-coupled pair oscillator followed

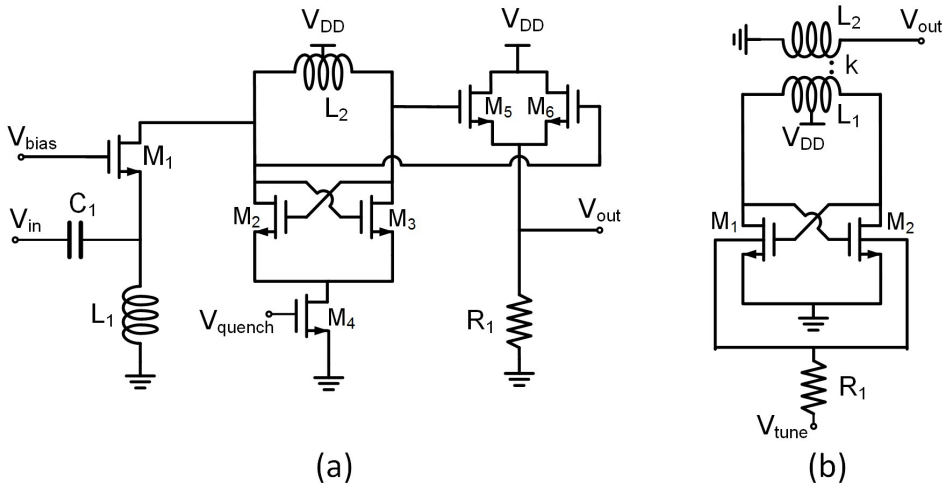

FIGURE 4.6. Circuit schematic of (a) receiver and (b) transmitter.

by an envelope detector. The circuit schematic is shown in FIGURE 4.6 (a). M2 and M3 are the cross-coupled transistor pair. The inductor L2 together with the parasitic capacitance of the transistors form the resonant tank. The current flowing in M2 and M3 is controlled by the tail current source M4, whose gate voltage is controlled by an external quench signal. Thus, the effective transconductance of the oscillator is controlled by the quench signal. M1 serves as a buffer between the oscillator and the input of the receiver. C1 and L1 serves as input matching network to 50 Ohms as well as DC block and DC current path. M5, M6 and R1 forms the envelope detector that extract the oscillation envelope, Vout. This is the envelope of the periodic oscillation, which is measured off-chip.

The receiver is implemented in a 28-nm bulk CMOS, and takes chip area of 357 um x 600 um. An on-wafer probe measurement of receivers is conducted. A 200 MHz sine wave with 200mV DC offset and 250 mVpp is used as quench signal to bias the super regenerative receiver in linear operation mode. Therefore the output voltage is a 200-MHz envelope signal, which is measured with spectrum analyzer. FIGURE 4.7 (a) shows the measured output voltage while input power is swept. The sensitivity of the receiver is measured to be -61 dBm, or 0.79 nW with resolution bandwidth to be 100 kHz (corresponding to integration time of 10 us). The power consumption of the receiver is 3 mW with 0.9 V supply voltage.

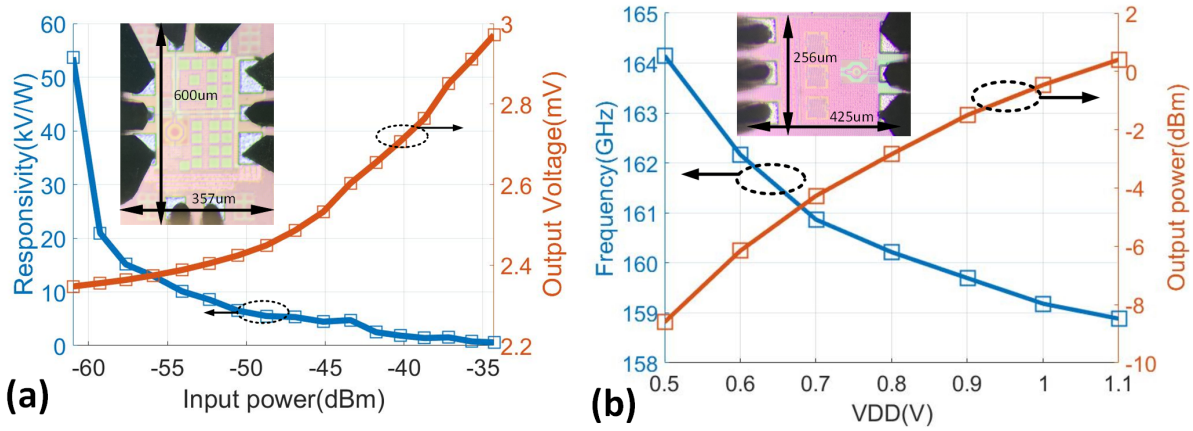

FIGURE 4.7. Measurement results and chip micrograph of (a) RX and (b) TX.

The transmitter takes form of a transformer-based fundamental frequency cross-coupled pair oscillator, whose schematic is shown in FIGURE 4.6(b). The transformer X1 is designed so that it not only provides the inductance for the resonant tank, but also works as impedance transformer to alleviate the 50 Ohm loading to the oscillator [**52**]. The cross-coupled transistor pair M1 and M2 are co-designed with the transformer to have good DC-RF efficiency, as well as enough output power [**53**]. Body tuning is used to allow frequency tuning. The current limiting resister R1 of 1K Ohms is added to protect the transistors. The transmitter is implemented in a 65-nm bulk CMOS and takes 370 um x 420 um chip area. The measured output frequency and out power vs. supply voltage is shown in FIGURE 4.7 (b). 0.6-V supply voltage is used to have 162 GHz output frequency. The corresponding output power is -6 dBm with DC power consumption of 6 mW.

4.4. Sensing System Measurement

As shown in the FIGURE 4.8 (a), the transmitter, sensor and receiver are assembled together on a PCB board. The transmitter's output ground-signal-ground (GSG) pad is wire bonded to the input GSG pad of the sensor, and the receiver's input GSG pad is wire bonded to the sensor's output GSG pad. The 162 GHz CW tone generated by the transmitter propagates through the sensor and gets detected by the receiver. The receiver's time-domain output waveform is measured by an oscilloscope and is shown in FIGURE 4.8 (b). The waveform is the envelope of the quenched regenerative oscillation, and the amplitude of the envelope is determined by the sub-THz input

power detected by the receiver. As shown in FIGURE 4.8 (c), the amplitude of the output waveform is also measured with spectrum analyzer, which is the amplitude of the tone at the frequency of 200 MHz due to the 200 MHz quench frequency. The noise floor of the sensing system is also measured with the spectrum analyzer to be -95 dBm with a resolution bandwidth (RBW) of 100 kHz, which corresponding to an integration time of 10 us. When sample of MUT with higher dielectric constant are placed on the rings, the tone was attenuated more and the receiver outputs a tone with smaller amplitude. FIGURE 4.8 (d) shows the system's output signal power varies with different standard dielectric material being sensed. For example, when the Rogers 5880 dielectric samples are placed on the sensor, which has a 1.2 permittivity difference with air, the system outputs a 49 uV voltage difference. Therefore, the measured sensing resolution can be calculated as

$$Resolution = \frac{1.2}{49uV/4.0uV} = 0.098. \tag{4.8}$$

where 4.0 uV is the voltage noise floor of the sensing system output, calculated based on the measured -95 dBm on the 50 Ohms load of the spectrum analyzer. On the other hand, the minimum detectable dielectric constant change is calculated from Eqn. 4.2 based on the measured sensor transduction and receiver sensitivity:

$$Resolution = \frac{0.79nW}{2.55uW/unit\,dielectric\,constant} = 3.10 \times 10^{-4}. \tag{4.9}$$

For dielectric constant larger than 6, the resolution degrades due to the larger mode mismatch between ring resonator and the dielectric waveguide. This resolution, however, is calculated based on the measurement performances of the WGM ring resonator sensor and the RX, and therefore the impact from the TX noise is not taken into consideration. This may results in an overly optimistic estimation of the permittivity sensing system resolution. In addition, this system cannot distinguish complex permittivity of the MUT samples, which results in a relatively low specificity for the dielectric material detection. Based on these aspects of the potential improvement, a more sophisticated sensing system is proposed and presented in the next chapter, which has the capability of suppressing the TX noise and of detecting complex permittivity.

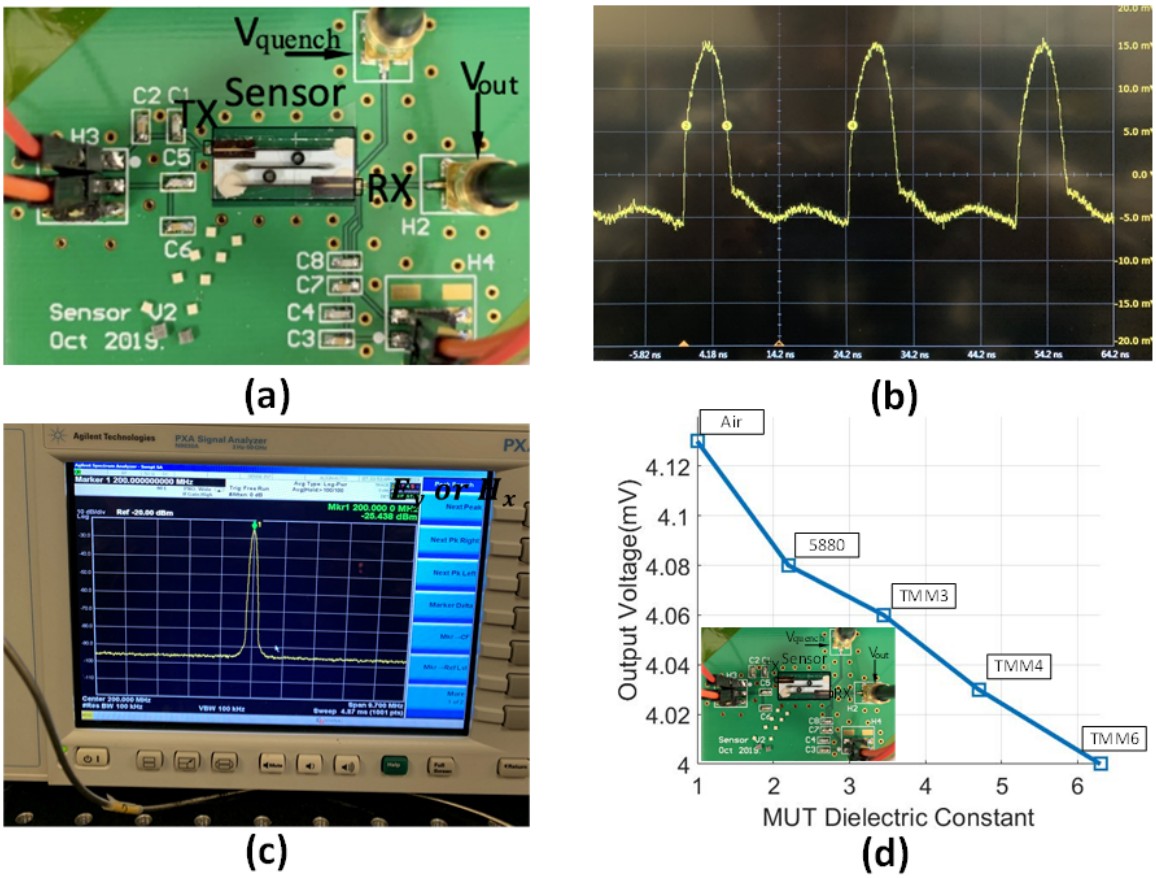

FIGURE 4.8. Sensing system measurement (a) Integrated system setup. (b) System output waveform, which is the envelope of the regenerative oscillation of the received, whose amplitude reflects RX detected power. (c) System output measured with spectrum analyzer. (d) System output voltage measured by spectrum analyzer with different dielectric samples placed on the sensor rings.

CHAPTER 5

High Resolution Complex Permittivity Sensing System

5.1. System Architecture and SNR Analysis

5.1.1. System Architecture. FIGURE 5.1 shows the system architecture. The TX outputs a complementary pair of BPSK modulated sub-THz signals through two identical off-chip silicon WGM disk resonator sensors near their band-stop resonant frequency, which are then summed by the combiner of the RX. The resulting signal reflects the transmission difference ΔS_{21} between the sensing and the reference path, which is then down converted by the RX mixer. The proceeding chopper up-converts the low frequency noise and the following integrator filters out the high frequency noise. The complementary BPSK signaling for the sensing and the reference paths suppresses both low frequency noise from the electronics and the impact from the ambient temperature variation. The summation of the complementary signals at the input of the RX reduces signal amplitude at the input of the mixer, which reduces the TX noise impact and mitigate the trade-off between noise and linearity for the RX circuitry. The TX injection-locks the RX LO through a low loss sub-THz LO feedforward path to suppress the TX's close-in phase noise in the down-conversion process at the RX. The architectural combination of balanced sensing and reference path and the LO feedforward overcomes the drift and high close-in phase noise of a THz free running VCO, leading to a high sensing resolution. The following subsections presents the quantitative analysis of the signal and noise of the sensing system that guides the design of the TRX circuits.

FIGURE 5.2 illustrates the signal and noise propagation of the system qualitatively in frequency domain. The VCO generates a CW tone at its oscillation frequency ω_{OSC} with phase noise. The TX chopper modulates the CW tone into BPSK at the modulation frequency of ω_{CHOP}, generating two sidebands at $\omega_{OSC} + \omega_{CHOP}$ and $\omega_{OSC} - \omega_{CHOP}$. The higher order harmonics of the BPSK modulation at frequencies of $\omega_{OSC} \pm 3\omega_{CHOP}$ and $\omega_{OSC} \pm 5\omega_{CHOP}$, etc., are omitted in this illustration for simplicity. As an architecture design of the TX signaling, the TX chopper drives

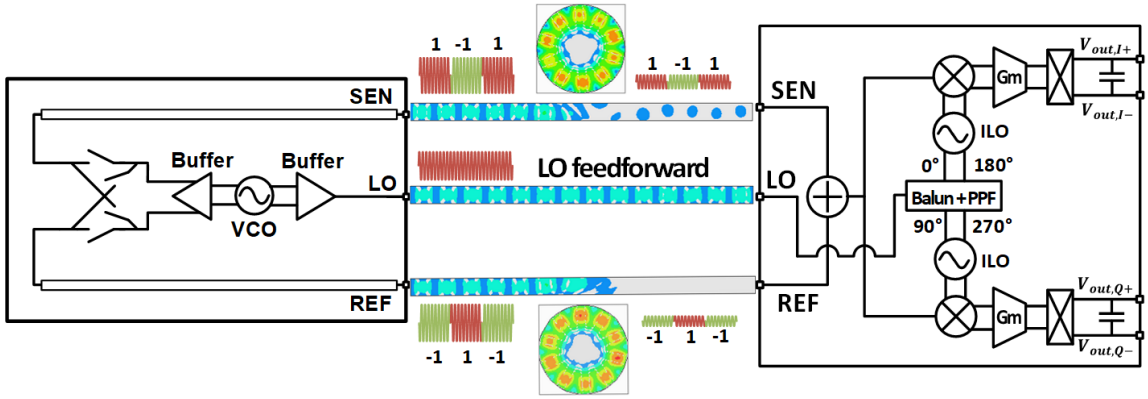

FIGURE 5.1. Sensing system architecture.

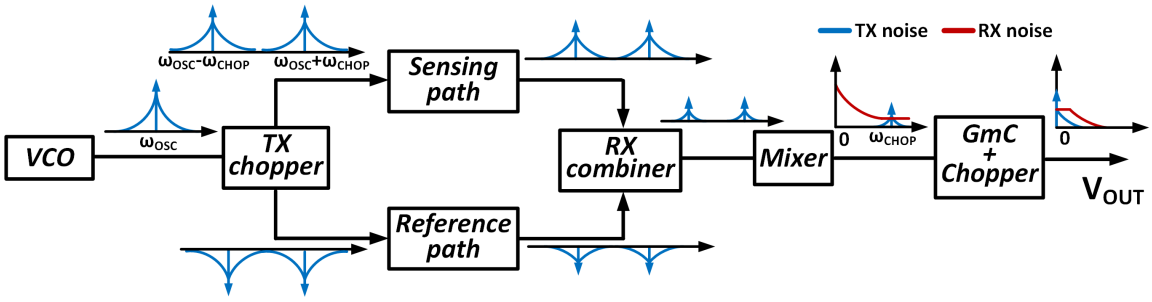

FIGURE 5.2. Illustration of signal and noise propagation.

the sensing path and the reference path with alternative phases, also incorporate the functionality of a power spliter and differential-to-single-ended converter, saving power and area. And thus, the signals at the output of the TX chopper have opposite signs, hence the name complementary BPSK signaling for the TX output. Comparing to the OOK type of modulation and signaling of the prior arts [**54**], this architectural innovation helps eliminate a strong carrier at ω_{OSC} at the input of the RX. This greatly suppresses the phase noise transmitted to the RX by the carrier, as well as relaxes the linearity requirement of the RX.

Passing through the sensing path and the reference path, the signals are attenuated by different levels, resulting from the different S_{21} of the two paths. The signals are then summed at the combiner of the RX. The summing of the complementary signals results in a residue signal that reflects the transmission difference of the sensing path and the reference path, or $\Delta S_{21} = S_{21,SEN} - S_{21,REF}$. This signal is then demodulated by the RX mixer, driven by the LO that is fed forwarded by the TX and has a frequency of ω_{OSC}, to the baseband. This baseband signal is a square wave with

fundamental frequency of ω_{CHOP}. The phase noise associated with the signal is suppressed in this downconversion process due to its coherence with the phase noise of the LO. The phase noise of the two sidebands $\omega_{OSC}+\omega_{CHOP}$ and $\omega_{OSC}-\omega_{CHOP}$ at the input of the mixer is also folded in-phase into ω_{CHOP} at the output of the mixer, resulting the factor of four in the TX noise power in Eqn. 5.2. Nonetheless, the TX noise is still lower than the RX noise, which is marked as a red curve, as determined by the simulation shown in FIGURE 5.9. The square wave signal is then demodulated down to DC by the RX chopper and amplified by the GmC integrator. And the flicker noise of the mixer and the OTA is upconverted by the chopper and filtered out by the integration capacitor. The systematic design of the architecture and the signaling suppresses the TX noise and the RX noise effectively while preserving and amplifying the signal at the the same time, resulting a high SNR at the system output. Detailed SNR analysis is carried out quantitatively in the following sections.

5.1.2. Signal Analysis. The signal flow of the system is analyzed within a half chopping cycle, because the system operates in steady state as if the signal is in CW mode. This avoids the unnecessary complexity and difficulty in analyzing the signal with the higher order modulation harmonics, and ensures correctness in theory, as proved quantitatively by comparing with the circuit simulation results in FIGURE 5.10. The system signal flow is illustrated in FIGURE 5.3. $V_{TX,SEN}=\sqrt{P_{TX}Z_0}$ and $V_{TX,REF}=-\sqrt{P_{TX}Z_0}$ are the rms signal voltages at the output of the TX to the sensing paths and the reference paths, respectively. P_{TX} is the TX output power to the sensing path and the reference path, and $Z_0=50\Omega$. $V_{RX,SEN}=\sqrt{P_{TX}Z_0}S_{21,SEN}$ and $V_{RX,REF}=-\sqrt{P_{TX}Z_0}S_{21,REF}$ are the signal voltages at the input of the RX to the sensing paths and the reference paths, respectively. $S_{21,SEN}$ and $S_{21,REF}$ are the transmission of the sensing path and reference path, respectively, and are both complex quantities. The RX sums these two signals before down converting and amplification. The magnitude of the RX output signal,$V_{sig,out}$, can

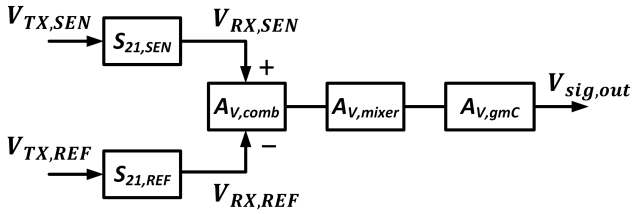

FIGURE 5.3. System signal flow.

therefore be given by

$$\begin{aligned} V_{sig,out} &= \left| \sqrt{P_{TX} Z_0} S_{21,SEN} - \sqrt{P_{TX} Z_0} S_{21,REF} \right| \\ &\quad \cdot A_{V,comb} \cdot A_{V,mixer} \cdot A_{V,gmC} \\ &= \sqrt{P_{TX} Z_0} \left| S_{21,SEN} - S_{21,REF} \right| \\ &\quad \cdot A_{V,comb} \cdot A_{V,mixer} \cdot A_{V,gmC} \\ &= \sqrt{P_{TX} Z_0} |\Delta S_{21}| \cdot A_{V,comb} \cdot A_{V,mixer} \cdot A_{V,gmC} \\ &= \sqrt{P_{TX} Z_0} Sen_{\epsilon_r} \Delta\epsilon_r A_{V,RX} \end{aligned} \tag{5.1}$$

where $A_{V,comb}$ is the voltage gain(loss) of the RX combiner, $A_{V,mixer}$ is the conversion gain of the mixer , $A_{V,gmC}$ is the DC gain of the gm-C integrator, and $A_{V,RX} = A_{V,comb} \cdot A_{V,mixer} \cdot A_{V,gmC}$ is the total voltage gain of the RX. For conciseness, the system analysis in the rest of this article is based on ϵ_r, which is a representation of either ϵ_r', or ϵ_r'' without loss of specificity. For example, Sen_{ϵ_r} can represent either $Sen_{\epsilon_r'}$ and $Sen_{\epsilon_r''}$. As can be seen, the output signal of the sensing system is proportional to the sensitivity of the sensor and the permittivity difference between the MUT on the sensing path and the reference path sensors.

5.1.3. Noise Analysis. Both TX and RX generate noise. The major source of the TX noise is the phase noise of the TX VCO, which is converted to amplitude noise in the direct conversion process of the RX mixer. The TX noise power density at the output of the TX can be modelled as $P_{TX} Z_0 L_{TX}(f)$, where $L_{TX}(f)$ is the phase noise of TX signal in unit of dBc/Hz. As the TX noise is essentially the phase noise of signal carrier, it follows a similar process of the signal flow. At the output of the RX combiner, the TX noise power density is $P_{TX} Z_0 L_{TX}(f) Sen_{\epsilon_r}^2 \Delta\epsilon_r^2 \cdot A_{V,comb}^2$. At the output of the mixer, the TX noise power density becomes $P_{TX} L_{TX}(f) Sen_{\epsilon_r}^2 \Delta\epsilon_r^2 \cdot$

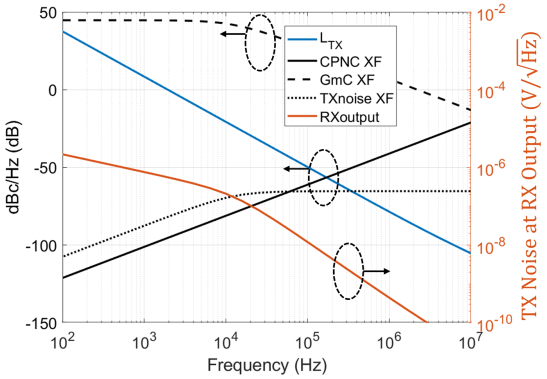

FIGURE 5.4. L_{TX}, TX noise at the RX output and its transfer functions

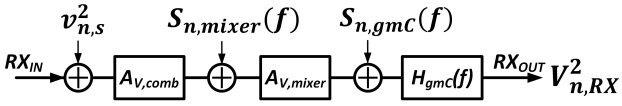

FIGURE 5.5. RX noise model.

$A_{V,comb}^2 A_{V,mixer}^2 4|1-e^{-j2\pi f t_d}|^2$. The factor 4 is due to the summing of the USB and the LSB of the phase noise at output of direct conversion. $|1-e^{-j2\pi f t_d}|$ is the coherent phase noise cancellation (CPNC) effect in the down conversion process, where t_d is the time delay difference between the RF and LO signals at the mixer, which is simulated to be 1.4 ns due to the high quality factor of the resonator sensor [**55**]. With its high pass feature, it suppresses the close-in phase noise. After passing the gm-C integrator, the total TX noise at the RX output can then be given by

$$V_{n,TX}^2 = \int_{f_L}^{f_H} P_{TX} L_{TX}(f) Z_0 (Sen_\epsilon \Delta\epsilon)^2 A_{V,comb}^2 A_{V,mixer}^2 4|1 - e^{-j2\pi f t_d}|^2 |H_{gmC}(f)|^2 df \quad (5.2)$$

where $H_{gmC}(f)$ as in Eqn. 5.2 is the transfer function of the time-windowed integrator and is derived in Appendix B. The transfer function of the CPNC process and the overall RX on the TX noise, and the TX noise power spectral density at the RX output are plotted in FIGURE 5.4. Also, in Eqn. 5.2, to precisely quantify the integrated TX noise voltage at the RX output, the lower bound of the integration f_L is chosen to be 100 Hz, which is much lower than the integration clock cycles of 50 kHz, and the upper bound of the integration f_H is chosen to be 100 MHz, which is much higher than the Gm-C corner frequency of 20 kHz.

FIGURE 5.5 shows the noise model of the RX. $v_{n,s}^2 = 2kTZ_0$ is the KT noise of the 50Ω source impedance of the two-input RX. The input-referred noise power density of the mixer can be

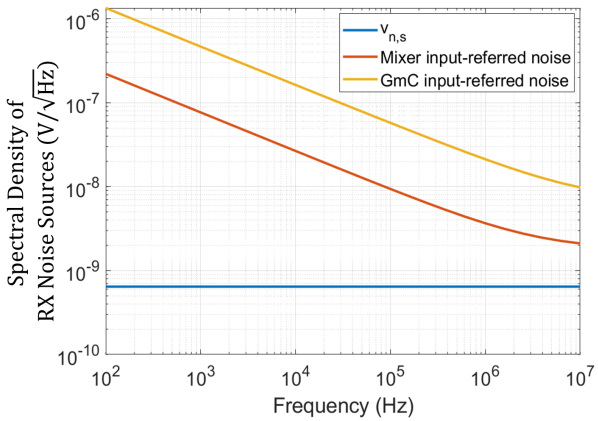

FIGURE 5.6. Simulated RX noise.

modelled as a combination of the mixer's thermal noise and flicker noise

$$S_{n,mixer}(f) = v_{n,mixer}^2 + \frac{k'_{mixer}}{f} \tag{5.3}$$

where $v_{n,mixer}^2$ is the power density of mixer's thermal noise, and k'_{mixer} is the mixer's flicker noise factor. Similarly, the noise power density of the gm-C integrator is modelled as

$$S_{n,gmC}(f) = v_{n,gmC}^2 + \frac{k'_{gmC}}{f} \tag{5.4}$$

The simulated RX noise sources are plotted in FIGURE 5.6. As discussed in Section IV B, the mixer is designed to have lower input referred noise than the GmC circuit to lower the overall noise figure of the RX. Also, the noise from the mixer and the GmC circuit dominates the KT noise $v_{n,s}$. Therefore, $v_{n,s}$ is neglected in the following analysis for simplicity. The total RX noise at the output is then given by

$$\begin{aligned} V_{n,RX}^2 = \int_{f_L}^{f_H} & S_{n,mixer} A_{V,mixer}^2 |H_{gmC}(f)|^2 \\ & + S_{n,gmC} |H_{gmC}(f)|^2 df \end{aligned} \tag{5.5}$$

Plugging Eqn. 5.3 and Eqn. 5.4 into Eqn. 5.5, we get

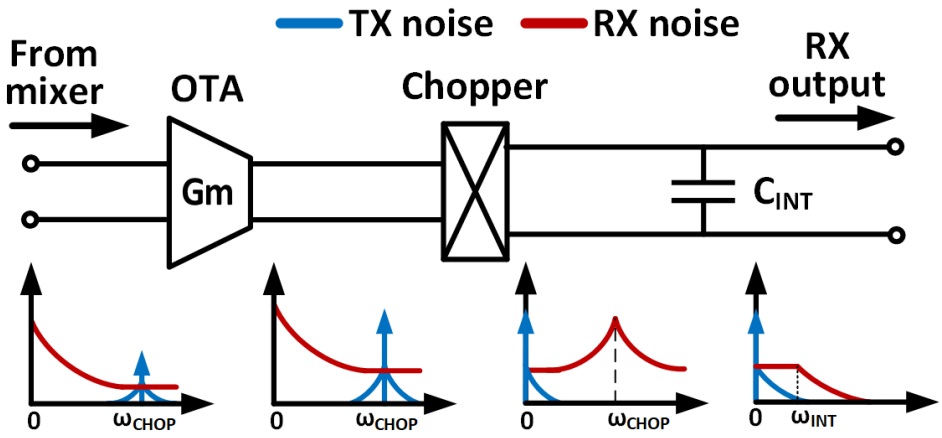

FIGURE 5.7. Signal and noise processing at the baseband circuits.

$$V_{n,RX}^2 = \int_{f_L}^{f_H} (v_{n,mixer}^2 + \frac{k'_{mixer}}{f}) A_{V,mixer}^2 |H_{gmC}(f)|^2 + (v_{n,gmC}^2 + \frac{k'_{gmC}}{f}) |H_{gmC}(f)|^2 df \tag{5.6}$$

With chopping, the flicker noise component at f_{chop} is down converted to DC. With the detailed derivation shown in Appendix A, the total RX noise can be approximated as

$$V_{n,RX}^2 \approx \int_{f_L}^{f_H} (v_{n,mixer}^2 + \frac{8k'_{mixer}}{\pi^2 f_{chop}}) A_{V,mixer}^2 |H_{gmC}(f)|^2 + (v_{n,gmC}^2 + \frac{8k'_{gmC}}{\pi^2 f_{chop}}) |H_{gmC}(f)|^2 df \tag{5.7}$$

FIGURE 5.8 shows the simulated total RX noise for different chopping rate f_{chop}, justifying the model of Eqn. 5.7. FIGURE 5.9 shows the simulated noise spectral densities of the various noise types shown at the output of the system. The chopping suppresses the RX noise that is generated between the choppers in the TX and the RX, and the CPNC suppress the TX noise under the RX noise. The circuit simulation results further validate the foregoing theoretical noise analysis in the following subsection of SNR analysis.

5.1.4. SNR and Resolution. The SNR of the system can be expressed as

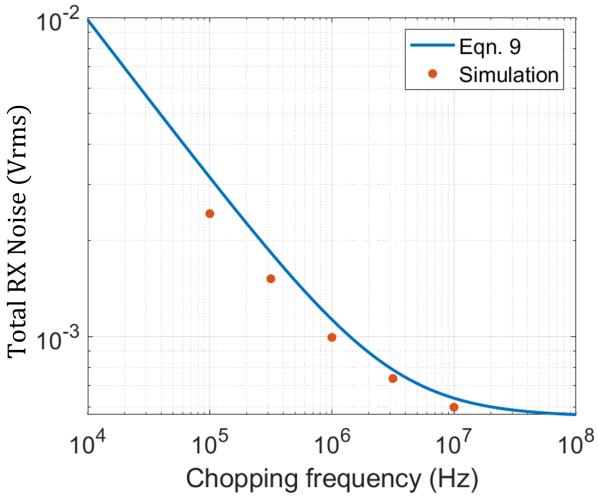

FIGURE 5.8. Total RX noise at the RX output for different chopping frequencies.

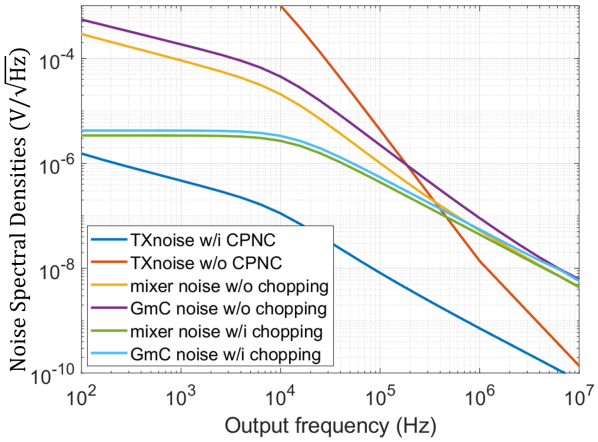

FIGURE 5.9. Noise spectral densities of different noise at the RX output.

$$SNR = \frac{V_{sig,out}^2}{V_{n,RX}^2 + V_{n,TX}^2} \tag{5.8}$$

By setting SNR = 1, the minimum detectable permittivity difference or the sensing resolution $\delta\epsilon_r$ can be expressed as Eqn. 5.9. The signal, noise and the resolution vs. the measurement integration time is shown in FIGURE 5.10 (a). The signal and therefore the TX noise increases by 20 dB/dec as the GmC integrator integrates for longer time. The increase of the signal and the noises saturates at around 10 us due to the finite output resistant of the OTA, as shown in FIGURE 5.21 (b). The combination of the higher gain but smaller noise bandwidth due to the longer integration time results in the slower increase rate of the RX noise of 10dB/dec before it

$$\delta\epsilon_r = \sqrt{\frac{\int_{f_L}^{f_H}(v_{n,mixer}^2 + \frac{8k'_{mixer}}{\pi^2 f_{chop}})A_{V,mixer}^2|H_{gmC}(f)|^2 + (v_{n,gmC}^2 + \frac{8k'_{gmC}}{\pi^2 f_{chop}})|H_{gmC}(f)|^2 df}{P_{TX}Z_0 Sen_{\epsilon_r}^2 A_{V,RX}^2 - \int_{f_L}^{f_H} P_{TX}L_{TX}(f)Z_0 Sen_{\epsilon}^2 A_{V,comb}^2 A_{V,mixer}^2 4|1-e^{-j2\pi f t_d}|^2|H_{gmC}(f)|^2 df}} \tag{5.9}$$

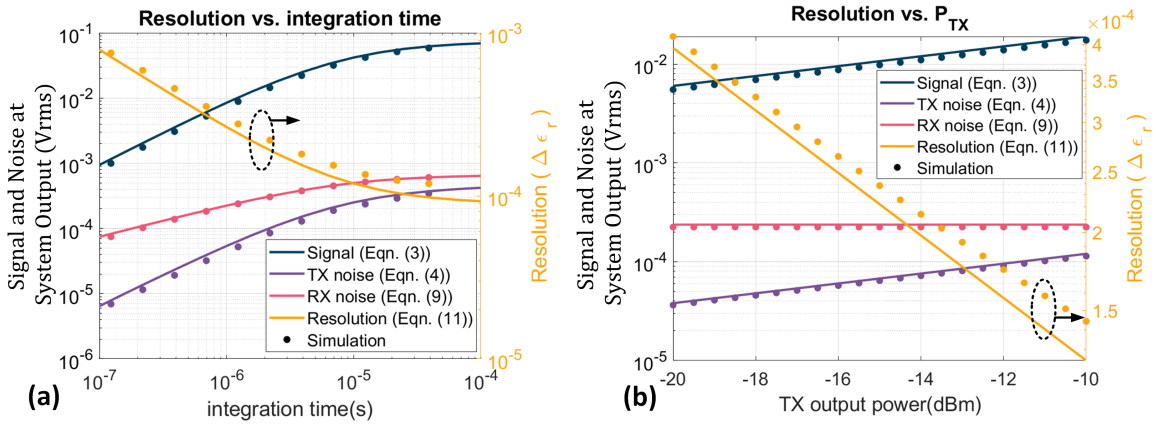

FIGURE 5.10. Theoretical and simulated signal, TX noise and RX noise voltage at the system output and resolution vs. (a) Integration time. (b) TX output power

saturates. Because the RX noise dominates over the TX noise, the signal increases 10 dB/dec faster than the total noise and therefore the resolution improves with the integration time with a -10 dB/dec slope before the integration saturates. The signal, noise and the resolution vs. the TX output power is shown in FIGURE 5.10 (b). With increased TX output power, signal and TX noise increases while the RX noise remains independent on TX output power, as expected. The SNR and therefore resolution improves because RX noise is dominating. The systematic analysis above guides the design decisions and the power spending strategies in the TX and RX design process, as shown in the next sections.

Given the expression of $H_{gmC}(f)$ derived from Appendix B, Eqn. B.14, the total RX noise can be approximated as

$$V_{n,RX}^2 \approx ENBW[(v_{n,mixer}^2 + \frac{8k'_{mixer}}{\pi^2 f_{chop}})A_{V,mixer}^2 A_{V,gmC}^2 + (v_{n,gmC}^2 + \frac{8k'_{gmC}}{\pi^2 f_{chop}})A_{V,gmC}^2] \tag{5.10}$$

where $ENBW \approx 1.57 f_{3dB}$ is the noise equivalent bandwidth of the RX. The noise factor of the RX can be expressed as

$$F = \frac{v_{n,RX,out}^2}{v_{n,S}^2 \cdot A_{V,RX}^2} = \frac{v_{n,RX,out}^2}{8kTZ_0 \cdot A_{V,RX}^2} \tag{5.11}$$

where $v_{n,RX,out}$ is the noise power density at the RX output due to the RX circuits and the source impedance. Because of the dominance of the RX noise over the noise due to the source impedance, it can be approximated as

$$\begin{aligned} v_{n,RX,out}^2 \approx (v_{n,mixer}^2 + \frac{8k'_{mixer}}{\pi^2 f_{chop}}) A_{V,mixer}^2 A_{V,gmC}^2 \\ + (v_{n,gmC}^2 + \frac{8k'_{gmC}}{\pi^2 f_{chop}}) A_{V,gmC}^2 \end{aligned} \tag{5.12}$$

Finally, combining Eqn. 5.10, Eqn. 5.11 and Eqn. 5.12, the total RX noise at the output can be expressed concisely in terms of the RX noise factor

$$V_{n,RX}^2 = ENBW \cdot F \cdot 8kTZ_0 \cdot A_{V,RX}^2 \tag{5.13}$$

which will in turn help result in a concise expression of the system sensing resolution with design insight in next subsection.

5.1.5. SNR and Resolution. With Eqn. 5.1, Eqn. 5.2 and Eqn. 5.7, the SNR of the system can be expressed as

$$SNR = \frac{V_{sig,out}^2}{V_{n,RX}^2 + V_{n,TX}^2} \tag{5.14}$$

Eqn. 5.9 is plotted with simulation results in FIGURE 5.10 with varying transmitter power and integration time(or $ENBW$). As shown in Fig 5, in the high resolution sensing regime, $V_{n,TX} << V_{n,RX}$. The system SNR has a concise form by neglecting the TX noise

$$SNR = \frac{P_{TX} Sen_{\epsilon_r}^2 \Delta\epsilon_r^2}{ENBW \cdot F \cdot 8kT} \tag{5.15}$$

Setting SNR = 1, the minimum detectable permittivity difference or the sensing resolution $\delta\epsilon_r$ can be expressed as

$$\delta\epsilon_r = \frac{\sqrt{ENBW \cdot F \cdot 8kT}}{\sqrt{P_{TX}} Sen_{\epsilon_r}} \tag{5.16}$$

Eqn. 5.16 shows that the high resolution can be achieved by having low RX noise figure and high permittivity sensitivity.

5.2. TX Design

The block diagram of the TX is shown in FIGURE 5.1, and the schematic and the core passive layout of the TX are shown in FIGURE 5.11. The TX generates sub-THz excitation for the sensors and provides injection LO to the RX to suppress the phase noise associated with the excitation signals in the sensing and reference paths. For this prototype, the TX should meet three requirements: the LO output power should be large enough to injection-lock the RX; based on FIGURE 5.10(b), the sensing and the reference path power should be large enough to achieve a permittivity sensing resolution to the order of 10^-4; the TX's output frequency should have a tuning range of 8 GHz to cover the resonant frequency shift caused by the common dielectric materials. From simulation, to injection-lock the RX ILO with a frequency range of 8 GHz, the minimum required input power at the RX's LO port is -15 dBm. Considering the 4dB insertion loss of the LO feedforward path from the sensor structure's simulation, the LO buffer needs an output power of -8 dBm to have some safe margin. Designed as a class-A power amplifier, the load line simulation of the LO buffer determines the device size of the pseudo-differential pair to be 6.7um, resulting in a DC power consumption of 9 mW for the LO buffer. A load pull simulation determines the optimum load impedance of the pseudo-differential pair for maximum output power is $Z_{opt} = 130 + j205\Omega$. A transformer-based balun T_{LO} converts $Z_0 = 50\Omega$ to Z_{opt} with a loss of 2 dB. The RF buffer delivers differential signals to the sensing and reference paths through the TX chopper. The buffer's device size has a direct impact on the output power level and therefore the system SNR. However, larger device also loads the VCO tank, resulting a small swing at the input of the buffer if the VCO devices are not widened correspondingly [**56**]. To limit the overall power consumption of the sensing system, the device is chosen to be 6.7 um wide, identical to the LO buffer, also to maintain layout symmetry. Therefore, the RF buffer has the same Z_{opt} as the LO buffer. Before designing the RF buffer's impedance matching transformer T_{RF}, the TX chopper is designed first so that its parasitics can be absorbed into the impedance matching. The device size of the chopper is chosen to be 12um to have the minimum power loss of 4.4 dB. This is also the

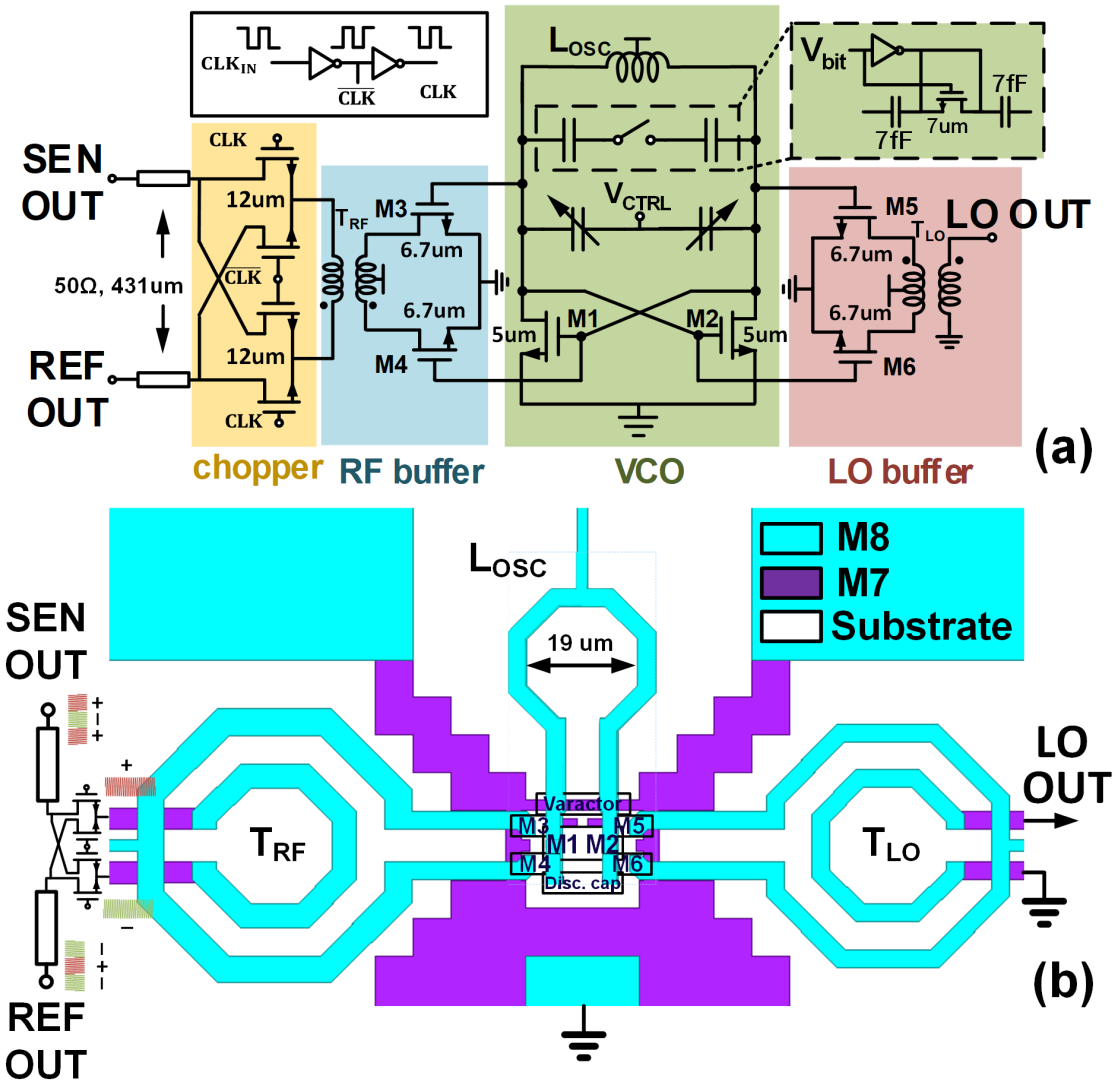

FIGURE 5.11. TX circuit. (a) TX schematic. (b) Core layout.

device size ensuing the best on-off ratio for each switch. The opposite-phase square-wave chopping signals are applied to the gates of the chopper switches to modulate the signals on the sensing and reference paths into BPSK signals. As can be seen on FIGURE 5.11, the signals with equal amplitude but opposite phase diverge at the output of the chopper to the sensing and reference path outputs, respectively, through the identical 431 um 50Ω CPW's, which have a loss of 1.5 dB. The transformer of the signal buffer is then designed to match the input impedance of the chopper to Z_{opt}.

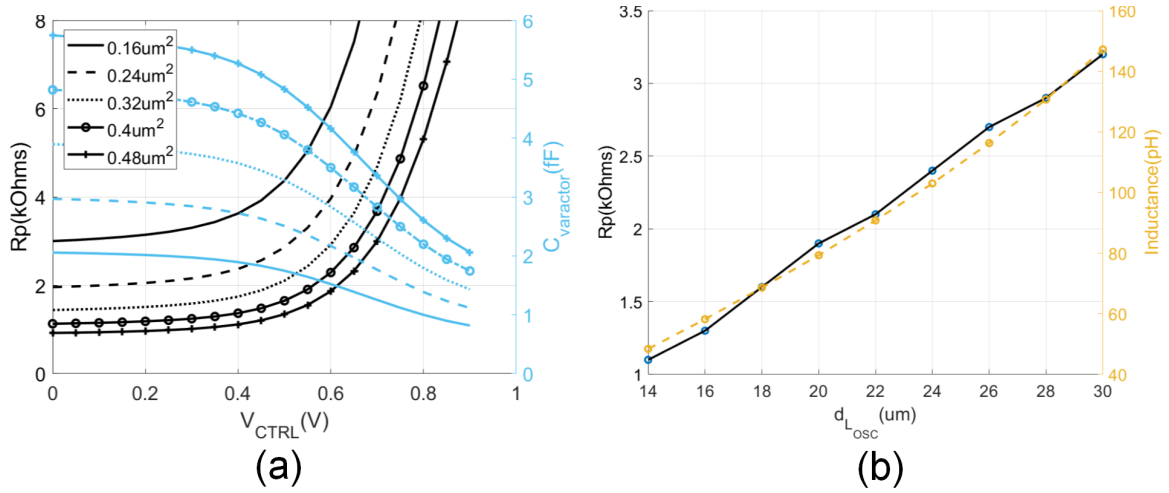

FIGURE 5.12. VCO design considerations. (a) Effective parallel resistance and capacitance of the varactors with different sizes. (b) Effective parallel resistance and inductance of the VCO inductor with different diameters

For the generation of sub-THz signal in CMOS technology, harmonic oscillator or fundamental oscillator with multiplier are the common methods, due to the fact that the operation frequency is close to f_{max} of the device [**57**] [**58**]. By contrast, fundamental oscillator is more efficient, without the need of the extraction of the weaker harmonics, yet it is also more challenging to design due to the higher loss of the passives and lower activity of the CMOS device at this frequency. In this work, to minimize the power consumption, a fundamental VCO is adopted to generate the 160 GHz signal for the sensing system. To achieve a tuning range of 8 GHz, a combination of the MOS varactors pair and a single-bit discrete capacitor are used. The VCO device size is determined to be 5 um to achieve an LO output power of -8 dBm, as shown in FIGURE 5.13, with the loading of the varactors and the discrete cap. The cross-coupled devices contributes 8 fF parasitic capacitance to the VCO's resonant tank, and consumes 8 mW of DC power. At 160 GHz, the quality factor of the varactor is significantly lower than those in the GHz range. To achieve an 8 GHz tuning range, a varactor size of $0.32um^2$ is chosen, whose quality factor varies from 28 to 5.5. To minimize the ground loss of the core area layout, the top two layers of thick metal M8 and M7 are used as ground in the core area, as shown in FIGURE 5.11(b). By the careful design and layout, the VCO generate a differential voltage amplitude $> 800mV$ at its drain nodes, which directly drives the gates of the LO and RF buffer devices.

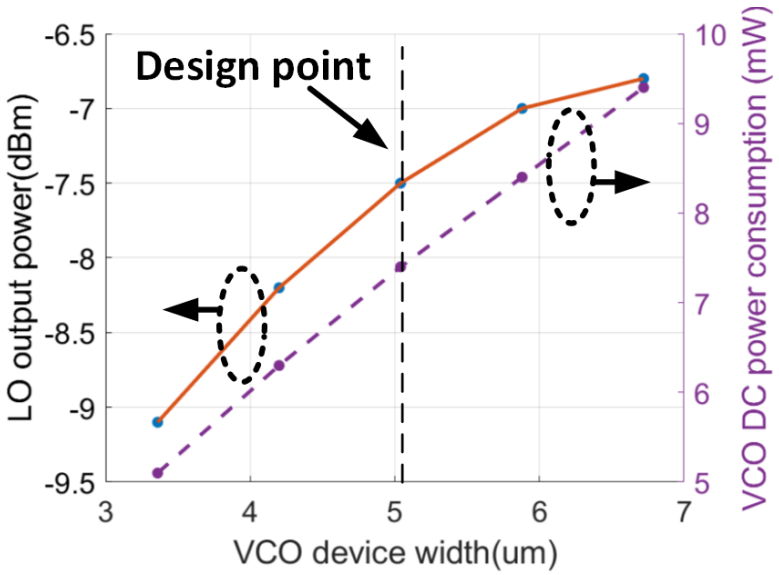

FIGURE 5.13. VCO device sizing and LO output power and DC power consumption.

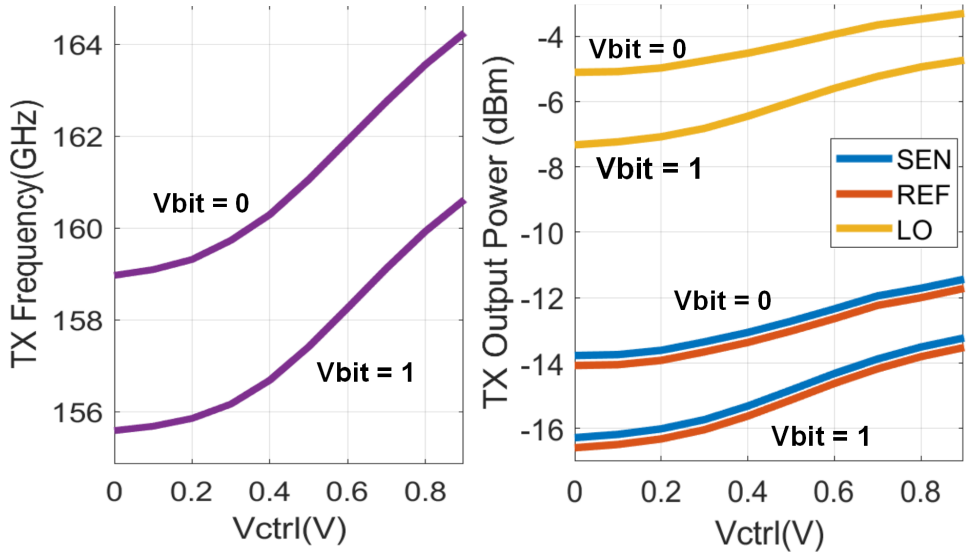

FIGURE 5.14. TX frequency tuning range and output power.

The simulated performance of the TX is shown in FIGURE 5.14. The LO buffer delivers the output power of -8 dBm to -3 dBm to the LO output port within the TX frequency tuning range. And the output power of the sensing and reference paths are from -11.5 dBm to -16.5dBm within the TX frequency sweep range. The output power of the sensing and reference port is lower than the LO port because the signal buffer drives two 50Ω paths at the same time, on top of the

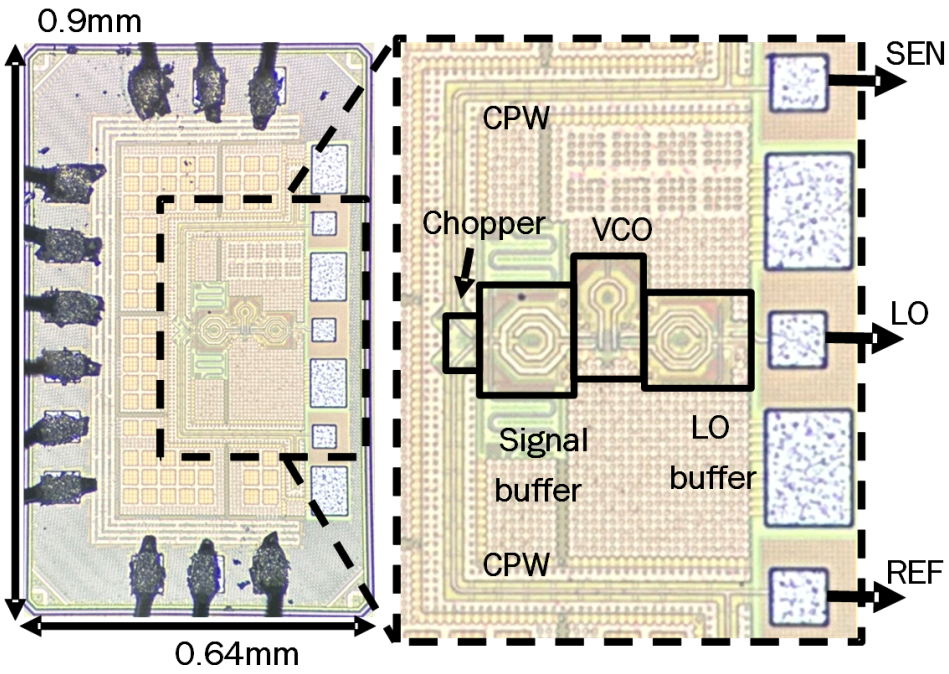

FIGURE 5.15. TX chip photo.

additional loss of the chopper and the routing CPW's. The output power difference of the sensing and reference paths are due to the layout mismatch of the TX. This mismatch, along with the sensor's fabrication mismatch, can be calibrated out in the measurement process. The simulated phase noise of the TX is shown in FIGURE 5.4. The TX chip is fabricated in 28 nm bulk CMOS technology and the chip photo is shown in FIGURE 5.15.

5.3. RX Design

The combiner's schematic and simulated performance is shown in FIGURE 5.17 and its layout can be seen from the RX chip photo in FIGURE 5.22. It is made of five sections of CPW and it combines the signal from the sensing and referencing paths. The combined signal is then split and delivered to the input of the mixers of the I and Q paths. The loss of the combiner is 5.2 dB.

At sub-THz, the power efficiency of the low-noise amplifier in terms of its effectiveness of lowering the NF of the entire RX is much lower than the GHz counterparts. Therefore, the RX adopted mixer-first topology. The design goal for the mixer is to have a reasonable noise figure and gain within a limited power budget to dictates a optimum noise performance of the overall RX.

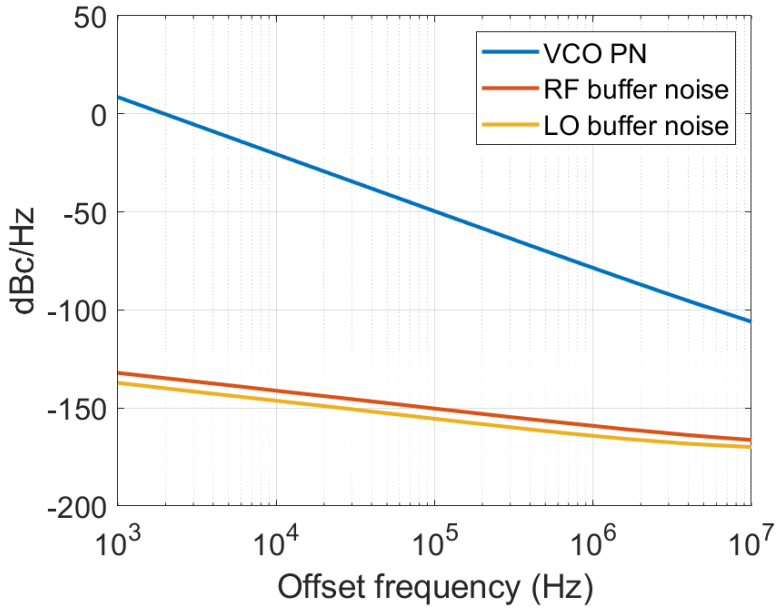

FIGURE 5.16. TX output noise partition.

The mixer's schematic is shown in FIGURE 5.18. A single-ended Gilbert cell serves as a natural balun to avoid the loss of the passive balun at sub-THz frequencies. The gm device is chosen to be 20 um-wide to have a transconductance of 22 mS. 3.3 mA out of 3.5 mA DC current from the gm device is bled to a PMOS current helper to relieve the current steering load of the switching devices. Less steering current allow the switching device to spend less time in transition, resulting in a better gain and noise performance. Less DC current also allows using larger load resistance and helps reduced the flicker noise of the switch devices, which further boost the gain and noise performance of the mixer.

The parasitic capacitance at node X steals away signal current from the gm device and increases the switching devices noise contribution to the output by lowering the impedance at the node. The inductor L2 of 45 pH and Q = 9 in the current bleeding path is used to resonate out the parasitic capacitance. The voltage gain of the mixer is around 17 dB and the noise figure is about 15.4dB. The switch devices contribute the most of the noise due to the relative low impedance at node X and the moderate differential LO voltage amplitude about 400 mV at 160 GHz. The ILO's schematic is shown in FIGURE 5.18. The ILO needs to have 8 GHz lock range to cover the measurement range and high output voltage swing at the mixer's LO port to maximize the mixer gain. To provide

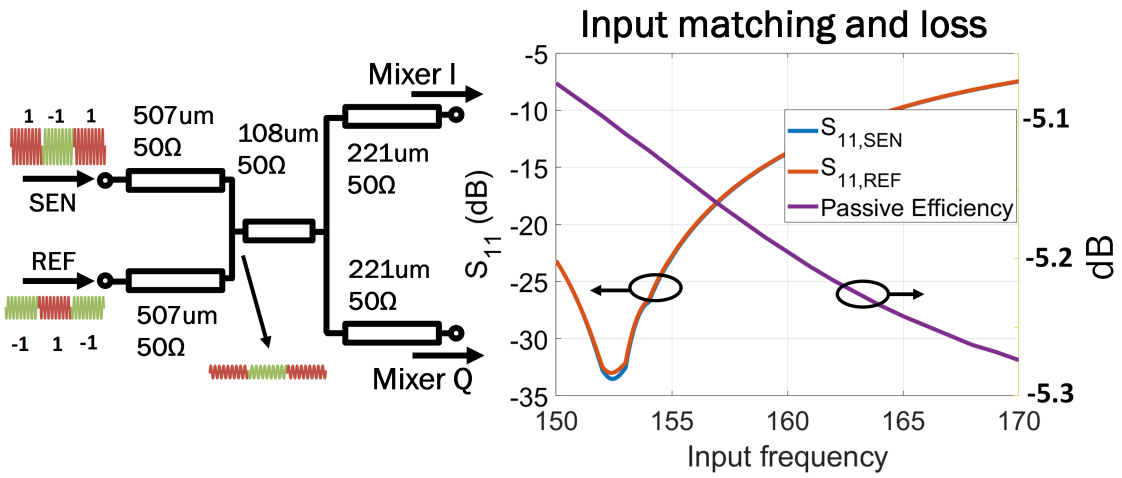

FIGURE 5.17. Combiner schematic and simulated performance.

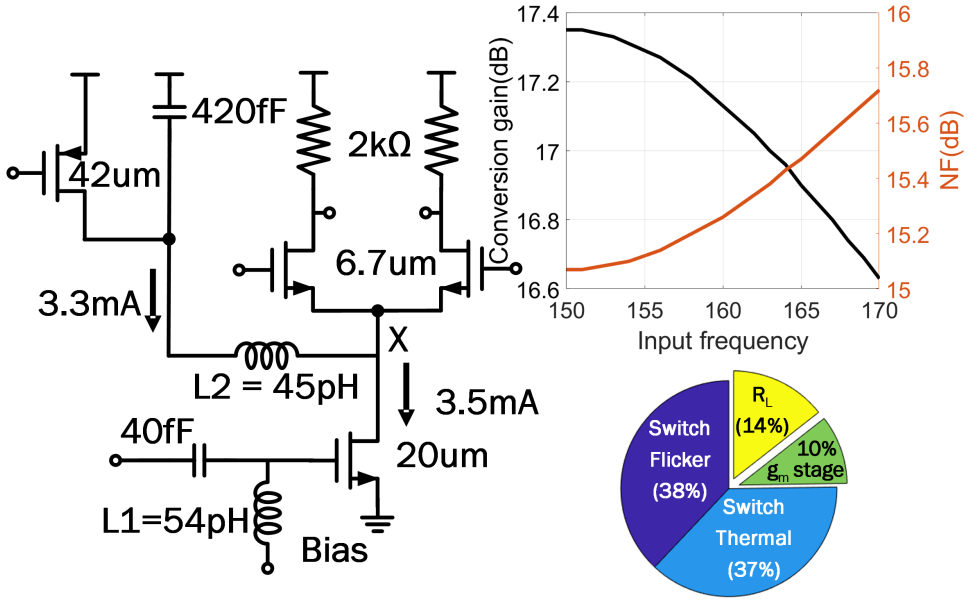

FIGURE 5.18. Mixer schematic, performance and noise contribution.

quadrature LO for the mixers of the I/Q path, the design of an RC poly-phase filter feeding two standalone ILO is adopted to avoid using the lossy quadrature coupler for quadrature oscillation generation that is commonly used in low frequency QILO's [**59**]. The resulting phase mismatch of the I/Q paths can be calibrated out in the measurement as a static process. An input balun converts the incoming TX LO signal to differential signal that drives the RC poly-phase filter to generate the two pairs of quadrature signals. From simulation, to have a 15 dB conversion gain, the

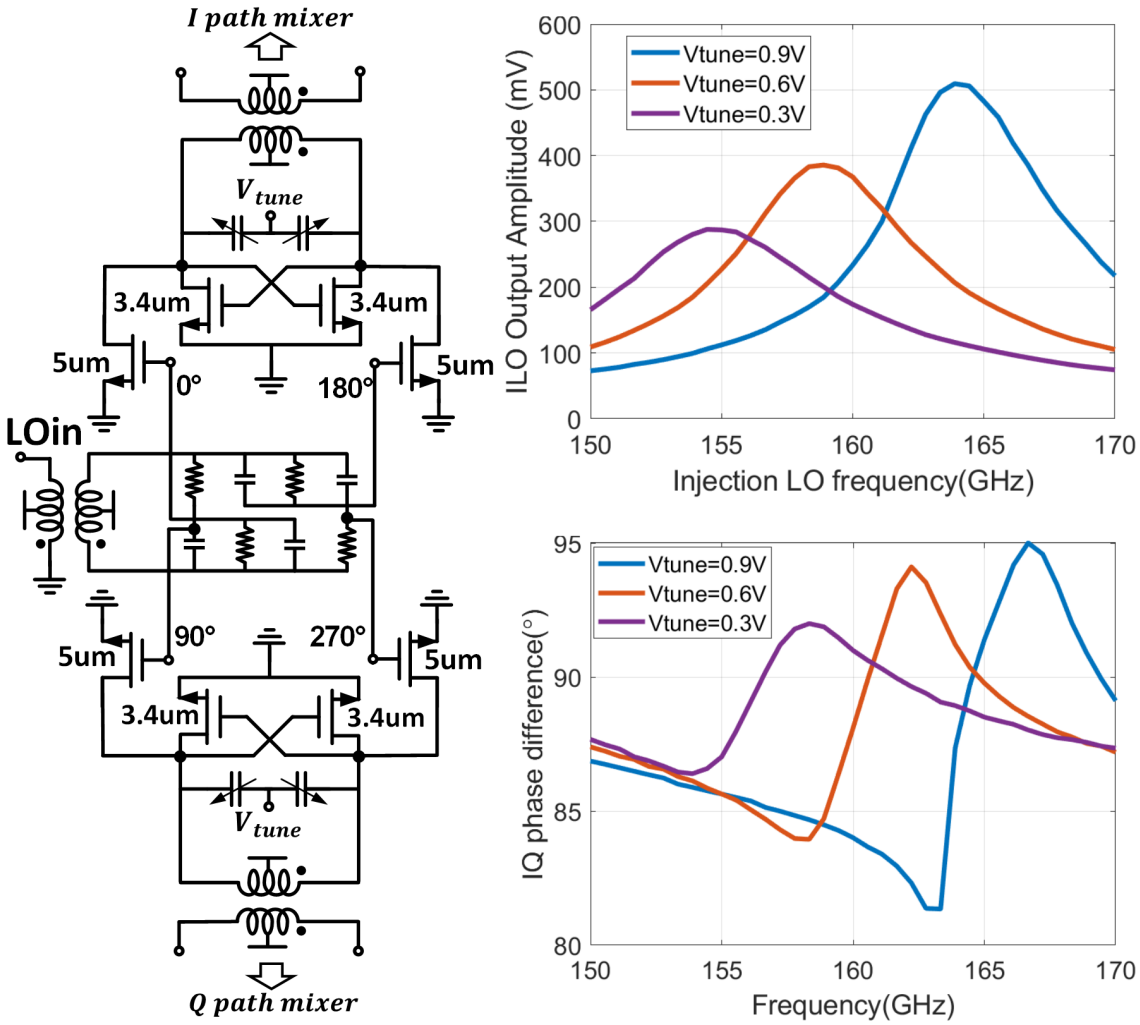

FIGURE 5.19. ILO schematic, output amplitude and I/Q phase difference.

mixer requires a 400 mV amplitude differential voltage at the gate of its LO devices. To achieve a reasonable lock range with this output amplitude requirement, two methods are adopted. First, the injection devices are larger than the oscillator device to have a strong enough injection to achieve a larger lock range. A pair of varactors are used to further increase the overall lock range by tuning the self-oscillation frequency of the core oscillator. From simulation, with a -12dBm injection power delivered at the RX's LO port, the lock range with larger than 400 mW LO amplitude is 12 GHz to have a safe margin for process variation, as shown in FIGURE 5.19.

The Gm-C integrator is implemented with a folded telescopic OTA as the Gm stage and a 52 pF on-chip integration capacitor. The OTA is designed to have low input-referred noise and high

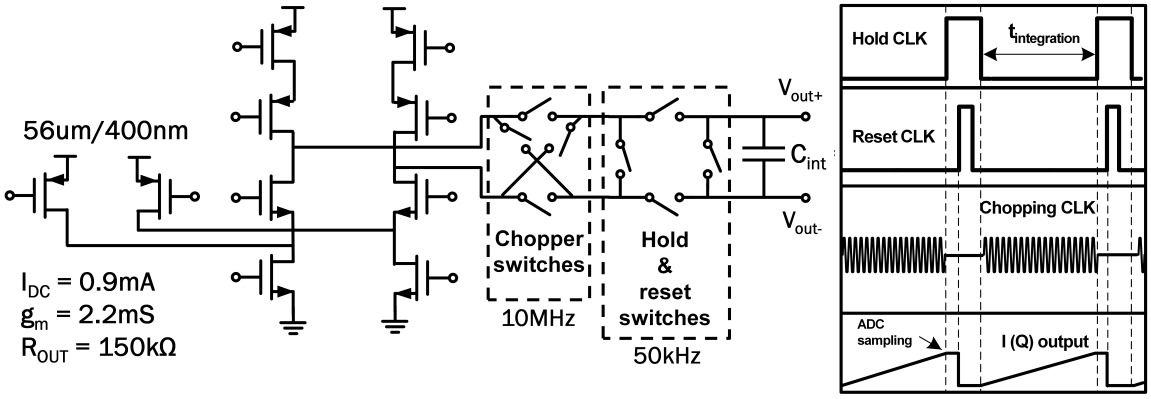

FIGURE 5.20. GmC schematic and analog signal processing timing.

output resistance to achieve a high SNR. A chopper is inserted between the OTA and the capacitor to suppress the flicker noise of the OTA and the mixer. The hold and reset switches control the integration period. Comparing to [**54**], the separation of the chopping and hold switch allows a longer integration time than the chopping period, resulting a higher SNR. The DC offset and low frequency noise are removed by the multiple chopping periods within one integration cycle. With the detailed derivation shown in the Appendix B, the transfer function of the GmC integrator with the integration time of $t = t_{int}$ is expressed as

$$H_{gmC}(s) = \frac{GmR_{out}(1 - e^{-st_{int}})}{1 - e^{-st_{int}} + R_{out}sC_{int}} \tag{5.17}$$

which is plotted in FIGURE 5.21(b) for different $t = t_{int}$. A longer integration time results in a larger DC gain and smaller ENBW, and hence higher SNR. As can be seen, however, comparing with an ideal Gm-C integrator in FIGURE 5.21(a), the increase of the gain and decrease of the bandwidth start to saturate as t_{int} increases above 10us. This saturation behavior is also manifested in the saturation of the resolution improvement with longer integration time in FIGURE 5.10.

This deviation from the ideal GmC's behavior is caused by the finite output resistance $R_{out} = 150k\Omega$ of the OTA, and the maximum integration time is constrained by the output resistance of the OTA. With $R_{out} = 150k\Omega$, the maximum integration time is around 14 us, which results in a DC gain of 50 dB and a ENBW of 20 kHz.

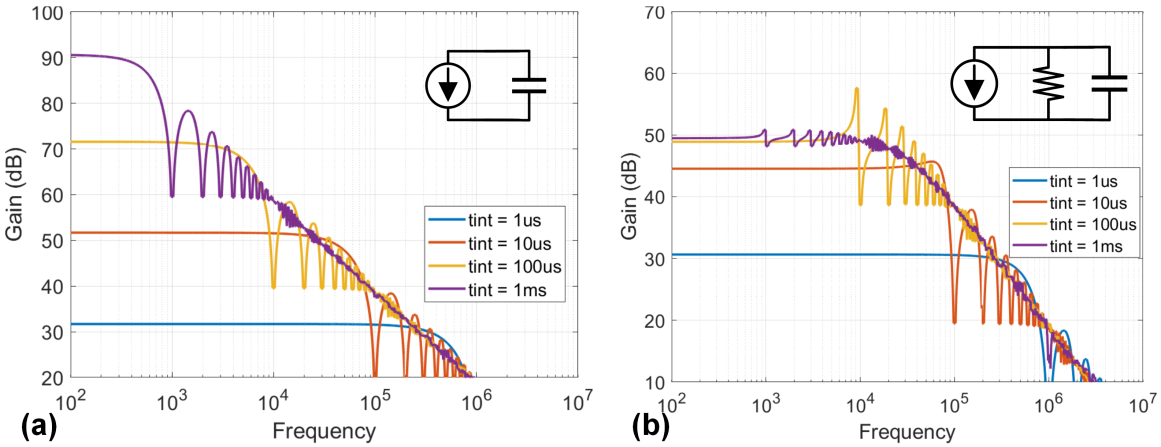

FIGURE 5.21. Transfer functions of (a)ideal GmC integrator and (b) practical GmC integrator with finite output resistance.

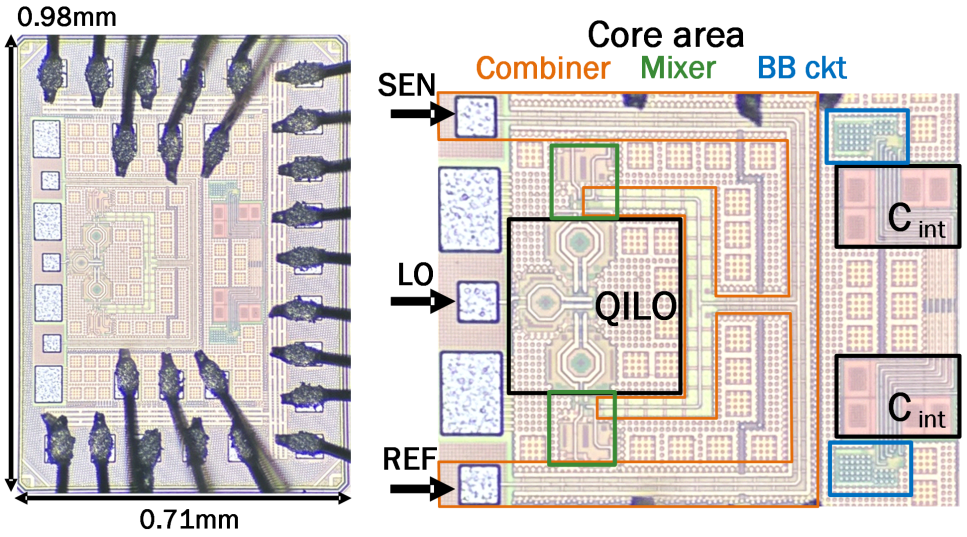

FIGURE 5.22. Photo of the RX chip and zoomed-in core area.

5.4. Packaging and Peripheral Circuits Design for Low Noise Sensing Systems

5.4.1. TX, RX and Sensor Structure Packaging. The TX chip, the RX chip and the sensor structures are glued on a PCB board and interconnected with bonding wires. The bonding wires interconnect the GSG pads of the on-chip CPW's of the sensing path, the reference path and the LO path with those on the sensor structure. These signal bonding wires are as short possible to minimize their impact on the loss of the 160 GHz signal, as compared to the DC wires, as shown in

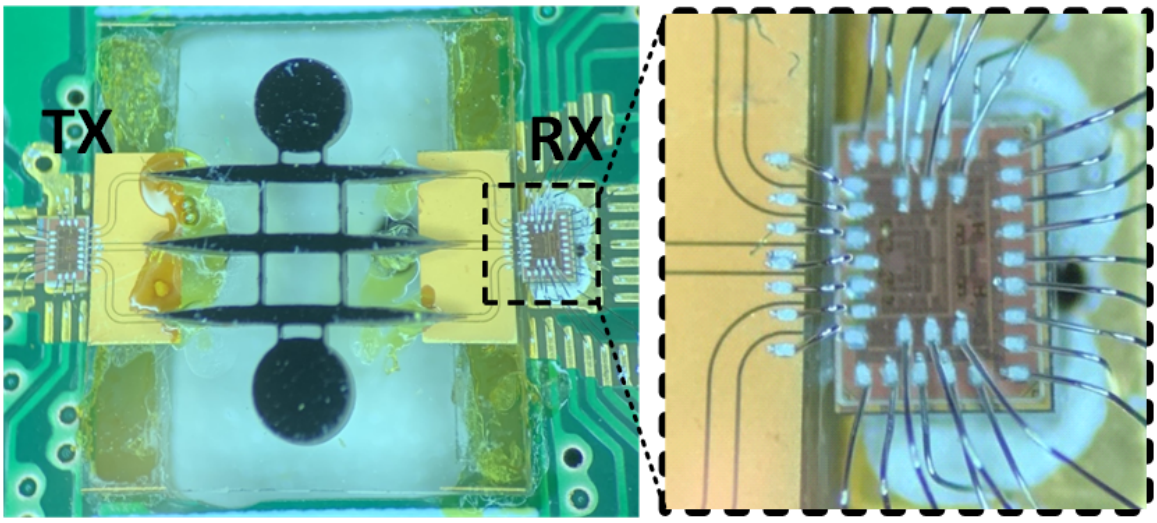

FIGURE 5.23. TX chip, sensor structure, RX chip are mounted on the PCB and interconnected with bonding wires.

the zoomed-in photo of FIGURE 5.23. The signal bonding wires are approximately 60 um, whose inductance's are around 60 pH based on EM simulation in HFSS, which are incorporated in the design of the output matching network of the TX and the input matching network of the RX to ensure good matching at these interfaces. The wire bond service is provided by the CHFE facility in UCLA. The area under the sensor disk of the PCB is cut in the PCB fabrication process to prevent Q of the resonator sensor from being lowered by the loss of the FR4 material of the PCB substrate.

The TX and RX chips are carefully designed to have low noise at the system output by suppressing the noise generated by the circuits on-chip. As a result, the system output is more susceptible to various kinds of off-chip noise. The PCB of the sensing system is therefore carefully designed to protect the sensing system from being polluted by the noise from the noise off-chip environment. The most dominant two types of noise sources are the noise from the voltage source equipment and the electromagnetic interference (EMI). The following two subsections illustrate the correspondent analysis and suppression techniques.

5.4.2. Measurement and Suppression of EMI Noise. The EMI may come from wireless communication signals such as cellular and WiFi as well as the emissions from the nearby electronics

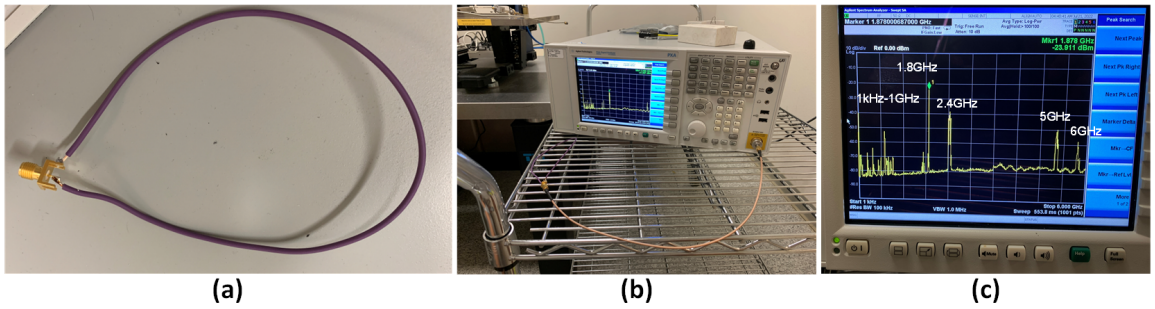

FIGURE 5.24. Lab EMI measurement (a) Loop antenna. (b) Measurement of the EMI signals picked-up by the loop antenna using a spectrum analyzer. (c) the EMI signals picked-up by the loop antenna.

and equipment. The EMI environment in the lab is tested using a simple loop antenna and a spectrum analyzer. As shown in FIGURE 5.24(c), a simple loop antenna can pick up upto -20dBm of noise from the radiation in the environment. A wire loop of a diameter of 10 cm is used in the test as a loop antenna because loops are easily formed by the wires and PCB traces, which could potentially receive EMI radiation from the measurement environment.

To minimize the pollution of the signals from the environment EMI, three measures are taken. First, sufficient amount of bypass capacitors are used for each DC voltage nets and power supplies to filter out the EM noise picked up by the traces. Second, to prevent the low noise output signal from being polluted by the EMI noise, the outputs of the RX is interfaced by SMA connectors. Hence, the ground shield of the coaxial cables that connects the RX output with the measurement equipment such as data acquisition unit can shield the signal from the external EMI. Third, the PCB is carefully designed to minimize the possible loops formed by the traces and the jump wires, because a small loop antenna's radiation resistance R_{rad} and therefore its radiation efficiency is proportional to the square of its area A, as

$$R_{rad} \approx 31.2k\Omega(\frac{N \cdot A}{\lambda^2})^2 \tag{5.18}$$

, where N is the turn numbers of the loop wire and λ is the operating wavelength. Therefore, lowering the loop area lowers its efficiency as an antenna to pick up EMI from the air. Furthermore, a loop formed by conductors not only picks up EMI from the air as a loop antenna, but also has a high inductance and therefore a high impedance to magnify any unwanted transient currents, no

matter from the EMI or from the IC internally, into larger voltage swings.

5.4.3. Analysis and Suppression of DC Supply Noise. The other major source of off-chip noise is the noise from the DC voltage supply equipment. General purpose voltage supply equipment typically does not focus to have low noise feature at their voltage output. For example, the Keithley 2600B System SourceMeter has a thermal noise of 20 mVpp at its voltage output in the frequency range of 10 Hz - 20 MHz. This translates to $670nV/\sqrt{Hz}$. On top of thermal noise, its datasheet also specifies flicker noise of $\sim$ 50 uVpp in the frequency range of 0.1Hz - 10Hz. Despite the fact that the flicker noise has higher noise power spectral density at the lower frequencies, the smaller frequency range or namely the bandwidth in which the flicker noise is dominant over thermal noise makes the flicker noise's contribution to the total noise power a minor factor comparing to the white thermal noise, which has the constant power spectral density in a wide bandwidth. Hence, the following analysis and simulations focus on the white thermal noise contributions from the various sources.

To understand how this noise level would impact the sensing system performance, extensive investigation is conducted to study the noise transfer functions from every DC pad of the chips to the final system output. The following paragraphs elaborate the most critical and typical nodes as examples.

The most critical node that is particularly susceptible to DC supply noise is the frequency control voltage V_{cont} of the TX's VCO. Its voltage value directly translates to the oscillation frequency of the VCO, and in the same way, its noise directly contributes to the frequency or phase noise of the VCO. From the analysis of section 5.1, the TX phase noise can limit the systems sensing resolution if it is not suppressed to a sufficiently low level by careful measures. Despite the fact that the TX phase noise cancellation technique is applied in the sensing system design, the noise suppression capability of the technique is finite and the TX phase noise should be well controlled so that the phase noise contributed from off-chip should be minimized. Hence, it is common to use a ultra low noise DC voltage supply to control the frequency tuning voltage in the VCO measurement, as well as a low noise power supply for the VCO, to prevent the oscillator under test from being polluted by the noisy control voltage and power supply. FIGURE 5.23 shows an example of an

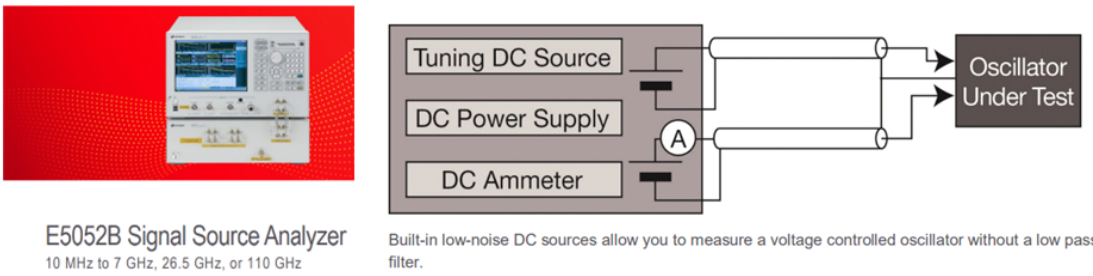

FIGURE 5.25. Example off-the-shelf VCO measurement equipment, which internally provides a ultra low noise ($1nV/\sqrt{Hz}$) DC source for the VCO's tuning voltage and supply voltage.

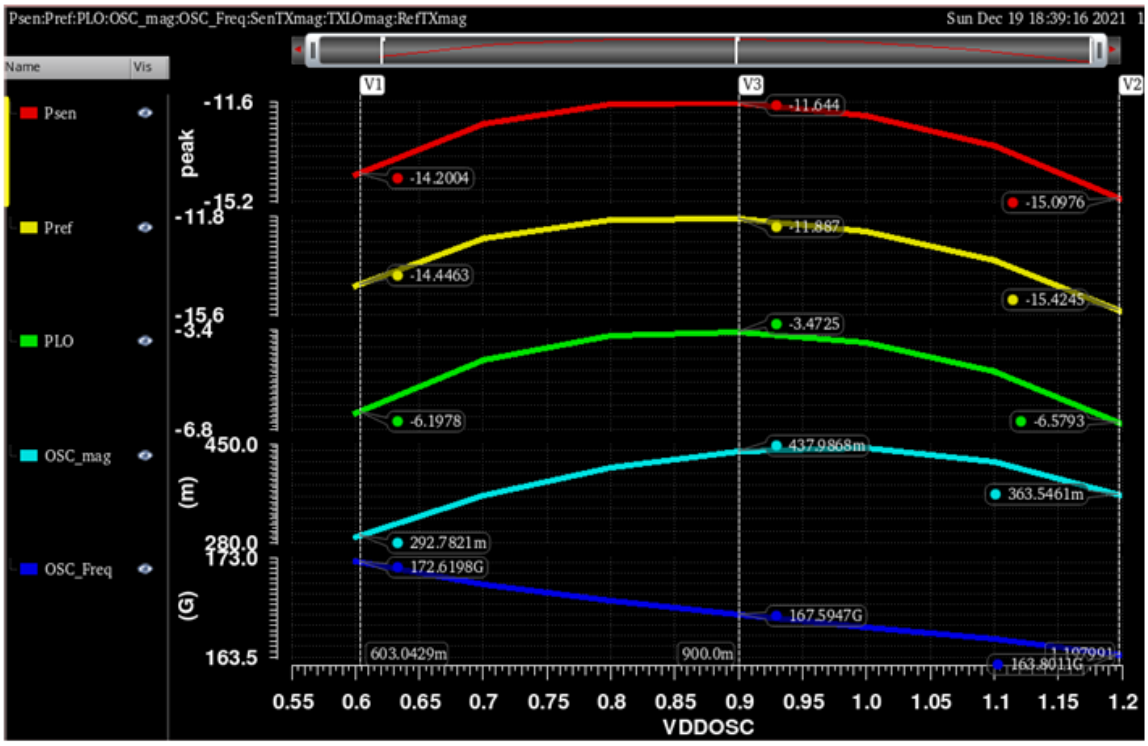

FIGURE 5.26. TX performance change with supply voltage VDD.

off-the-shelf VCO measurement equipment that provides low noise ($1nV/\sqrt{Hz}$) DC source for the tuning voltage and power supply of the oscillator under test. It is more obvious that the noise in the frequency tuning voltage would contribute directly to the phase noise of the VCO. Therefore, the following analysis focuses on how the noise in the power supply voltage can contribute to the phase noise of the VCO.

As shown in FIGURE 5.11, the VCO in the TX adopts the topology of cross-coupled pair with LC

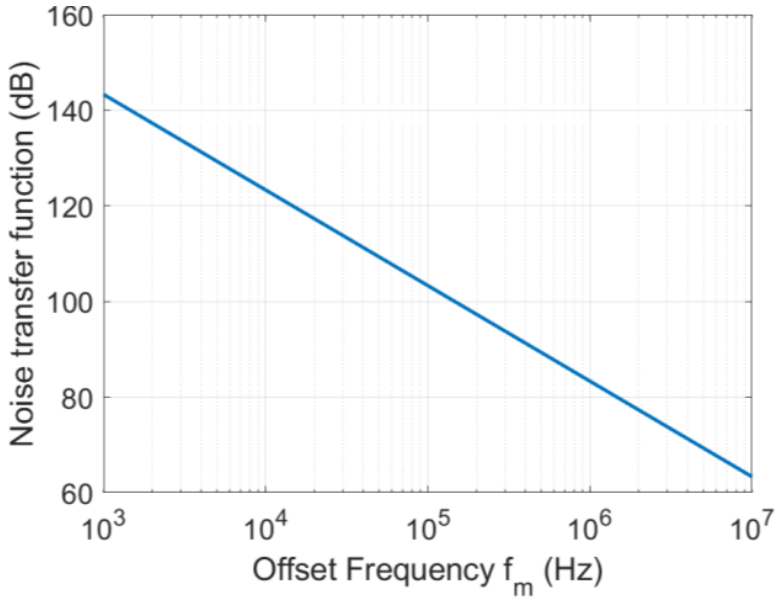

FIGURE 5.27. noise power spectral density transfer function $H_{VDD}(f_m)$ from VDD to VCO output.

resonance tank. The supply voltage applied at the center tap of the oscillator inductor also controls the gate and drain voltages of the cross-coupled pair transistors M1 and M2. On the other hand, the major parasitic capacitance of M1 and M2, C_{GS}, C_{DB}, are voltage dependent. Therefore, the change of the supply voltage changes the capacitance values of C_{GS}, C_{DB}. From the schematic of the VCO, C_{GS} and C_{DB} constitute part of the resonant tank capacitance. Thus, the supply voltage VDD changes the resonant frequency of the VCO indirectly, playing a similar role as the dedicated frequency control voltage V_{CTRL}. The frequency tuning property of the supply voltage can be utilized as a intended frequency tuning method, as in [**60**], where the MOS varactor's Q drops below 5 at frequencies above 300GHz. The frequency tuning capability of the supply voltage is simulated and shown in FIGURE 5.26. The TX performance changes when VDD changes from 0.6 V to 1.2 V. Together with change of the output power of the sensing, the reference and the LO path, the TX frequency changes from 163.8 GHz to 172.6 GHz. Similar to the frequency tuning gain of the VCO K_{VCO}, we define a supply voltage gain as $K_{VDD} \stackrel{\text{def}}{=} \Delta\omega_m/\Delta VDD$. Based on the simulation results shown in FIGURE 5.26, $K_{VDD} = 14.67Grad/Hz/V$. The following theoretical analysis is used to predict the transfer function of the supply noise to phase noise.

The supply voltage noise at certain frequency ω_m is model as $v_n cos(\omega_m)$, a sine wave with an

amplitude of v_n. Then the radian frequency drift caused by this noise can be expressed as

$$\Delta\omega(t) = K_{VDD} v_n cos(\omega_m t) \tag{5.19}$$

The output of the VCO can be expressed as, $Acos(\omega_0 t + \phi(t))$, where A is the amplitude of the VCO's output voltage swing, ω_0 is the nominal oscillation frequency, and $\phi(t)$ is the phase fluctuation. The resulting phase fluctuation due to this frequency drift is then expressed as

$$\phi(t) = \int \Delta\omega(t)dt = \frac{K_{VDD}}{\omega_m} v_n sin(\omega_m t) \tag{5.20}$$

by integrating the frequency drift over time. Therefore, the power spectral density of the phase fluctuation and the supply voltage noise has the following relationship

$$S_\phi(f_m) = (\frac{K_{VDD}}{\omega_m})^2 S_{vn}(f_m) = H^2_{VDD}(f_m) S_{vn}(f_m) \tag{5.21}$$

where

$$H_{VDD}(f_m) = (\frac{K_{VDD}}{\omega_m})^2 \tag{5.22}$$

is the noise power spectral density transfer function, from VDD to the VCO output. The plot of Eqn. 5.22 is shown in FIGURE 5.27. The transfer function shows a low pass feature with a roll-off rate of -20 dB/dec. This trend matches with the mechanism through which the white noise in a resonant tank is up-converted to the VCO phase noise with the slope of -20 dB/dec, predicted by the Leeson's phase noise model [**61**].

To further verify the theoretical prediction of Eqn. 5.22, a dedicated simulation of the TX VCO's phase noise and its transfer function is conducted, as shown in FIGURE 5.28. The TX isolated VCO is injected with white voltage noise of $S^2_{vn,VDD} = 1pV^2/Hz$ at the VDD node. And $H_{VDD}(f_m)$ is plotted in FIGURE 5.28(c) by $H_{VDD}(f_m) = S_\phi(f_m)/v^2_{n,VDD}$, where S_ϕ is the phase noise power spectral density in the unit of V^2/Hz of the VCO output which match with FIGURE 5.27 in both trend and quantity. FIGURE 5.28(d) shows the the VCO's output phase noise with the white supply noise of $1uV/\sqrt{(}Hz)$ being turned on(green) and off(red). When the supply noise is turned on, the phase noise is raised up by significant amount, of 55dB at 10MHz offset, for example. It can also be noted that, the -30 dB/dec slope of the intrinsic phase noise of the VCO (red curve)

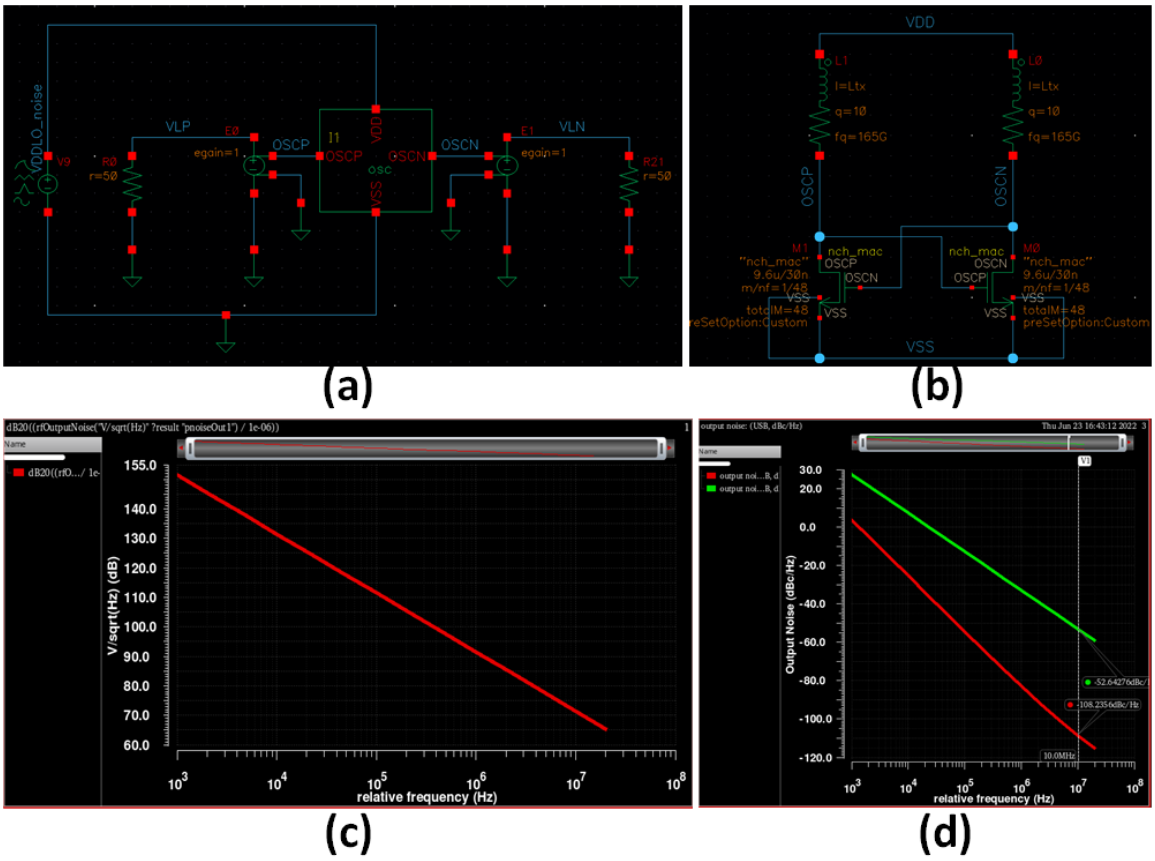

FIGURE 5.28. Circuit Simulation of $H_{VDD}(f_m)$. (a) Simulation test bench. (b) VCO schematic. (c) Simulated $H_{VDD}(f_m)$. (d) The comparison of the VCO's output phase noise with supply noise of $1uV/\sqrt{(}Hz)$ ON(green) and OFF(red).

due to the flicker noise up-conversion is replaced by the -20 dB/dec slope (green curve) when the white supply noise is turned on, which shows a domination of output phase noise due to the white noise up-conversion. The noise spectral density of $1uV/\sqrt{(}Hz)$ is used in the simulation based on the output noise specification of the DC supply source of the lab. Hence, the simulation shows that if the DC supply source is used directly for VDD, the output phase noise of the VCO would be dominated by the supply noise from the DC source. Further analysis shows that this is the primary mechanism of the supply noise impact on the TX output noise, as the VCO's phase noise is the dominant source of the TX output noise, as shown in FIGURE 5.16. Adding bypass capacitors at the supply nodes would not be particularly effective due to the low pass feature of the supply noise up-conversion transfer function $H_{VDD}(f_m)$,similar to the transfer function of a bypass capacitor.

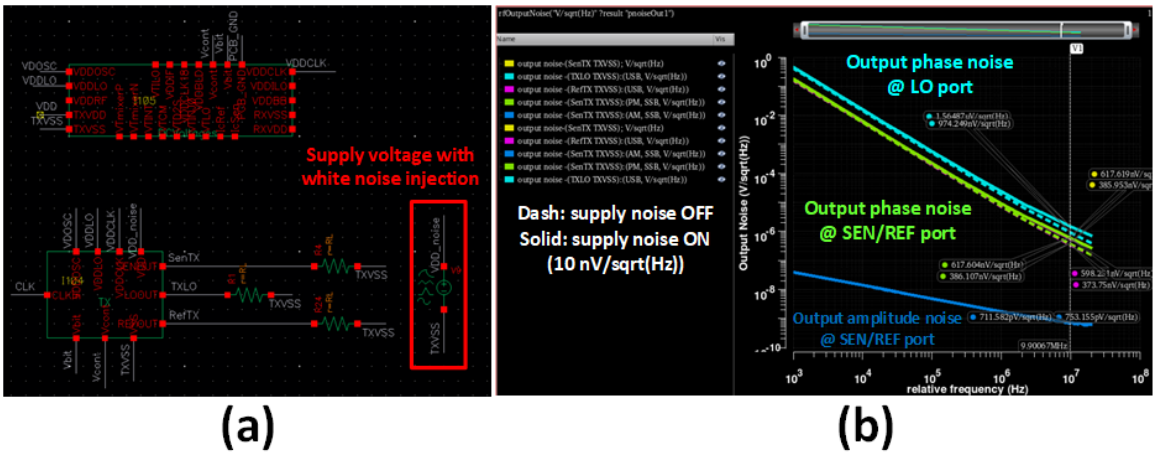

FIGURE 5.29. TX supply noise level requirement simulation. (a) Simulation test bench, with variable white noise source injection noise to VDD. (b) TX output phase noise for $10nV/\sqrt{(}Hz)$ supply noise injection.

Another options would be using low noise voltage regulators. The negative feedback and the band-gap reference in the low noise voltage regulators help suppress the noise level of the supply voltage from the DC source.

To determine the noise level requirement for the supply voltage which contributes negligible noise to the TX output, a simulation of the entire TX with a variable white noise source injected in the supply voltage is executed, as shown in FIGURE 5.29(a). The simulation results in FIGURE 5.29(b) shows the output noise spectral density in unit of $V/\sqrt{Hz}$ of the TX at the LO port and the sensing and the reference ports with the injection being turned on or off. When the injected white noise level is $10nV/\sqrt{(}Hz)$, the added TX output noise when the noise injection is on (solid line) is negligible comparing to the case when the noise injection is off (dash line). It is thus determined that the supply noise level has to be lower than $10nV/\sqrt{(}Hz)$. The same analysis and simulation is conducted for the RX power supply nodes and the corresponding noise transfer functions are lower than the TX's. Therefore with the simulated TX supply noise requirement, LT3045, a low noise low drop-out voltage regulator (LDO), is selected to be used as the voltage regulator for both TX's and RX's power supply, as its datasheet specifies a $2nV/\sqrt{(}Hz)$ voltage noise at its output. With the same methodology, the noise transfer function from all other DC access points of the sensing system are analyzed and simulated. The DC node with the highest noise gain to the final system

output is determined to be the frequency tuning voltage V_{CTRL} of the TX VCO. Similarly, with a $10nV/\sqrt{(Hz)}$ voltage noise injected to V_{CTRL}, the added output noise is negligible. With this requirement being taken into consideration, AD5676, a programmable low noise digital to analog converter (DAC) is adopted to generate the DC voltage, which has an output noise spectral density of $80nV/\sqrt{(Hz)}$. To further suppress its output noise, an RC filter is added between the output of the DAC and the V_{CTRL} pin of the chip. The series resistor of 2 kOhms and shunt capacitor of 1 uF set the noise suppression corner frequency at 8 Hz, which means the noise spectral density at V_{CTRL} pin is suppressed below $8nV/\sqrt{(Hz)}$ at the frequency of 80 Hz and above. The DAC has 8 channel and a total of two DAC's are used to provide 12 tunable DC voltages for both the TX and the RX chip. The programmable DAC's are controlled by Serial Peripheral Interface (SPI) which is provided by a microcontroller unit (MCU).

The circuit components such as the LDO's, the programmable DAC's and the larger sized capacitors are mounted on a separate PCB, called DC board, as shown in FIGURE 5.30(c), while the TX chip, the RX chip and the sensor structure are mounted on the the other board, called sensor board. The separation of the circuit components into these two boards eliminates the risk of damaging the relatively fragile sensor structure while soldering the rest of the circuit components on the same board. As shown in FIGURE 5.30(a), besides the TX and the RX chips and the sensor structure, the sensor board also has the coaxial connectors for the control clocks and the RX I/Q outputs. The 10 nF NP0 decaps are placed as close to the chip as possible, approximately 5mm away from the chip, to maximize its bypass and backup functionality. Therefore they are soldered on the back side of the board, to avoid the crowded traces on the top side, as shown in FIGURE 5.30(b). Numerous solutions exist concerning the connection of the two boards. The DC voltages provided by the LDO's and the DAC's from the DC board can be fed to the sensor board through simple jump wires, twisted pairs, PCI(Peripheral Component Interconnect) connectors, and etc. Finally, stacked PCB connection by pin header connectors is chosen, based on the following advantages. First, it minimizes the physical length of the connections between the two boards, which minimizes the potential EMI issues analyzed in the previous subsection. It also helps reduce ground loops formed by the ground connection between the two boards, improving signal integrity compared to connecting the two boards by other wires connections. Secondly, its vertical form

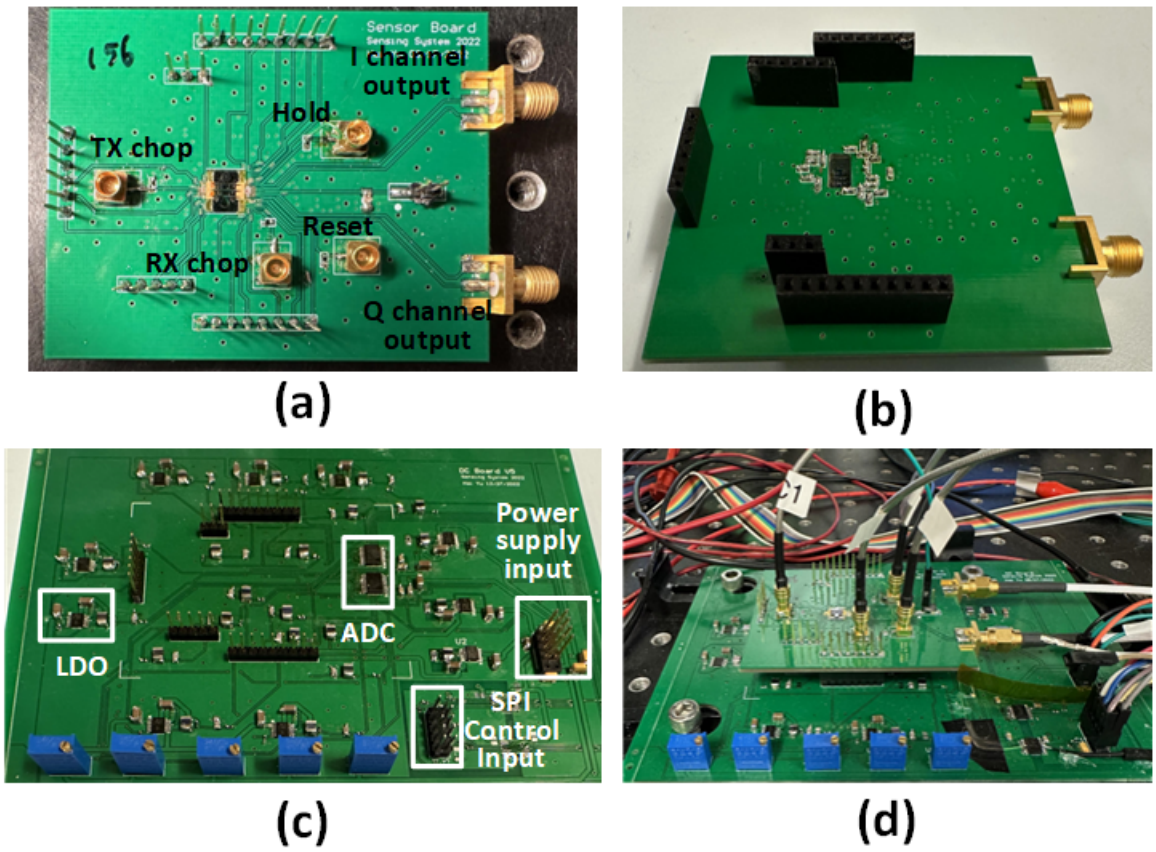

FIGURE 5.30. PCB of the sensing system. (a) Sensor board and notations of interconnections. (b) Back of the sensor board, showing 10nF decaps closely surrounding the chip areas. (c) DC board. (d) Two boards stacked up with pin header connections.

makes the entire system more compact. Lastly, the physical position of the sensing board is fixed with the DC board, making the entire system more physically stable and robust and hence less noise/uncertainty prone. The fully connected PCB in work mode is shown in FIGURE 5.30(d). To ensure a low noise output, the quality of the circuit ground is important. A noisy ground can corrupt a clean signal. To have a clean ground, it is a common practice to separate analog ground (GNDA) and digital ground (GNDD), because GNDD is usually much more noisy due to the fast transitions and current surges of the digital signals. With this consideration, the the ground associated with the SPI communication from the MCU, which is labelled as GNDD, is isolated from the ground of the rest of the board (GNDA). As can be seen from FIGURE 5.30(c), GNDD forms an island at the lower right corner of the DC board, forming a Galvanic isolation with GNDA. The

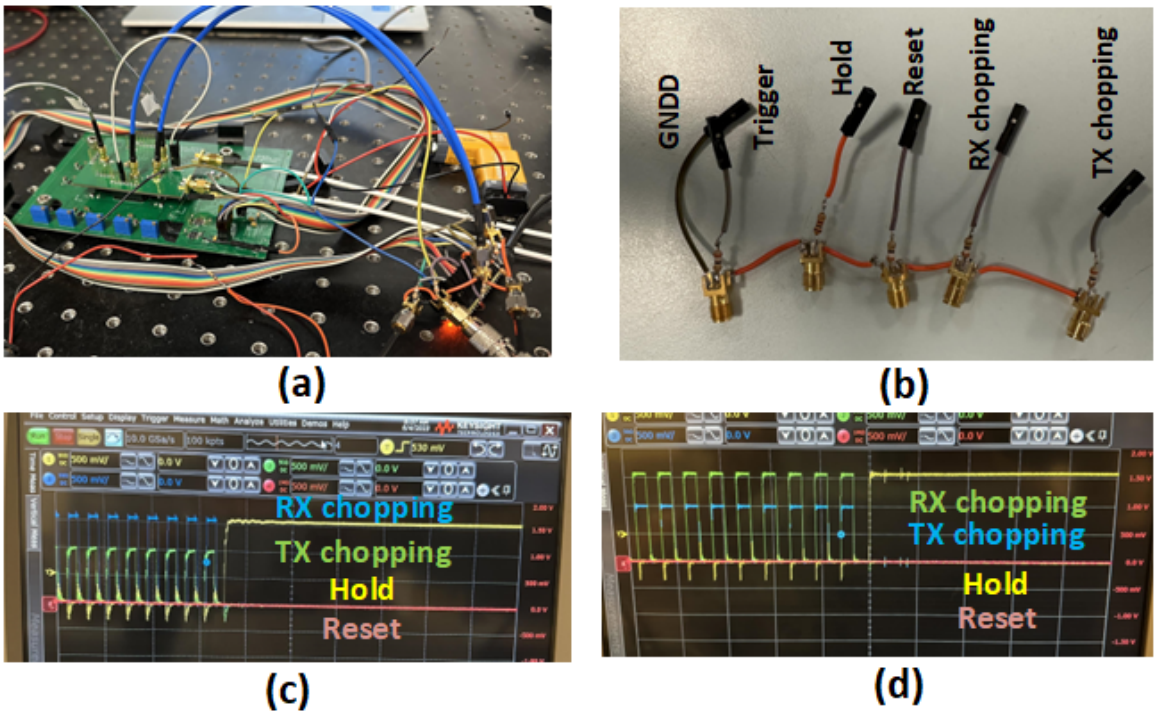

FIGURE 5.31. MCU control signal integrity (a) MCU provides SPI control and DC voltages to the DC boards through jump wires and the clocks to the sensor board through coaxial cables. (b) Series resistors soldered to the SMA connectors to suppress reflections in the coaxial cables. (c) Clock signals at the inputs of the chips without series resistors. (d) Clock signals at the inputs of the chips with series resistors.

SPI communication signals are then transmitted from the island to the DAC's through two digital isolators ADuM1440.

The control clocks of the TX and RX are directly fed to the sensor board through coaxial connectors. 50 Ohms shunt resistors are placed near the connector output pin to provide proper termination of the clocks to prevent reflections. Besides the general purpose function generators, the MCU that controls all the DC voltages of the TX and the RX chip can also provide the control clocks through its general purpose I/O (GPIO) pin. Thus, the entire sensing system's functionality can be controlled by a single MCU, which makes the sensing system prototype portable, convenient for live demonstrations. The MCU used for the sensing system control is a Teensy 4.0 Arduino, which can be seen from the lower right corner of FIGURE 5.31(a). To preserve the signal integrity of the control clocks, which are square waves with the frequencies upto 10 MHz and the rising and

FIGURE 5.32. (a) Live demo booth at the RFIC 2023. (b) Live demo at the SRC 2023 Annual Review.

falling edges of several nano seconds, coaxial cables are used to transmit the clock signals from the MCU to the sensor board. To connect the MCU's output pins to the coaxial cables, homemade pin header to SMA connector transitions are used, as shown in FIGURE 5.31(b). From the picture, it can also be seen that series resistors are also inserted in the transition to suppress reflections in the coaxial cables. The resistor values vary from 50 Ohms to 130 Ohms, which also help adjust the high level voltages of the clocks for the TX chip (0.9 V) and the RX chip (1.8 V). The clock signals at the sensor board without and with the series resistors are shown in FIGURE 5.31(c) and (d), respectively. Without the series resistors, the gradual transitions and the ripples actually prevents the chips from working properly. After adding the series resistors, the clock waves are much tidier and the sensing system works properly. Besides the control clocks that fed to the sensor board to control the chips, a trigger which is a duplicate of the hold clock is sent to the output sampling device, to make sure that the sensing system's output is sampled right after the integration time ends and the hold time begins.

It is also observed that, when using the MCU to provide the control clocks for the TX and RX chips, the system output signals from the I/Q paths are noisier comparing to the case when the desktop function generators are used to provide to clocks to the chips. There are two possible reasons. First, the ground of the MCU, which is considered to be noisy due to the constant digital operations on the MCU board, is directly connected to the analog ground of the sensor board,

breaking the Galvanic isolation between GNDA and GNDD. The ground noise from the MCU may have polluted the system's output signals. On the other hand, the desktop function generators are considered to have a much better ground thanks to its size, comparing to the small MCU board, whose ground is provided by the control laptop through a half-meter USB cable. Secondly, the function generator can provides a simple sine wave as the chopping clock to the sensor boards, and the inverters on the TX and the RX chips can convert the sine wave into square waves as the chopping signal. In contrast, Teensy MCU's GPIO can only provide square waves for the chopping clocks with required frequency of 10 MHz. The fast transition of the square waves may corrupt the output signals through the EM coupling between traces. This serves as the trade-off between the portability of the prototype system and its performance. Nevertheless, the sensing system is live demonstrated successfully in Radio Frequency Integrated Circuit Symposium (RFIC) 2023 and Semiconductor Research Corporation (SRC) CogniSense Center 2023 Annual Review, as shown in FIGURE 5.32.

5.5. Measurement Results

The measurement setup is shown in FIGURE 5.33. Rogers microwave circuit board substrates are placed on top of the sensors of the sensing and reference path as MUT samples. The samples are of the same dimensions as in the simulations shown in FIGURE 3.12. A Teensy Arduino micro-control unit (MCU) is sufficient to provide all the clocking and control signals for the TX and RX. The TX's output frequency is controlled by V_{cont}, which is swept in each sample measurement. The 10 MHz chopping clock is provided by the MCU to both the TX and RX. The hold and the reset clock of the RX's integrator are also provided by the MCU to control the integration time. The hold and reset clocks are set to have a frequency of 50kHz. With 70% duty cycle, which gives an integration time of 14us.

The output waveform of I path $V_{out,I}$ is observed by oscilloscope, as shown in FIGURE 5.34. The output waveform (yellow curve) of 4 cycles of integration are shown together with the hold clock(green curve), when the V_{cont} and therefore TX frequency is constant. The RX outputs $V_{out,I}$ and $V_{out,Q}$ are sampled by the data acquisition module NI DAQ9174, whose sampling is triggered by the rising edge of the hold clock of the RX to make sure the output voltages are sampled at the end of

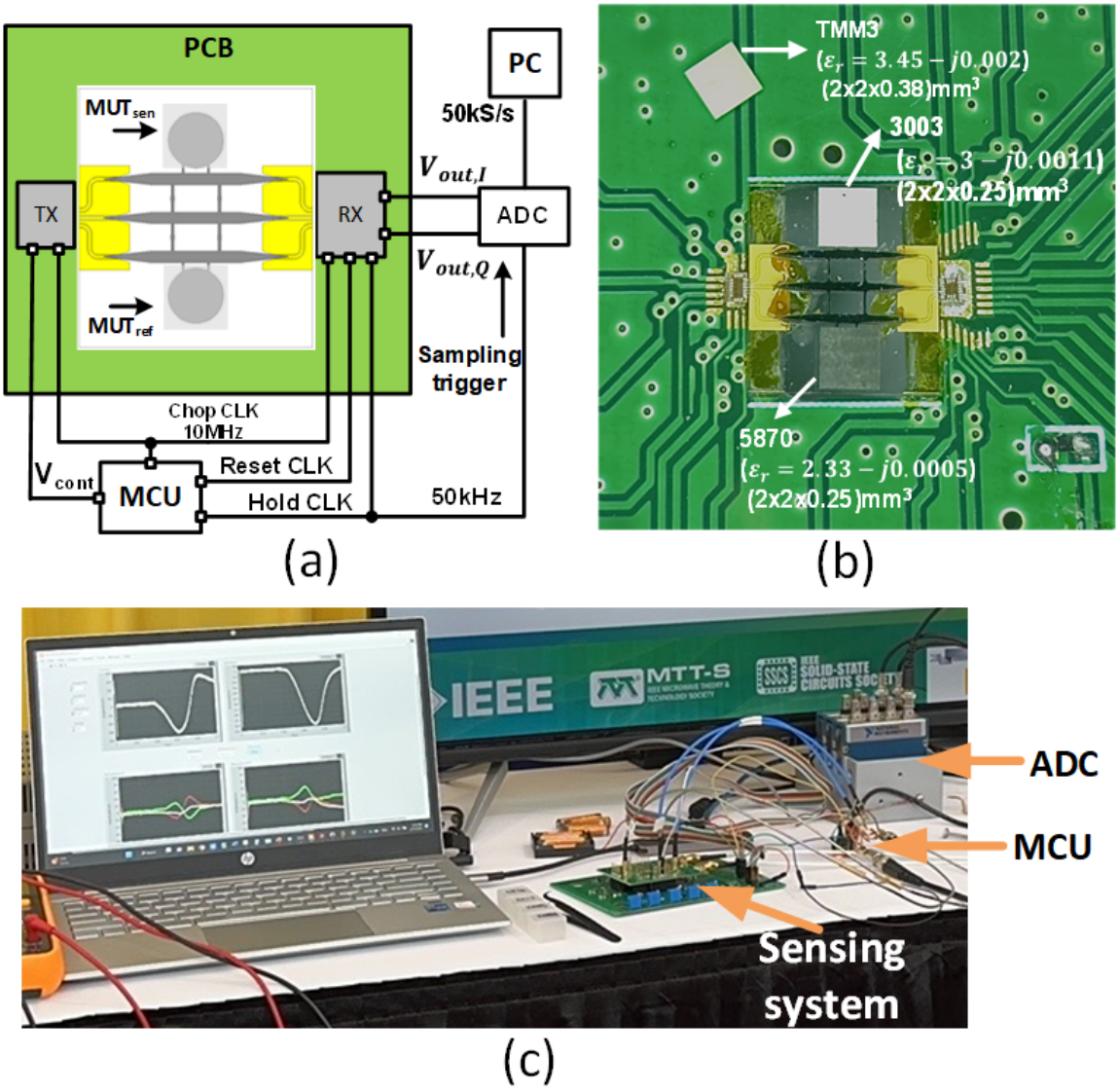

FIGURE 5.33. Measurement setup (a) Block diagram. (b) Top view of the sensing area with MUT samples placed on top of the sensors in the progress of measurement. (c) Photo of the measurement setup

each integration cycle. $V_{out,I}$ and $V_{out,Q}$ are then used to construct the ΔS_{21} of different dielectric samples placed on top of the sensors of the sensing and reference paths, as shown in FIGURE 5.34(b). In FIGURE 5.34(b), V_{cont} is swept from 380mV to 880mV to obtain the transmission difference waveform of the sensing and reference paths when different MUT samples are placed on the sensors in the frequency range of 157 GHz - 161 GHz. The relative sweeping speed of V_{cont}

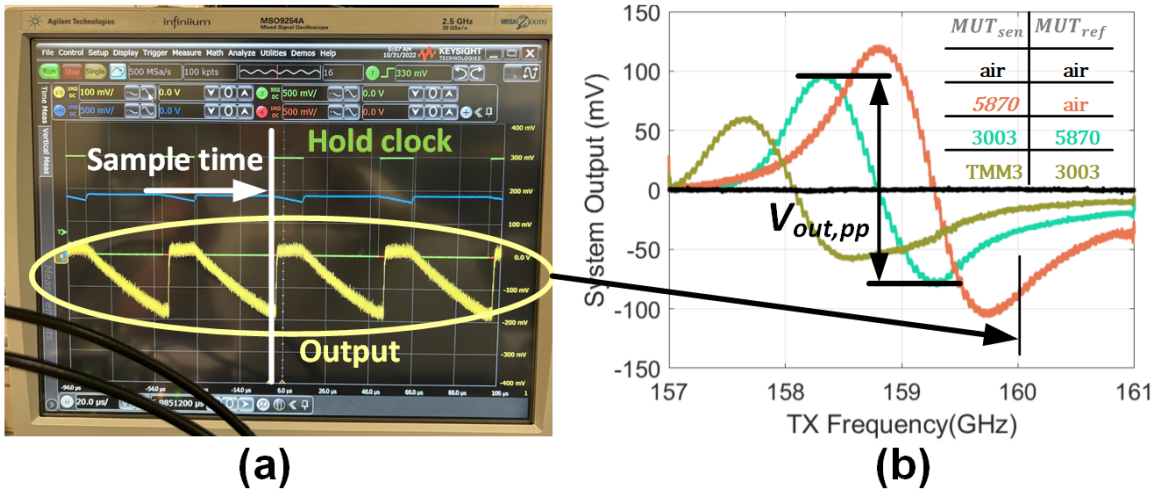

FIGURE 5.34. Sensing system output observed in (a) oscilloscope and (b) PC through the ADC

is adjustable. In the measurement shown in FIGURE 5.34(b), V_{cont} is swept from 380 mV to 880 mV in the step of 5 mV, and stays constant for 20 ms in each step, allowing the ADC to take 1000 samples at each frequency point. And therefore, the measurement of each curves in FIGURE 5.34 takes a total of 2 s. If higher throughput is required, one round of complex permittivity measurement can be finished for less than 2 ms, with only one sample taken at each frequency point. When V_{cont} is swept from 380 mV to 880 mV in the step of 5 mV, the TX frequency is swept in steps of approximately 8 MHz. The approximation is due to the fact that the TX frequency does not change with V_{cont} in an absolutely linear fashion, as shown in FIGURE 5.14. However, this nonlinear relationship between the TX frequency and V_{cont} is readily calibrated out by curving the sweeping step accordingly in the measurement.

FIGURE 5.35 shows the system outputs when the Rogers 5870 samples of different thickness are placed on the sensing and reference paths. Simulation results from FIGURE 3.12(b) are also plotted in the same figure against the measurement results. These measurements emulate the permittivity measurement process of an unknown MUT sample by comparing its transmission difference with the simulation result when the reference MUT on the reference path is the known MUT Rogers 5870 with the same thickness.

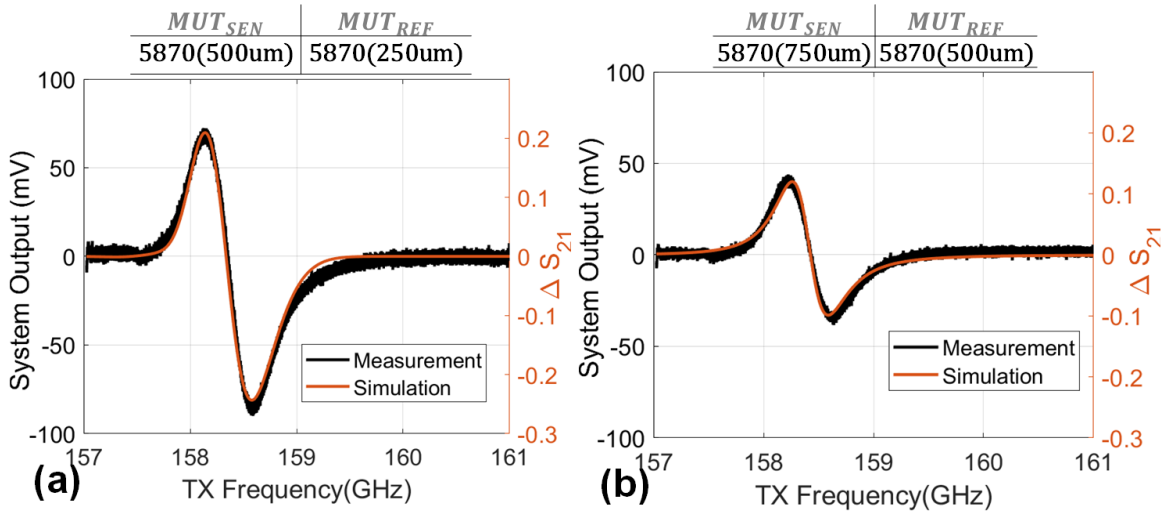

FIGURE 5.35. Sensing system output with different thickness of Rogers 5870 samples placed on the sensors. (a) 500um-thick 5870 vs. 250um-thick 5870. (b) 750um-thick 5870 vs. 500um-thick 5870.

To determine the sensing system's noise floor, the system output is measured for 10 s, for a total of 500k samples at sampling rate of 50kS/s. As shown in FIGURE 5.36, the system's output noise, especially the low frequency noise is significantly suppressed when the system chopping clock is turned on. The rms of the total system output noise is determined by taking the standard deviation of the 500k samples, which is 0.45 mV. The SNR of the measurements can be calculated by

$$SNR = \frac{V_{out,pp}^2}{v_{n,out}^2} \tag{5.23}$$

where $V_{out,pp}$ is the peak-peak voltage of the system output due to permittivity difference between the sensing and the reference path, and $v_{n,out}$ is the rms voltage of the system output noise.

The relative permittivity sensing resolution of the sensing system are calculated by dividing the normalized permittivity difference of the measured samples that causes the $V_{out,pp}$ by the square root of the resulting SNR:

$$\delta_{\epsilon_r} = \frac{\widehat{\Delta\epsilon_r}}{\sqrt{SNR}} \tag{5.24}$$

For example, a sensing resolution of 0.05% is found by a 14.0% permittivity difference between the Rogers TMM3 and Rogers 3003 samples divided by the resulting $\sqrt{SNR}$ of 263. The 5 cases of

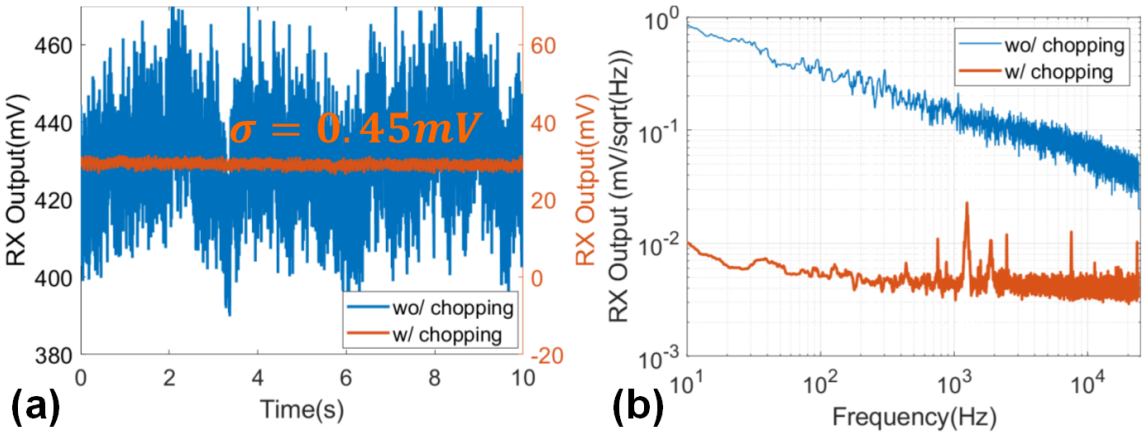

FIGURE 5.36. System output noise and noise suppression effect of the chopping. (a)Time domain output noise. (b)Spectral density of (a).

TABLE 5.1. Measurement Results Summary

Case	**1**	**2**	**3**	**4**	**5**
$\mathbf{MUT_{SEN}}$	5870	3003	TMM3	5870 (500um)	5870 (750um)
$\mathbf{MUT_{REF}}$	Air	5870	3003	5870 (250um)	5870 (500um)
$\epsilon'_{r,SEN}$	2.33	3	3.45	2.77*	2.95*
$\epsilon'_{r,REF}$	1	2.33	3	2.33	2.77*
$\widehat{\Delta\epsilon'_r}\%$ **	79.9	25.1	14.0	17.3	6.3
$V_{PP}(mV)$	223.4	117.7	118.1	155.5	87.6
$v_{n,out}(mV)$	0.45	0.45	0.45	0.45	0.45
SNR	2.56×10^5	1.56×10^5	6.89×10^4	1.19×10^5	3.79×10^4
Resolution %	0.16	0.064	0.053	0.05	0.032

* Equivalent permittivity for sample with 250um thickness;

** The normalized permittivity difference $\widehat{\Delta\epsilon'_r} = \frac{\epsilon'_{r,SEN} - \epsilon'_{r,REF}}{(\epsilon'_{r,SEN} + \epsilon'_{r,REF})/2}$.

the measurement results in FIGURE 5.34(b) and FIGURE 5.35 are summarized in TABLE **??**. When the permittivity differences between the sensing and the reference paths are less than 20%, the average resolution of 0.05% can be achieved.

Table I compares this work with the prior arts. For typical sensing systems, resolution can always be improved by merely consuming more power or integrating the output signal for longer time. One typical example of the former is to add more amplifiers either at the front end or the base band. Governed by general physics law, the power consumption has a linear trade-off relation with the SNR. Namely, consuming twice the power can improve the SNR by two times. Similarly,

longer integration time can be achieved by adding larger integration capacitors to lower the noise filtering bandwidth or ENBW. The relationship between the integration time and the SNR is also linear. The derivation of Eqn. 5.15 also shows obedience of this general rule. Thus, to have a fair and more straightforward comparison, a sensor figure-of-merit is defined as

$$FoM = -10log(\delta_{\epsilon_r}^2 P_{DC} \tau_{int}) \tag{5.25}$$

where δ_{ϵ_r} is the permittivity sensing resolution, P_{DC} is the DC power consumption, and τ_{int} is the integration time. By comparing with the prior arts, this sensing system not only demonstrates the best sensing resolution, but also achieves the highest FoM factor. This means that the sensing system achieves higher sensing resolution and consumes less power and takes less measurement time, as can also be seen from TABLE 5.2. The primary contributor for the high FoM factor is the adoption and design of the high sensitivity WGM sensor. As can be seen from Eqn. 5.15, higher sensitivity of the permittivity sensor improves the system SNR, directly breaking the trade-off between the SNR and the power consumption and integration time. The high FoM can also be attributed to the careful system-level SNR analysis that guides system architecture design. The power consumption distribution is also designed to make sure that the power is utilized in the most efficient way in the systematic design point of view. The DC power consumption partition is shown in FIGURE 5.37. The TX consumes 24 mW of power and the RX consumes 30 mW. The on-chip signal generation (VCO) and the LO distribution (LO buffer and ILO) consumes a total of 61.2% of power. The signal amplification and processing consumes the rest of the 38.8%.

TABLE 5.2. Comparison with the State-of-the-Art Integrated Permittivity Sensor

	JSSC'16 [?]	**JSSC'20 [54]**	**TMTT'19 [?]**	**CICC'21 [?]**	**This Work**
Technology	65nm CMOS	180nm CMOS	65nm CMOS	45nm RFSOI	28nm CMOS
Frequency(GHz)	6.5/11/ 17.5/30	1.8/2.2	3-10	$\lambda =$ $1300nm$	154-160
Resolution(%)	0.8	0.3	0.2	0.08	0.05
Integration time(us)	10	1000	150	10000	14
Complex sensing	No	No	Yes	No	Yes
Integrated LO	Yes	Yes	Yes	No	Yes
Power consump.(mW)	65	77.7	64	128	54
FoM	103.8	108.4	104.2	90.9	127.2

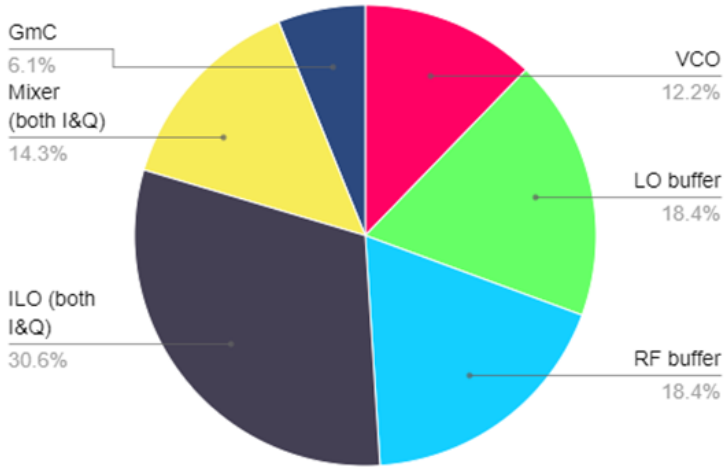

FIGURE 5.37. System DC Power Consumption Partition.

CHAPTER 6

Conclusion

6.1. Summary

In conclusion, this dissertation contributes significantly to the field of permittivity sensing, particularly in the context of CMOS technology and high-resolution applications. The exploration of sub-THz WGM resonator-based CMOS permittivity sensors represents a novel and promising approach, leveraging the benefits of compact form-factor, integration with CMOS transceivers, and enhanced sensitivity. The theoretical foundations laid for sensitivity optimization, coupled with the proposed novel mechanism for detecting complex permittivity, advance the understanding and capabilities of permittivity sensing systems.

The prototyped low-power permittivity sensing system at 160 GHz demonstrates remarkable performance with a permittivity sensing resolution of 3×10^{-4} for a short integration time of 10 µs and a minimal power consumption of 9 mW. Furthermore, the implemented high-resolution complex permittivity sensing system, utilizing a band-stop WGM disk resonator and innovative noise suppression techniques, achieves a record-breaking 0.05% complex sensing resolution within a 14-µs integration time, consuming only 54 mW of DC power. These achievements underscore the feasibility and efficiency of the proposed sub-THz WGM resonator-based CMOS permittivity sensing approach, offering new possibilities for high precision biosensing, precision medicine, and other applications demanding real-time, high-throughput measurements. The outcomes of this dissertation not only contribute to the academic understanding of permittivity sensing but also provide practical solutions that can be instrumental in diverse industries, fostering cost-effective and ubiquitous applications without compromising precision and accuracy.

6.2. Future Direction

The proposed high resolution permittivity sensing system establishes a platform for future sensing system with improved performance and expanded capabilities. The following are the three

possible directions.

First, the resolution of the sensing system can be further increased by adopting LNA's at the input of the RX, at the expense of higher DC power consumption. To mitigate the increased power consumption, passive mixer can be adopted instead of an active mixer. Secondly, the power consumption of the sensing system can be reduced by lowering the operating frequency to GHz, at the expense of larger form factors of the sensor. Finally, the dynamic range, namely the permittivity sensing range can be expanded by adopting multi-ring design. With multiple rings at different resonant frequencies, the sensing system should be capable of detecting materials with arbitrarily large permittivity range.

APPENDIX A

Derivation of the Flicker Noise Reduction by Chopping Technique

The following derivation verifies the flicker noise contribution at the RX output near DC (within ENBW, that is $f <$ ENBW) after the chopper by modeling the chopping process as frequency domain convolution with the harmonics of the square wave.

$$v^2_{1/f,out}(f) = v^2_{1/f,in}(f) * H^2_{chop}(f)$$

$$v^2_{1/f,out}(f) = \frac{k}{f} * 2\sum_{n=1}^{\infty}\left[\frac{2}{(2n-1)\pi}\right]^2 \delta[f + (2n-1)f_{chop}]$$

$$v^2_{1/f,out}(f) = \int_{-\infty}^{\infty}\frac{k}{\nu}\cdot 2\sum_{n=1}^{\infty}\left[\frac{2}{(2n-1)\pi}\right]^2 \cdot \delta[\nu - (f + (2n-1)f_{chop})]df \tag{A.1}$$

By sifting property of the dirac delta function, we get

$$v^2_{1/f,out}(f) = 2\sum_{n=1}^{\infty}\left[\frac{2}{(2n-1)\pi}\right]^2 \frac{k}{f + (2n-1)f_{chop}}$$

$$v^2_{1/f,out}(f) = 2\left(\frac{2}{\pi}\right)^2 \frac{k}{f + f_{chop}} + 2\left(\frac{2}{3\pi}\right)^2 \frac{k}{f + 3f_{chop}} + 2\left(\frac{2}{5\pi}\right)^2 \frac{k}{f + 5f_{chop}} + ... \tag{A.2}$$

when $f << f_{chop}$, which is the case when $f < 20kHz$ after chopping

$$v^2_{1/f,out}(f) = 2\left(\frac{2}{\pi}\right)^2 \frac{k}{f_{chop}} + 2\left(\frac{2}{3\pi}\right)^2 \frac{k}{3f_{chop}} + 2\left(\frac{2}{5\pi}\right)^2 \frac{k}{5f_{chop}} + ... \approx= 2\left(\frac{2}{\pi}\right)^2 \frac{k}{f_{chop}} = \frac{8}{\pi^2}\frac{k}{f_{chop}} \tag{A.3}$$

APPENDIX B

Derivation of Signal and Noise Processing of the Gm-C Integrator

This Appendix subsection shows the derivation of the transfer function of the Gm-C integrator. The output voltage across the integration capacitor after the integration finishes($t > t_{int}$) can be expressed as

$$V_{out}(t) = \frac{1}{C_{int}} \int_0^{t_{int}} G_m \cdot Vin(\tau) - \frac{V_{out}(\tau)}{R_{out}} d\tau \tag{B.1}$$

In order to derive the frequency domain transfer function, some manipulation is needed before performing the Laplace transformation:

$$V_{out}(t) + \frac{1}{C_{int}} \int_0^{t_{int}} \frac{V_{out}(\tau)}{R_{out}} d\tau = \frac{1}{C_{int}} \int_0^{t_{int}} G_m \cdot Vin(\tau) d\tau \tag{B.2}$$

$$\begin{aligned} &V_{out}(t) + \frac{1}{C_{int}} \left[\int_0^{t} \frac{V_{out}(\tau)}{R_{out}} d\tau + \int_t^{t_{int}} \frac{V_{out}(\tau)}{R_{out}} d\tau \right] = \\ &\frac{1}{C_{int}} \left[\int_0^{t_{int}} G_m \cdot Vin(\tau) d\tau + \int_t^{t_{int}} G_m \cdot Vin(\tau) d\tau \right] \end{aligned} \tag{B.3}$$

$$\begin{aligned} &V_{out}(t) + \frac{1}{C_{int} R_{out}} \left[\int_0^{t} V_{out}(\tau) d\tau - \int_{t_{int}}^{t} V_{out}(\tau) d\tau \right] = \\ &\frac{G_m}{C_{int}} \left[\int_0^{t_{int}} Vin(\tau) d\tau - \int_{t_{int}}^{t} Vin(\tau) d\tau \right] \end{aligned} \tag{B.4}$$

Using the convolution property of Heaviside function $x(t) * u(t) = \int_0^t x(\tau) d\tau$, the above equation can be written as

$$\begin{aligned} &V_{out}(t) + \frac{1}{C_{int} R_{out}} \left[V_{out}(t) * u(t) - V_{out}(t) * u(t - t_{int}) \right] = \\ &\frac{G_m}{C_{int}} \left[V_{in}(t) * u(t) - V_{in}(t) * u(t - t_{int}) \right] \end{aligned} \tag{B.5}$$

$$V_{out}(t) + \frac{V_{out}(t)}{C_{int}R_{out}} * [u(t) - u(t - t_{int})] = \frac{G_m}{C_{int}} V_{in}(t) * [u(t) - u(t - t_{int})] \tag{B.6}$$

Performing Laplace transformation:

$$V_{out}(s) + \frac{V_{out}(s)}{C_{int}R_{out}} \left[\frac{1}{s} - \frac{e^{-st_{int}}}{s}\right] = \frac{G_m}{C_{int}} V_{in}(s) \left[\frac{1}{s} - \frac{e^{-st_{int}}}{s}\right] \tag{B.7}$$

$$\begin{aligned} H_{GmC}(s) &= \frac{V_{out}(s)}{V_{in}(s)} \\ &= \frac{GmR_{out}(1 - e^{-st_{int}})}{1 - e^{-st_{int}} + R_{out}sC_{int}} \end{aligned} \tag{B.8}$$

For an ideal Gm-C integrator, the output resistance R_{out} approaches infinity, and (B.8) becomes

$$H_{GmC}(s) = \frac{G_m(1 - e^{-st_{int}})}{sC_{int}} \tag{B.9}$$

The magnitude of its transfer function is given by

$$|H_{G_mC}(j\omega)| = \left|\frac{G_m(1 - e^{-j\omega t_{int}})}{C_{int}j\omega}\right| = \frac{2G_m sin(\frac{\omega t_{int}}{2})}{C_{int}\omega}$$

which can also be expressed as

$$|H_{G_mC}(j2\pi f)| = \frac{G_m t_{int}}{C_{int}} \cdot \frac{sin(t_{int}\pi f)}{t_{int}\pi f}. \tag{B.10}$$

(B.10) predicts the transfer function of an ideal Gm-C integrator to be a sinc function with the DC gain of $G_m t_{int}/C_{int}$ and the first null bandwidth of $1/t_{int}$. It follows that, to have a higher signal gain, the Gm-C integrator should be designed to have a higher G_m, and a lower C_{int} for a fixed integration time t_{int}. On the other hand, for a fixed G_m and C_{int}, longer integration time t_{int} also gives a higher gain, and a lower bandwidth at the same time. The transfer function of an ideal Gm-C integrator (B.10) is plotted in Fig. 5.21 (a), in contrast with a practical Gm-C integrator with a finite output resistance R_{out} in Fig. 5.21 (b).

When a practical Gm-C integrator integrates for long enough time ($|e^{-st_{int}}| \ll 1$), (B.8) can be approximated as

$$H_{GmC}(s) \approx \frac{G_m R_{out}}{1 + R_{out}sC_{int}}, \tag{B.11}$$

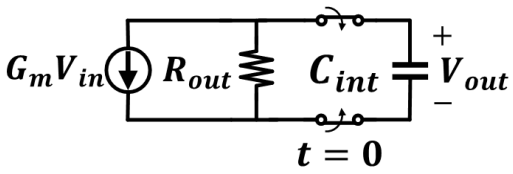

FIGURE B.1. Start of integration.

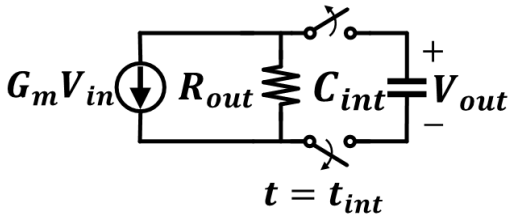

FIGURE B.2. Finish of integration.

which predicts a DC gain of $A_{V,GmC} = G_m R_{out}$, and a 3-dB bandwidth of $f_{3dB} = 1/(2\pi R_{out} C_{int})$. Comparing with (B.10), R_{out} sets the limits for the DC gain and the bandwidth which can no longer be improved by longer integration time, which is shown in Fig. 5.21 (b) and results in the saturation behaviors of the signal and noise in Fig. 5.10. Eqn. B.11 can be expressed in terms of frequency f

$$H_{gmC}(f) \approx \frac{GmR_{out}}{1 + j2\pi f R_{out} C_{int}} \tag{B.12}$$

which can be further re-write as

$$H_{gmC}(f) = A_{V,gmC} \frac{1}{1 + \frac{jf}{f_{3dB}}} \tag{B.13}$$

To facilitate the derivation of the sensing system SNR and resolution, the integration of $H_{gmC}(f)$ over frequencies band of interest can be expressed as

$$\int_{f_L}^{f_H} |H_{gmC}(f)| df \approx A_{V,gmC} ENBW \tag{B.14}$$

where $ENBW = 1.57 f_{3dB}$ is the equivalent noise bandwidth of the GmC integrator when integrated for long enough time ($|e^{-st_{int}}| \ll 1$).

Bibliography

[1] B. Yu, Y. Liu, Y. Ye, J. Ren, X. Liu, and Q. J. Gu, "High-efficiency micromachined sub-thz channels for low-cost interconnect for planar integrated circuits," *IEEE Transactions on Microwave Theory and Techniques*, vol. 64, no. 1, pp. 96–105, 2016.

[2] B. Yu, Y. Liu, Y. Ye, X. Liu, and Q. J. Gu, "Low-loss and broadband g-band dielectric interconnect for chip-to-chip communication," *IEEE Microwave and Wireless Components Letters*, vol. 26, no. 7, pp. 478–480, 2016.

[3] S. J. Orfanidis, "Electromagnetic waves and antennas."

[4] K. Entesari, A. A. Helmy, and M. Moslehi-Bajestan, "Integrated Systems for Biomedical Applications: Silicon-Based RFMicrowave Dielectric Spectroscopy and Sensing," *IEEE Microw. Mag.*, vol. 18, no. 5, pp. 57–72, July-Aug, 2017.

[5] Y. Wang, H. Li, Z. Cao, T. Yu, Q. Shen, and Y. He, "Oscillating wave sensor based on the Goos–Hänchen effect," *Applied Physics Letters*, vol. 92, no. 6, p. 061117, 2008.

[6] Z. Wang and D. J. Bornhop, "Dual-capillary backscatter interferometry for high-sensitivity nanoliter-volume refractive index detection with density gradient compensation," *Analytical chemistry*, vol. 77, no. 24, pp. 7872–7877, 2005.

[7] R. Heideman and P. Lambeck, "Remote opto-chemical sensing with extreme sensitivity: design, fabrication and performance of a pigtailed integrated optical phase-modulated Mach–Zehnder interferometer system," *Sensors and Actuators B: Chemical*, vol. 61, no. 1-3, pp. 100–127, 1999.

[8] N. M. Hanumegowda, C. J. Stica, B. C. Patel, I. White, and X. Fan, "Refractometric sensors based on microsphere resonators," *Applied Physics Letters*, vol. 87, no. 20, 2005.

[9] C.-Y. Chao, W. Fung, and L. J. Guo, "Polymer microring resonators for biochemical sensing applications," *IEEE journal of selected topics in quantum electronics*, vol. 12, no. 1, pp. 134–142, 2006.

[10] A. Yalcin, K. C. Popat, J. C. Aldridge, T. A. Desai, J. Hryniewicz, N. Chbouki, B. E. Little, O. King, V. Van, S. Chu, *et al.*, "Optical sensing of biomolecules using microring resonators," *IEEE Journal of Selected Topics in Quantum Electronics*, vol. 12, no. 1, pp. 148–155, 2006.

[11] K. De Vos, I. Bartolozzi, E. Schacht, P. Bienstman, and R. Baets, "Silicon-on-Insulator microring resonator for sensitive and label-free biosensing," *Optics express*, vol. 15, no. 12, pp. 7610–7615, 2007.

[12] C. A. Barrios, K. B. Gylfason, B. Sánchez, A. Griol, H. Sohlström, M. Holgado, and R. Casquel, "Slot-waveguide biochemical sensor," *Optics letters*, vol. 32, no. 21, pp. 3080–3082, 2007.

[13] X. Fan, I. M. White, S. I. Shopova, H. Zhu, J. D. Suter, and Y. Sun, "Sensitive optical biosensors for unlabeled targets: A review," *analytica chimica acta*, vol. 620, no. 1-2, pp. 8–26, 2008.

[14] H. Tazawa, T. Kanie, and M. Katayama, "Fiber-optic coupler based refractive index sensor and its application to biosensing," *Applied Physics Letters*, vol. 91, no. 11, 2007.

[15] O. Elhadidy, S. Shakib, K. Krenek, S. Palermo, and K. Entesari, "A wide-band fully-integrated CMOS ring-oscillator PLL-based complex dielectric spectroscopy system," *IEEE Transactions on Circuits and Systems I: Regular Papers*, vol. 62, no. 8, pp. 1940–1949, 2015.

[16] J.-C. Chien and A. M. Niknejad, "Design and analysis of chopper stabilized injection-locked oscillator sensors employing near-field modulation," *IEEE Journal of Solid-State Circuits*, vol. 51, no. 8, pp. 1851–1865, 2016.

[17] ——, "Oscillator-based reactance sensors with injection locking for high-throughput flow cytometry using microwave dielectric spectroscopy," *IEEE Journal of Solid-State Circuits*, vol. 51, no. 2, pp. 457–472, 2015.

[18] M. Elkholy and K. Entesari, "A Wideband Low-Power LC-DCO-Based Complex Dielectric Spectroscopy System in 0.18-um CMOS," *IEEE Transactions on Microwave Theory and Techniques*, vol. 65, no. 11, pp. 4461–4474, 2017.

[19] M. M. Bajestan, A. A. Helmy, H. Hedayati, and K. Entesari, "A 0.62–10 GHz complex dielectric spectroscopy system in CMOS," *IEEE Transactions on Microwave Theory and Techniques*, vol. 62, no. 12, pp. 3522–3537, 2014.

[20] M. Bakhshiani, M. A. Suster, and P. Mohseni, "A broadband sensor interface IC for miniaturized dielectric spectroscopy from MHz to GHz," *IEEE Journal of Solid-State Circuits*, vol. 49, no. 8, pp. 1669–1681, 2014.

[21] A. P. Saghati, J. S. Batra, J. Kameoka, and K. Entesari, "A metamaterial-inspired wideband microwave interferometry sensor for dielectric spectroscopy of liquid chemicals," *IEEE Transactions on Microwave Theory and Techniques*, vol. 65, no. 7, pp. 2558–2571, 2017.

[22] B. Laemmle, K. Schmalz, C. Scheytt, R. Weigel, and D. Kissinger, "An integrated 125GHz Sensor with read-out circuit for permittivity measurement of liquids," in *2012 IEEE/MTT-S International Microwave Symposium Digest*. IEEE, 2012, pp. 1–3.

[23] P. H. Siegel, "Terahertz technology," *IEEE Transactions on microwave theory and techniques*, vol. 50, no. 3, pp. 910–928, 2002.

[24] R. Han, Z. Hu, C. Wang, J. Holloway, X. Yi, M. Kim, and J. Mawdsley, "Filling the gap: Silicon terahertz integrated circuits offer our best bet," *IEEE Microwave Magazine*, vol. 20, no. 4, pp. 80–93, 2019.

[25] O. Momeni and E. Afshari, "High power terahertz and millimeter-wave oscillator design: A systematic approach," *IEEE Journal of Solid-State Circuits*, vol. 46, no. 3, pp. 583–597, 2011.

[26] Y. Chen, R. Hu, J.-H. Yu, Y. Ye, Y. Zhu, X. Liu, S. Qiu, J. Chen, X. Liu, C. Domier, *et al.*, "110–140-ghz wide-if-band 65-nm cmos receiver design for fusion plasma diagnostics," *IEEE Microwave and Wireless Components Letters*, vol. 32, no. 6, pp. 631–634, 2022.

[27] S. Qiu and Y. Zheng, "Design of an electron optical system for a 263 ghz sheet beam twt," in *2023 24th International Vacuum Electronics Conference (IVEC)*. IEEE, 2023, pp. 1–2.

[28] J. Chen, H. Wang, and X. Liu, "A 310-ghz fundamental oscillator with 0.4-mw output power and 3.2

[29] H. Wang, J. Chen, J. T. S. Do, H. Rashtian, and X. Liu, "High-efficiency millimeter-wave single-ended and differential fundamental oscillators in cmos," *IEEE Journal of Solid-State Circuits*, vol. 53, no. 8, pp. 2151–2163, 2018.

[30] H. Afzal, C. Li, and O. Momeni, "A highly efficient 165-ghz 4fsk 17-gb/s transceiver system with frequency overlapping architecture in 65-nm cmos," *IEEE Journal of Solid-State Circuits*, 2023.

[31] X. Ding, H. Yu, S. Sabbaghi, and Q. J. Gu, "Design and analysis of a mode-coupler-based multimode multidrop si dielectric waveguide channel for sub-thz/thz interconnect," *IEEE Transactions on Microwave Theory and Techniques*, 2023.

[32] Y. Ye, B. Yu, and Q. J. Gu, "A 165-ghz transmitter with 10.6% peak dc-to-rf efficiency and 0.68-pj/b energy efficiency in 65-nm bulk cmos," *IEEE Transactions on Microwave Theory and Techniques*, vol. 64, no. 12, pp. 4573–4584, 2016.

[33] Y. Yashchyshyn and K. Godziszewski, "A new method for dielectric characterization in sub-thz frequency range," *IEEE Transactions on Terahertz Science and Technology*, vol. 8, no. 1, pp. 19–26, 2017.

[34] D. Wang, J. Yun, M. Eissa, M. Kucharski, K. Schmalz, A. Malignaggi, Y. Wang, J. Borngräber, Y. Liang, H. Ng, *et al.*, "207-257 ghz integrated sensing readout system with transducer in a 130-nm sige bicmos technology," in *2019 IEEE MTT-S International Microwave Symposium (IMS)*. IEEE, 2019, pp. 496–499.

[35] K. D. Vos, I. Bartolozzi, E. Schacht, P. Bienstman, and R. Baets, "Silicon-on-insulator microring resonator for sensitive and label-free biosensing," *Opt. Express*, vol. 15, no. 12, pp. 7610–7615, Jun 2007. [Online]. Available: https://opg.optica.org/oe/abstract.cfm?URI=oe-15-12-7610

[36] H. Yu, B. Yu, X. Ding, J. S. Gómez-Díaz, and Q. J. Gu, "A 162 ghz ring resonator based high resolution dielectric sensor," in *2020 IEEE/MTT-S International Microwave Symposium (IMS)*, 2020, pp. 233–236.

[37] X. Ding, B. Yu, Y. Ye, H. Yu, Z. Xu, and Q. Jane Gu, "An fdd-based full-duplex sub-thz interconnect with data-rate of 22.6 gb/s and energy-efficiency of 1.58pj/bit," in *2021 46th International Conference on Infrared, Millimeter and Terahertz Waves (IRMMW-THz)*, 2021, pp. 1–2.

[38] S. A. Frank Vollmer, "Whispering-gallery-mode biosensing: label-free detection down to single molecules," *Nature Methods*, vol. 5, p. 591–596, 2008.

[39] R.G.Hunsperger, "Integrated optics," vol. ,6th ed., New York, NY, USA: Springer, 2009.

[40] D. M. Pozar, *Microwave engineering; 3rd ed.* Hoboken, NJ: Wiley, 2005. [Online]. Available: https://cds.cern.ch/record/882338

[41] N. M. Hanumegowda, C. J. Stica, B. C. Patel, I. White, and X. Fan, "Refractometric sensors based on microsphere resonators," *Applied Physics Letters*, vol. 87, no. 20, p. 201107, 11 2005. [Online]. Available: https://doi.org/10.1063/1.2132076

[42] X. Fu, G. Su, A. A. A. Apriyana, G. Feng, L.-l. Sun, and H. Yu, "A label-free and non-invasive cmos sub-thz plasmonic sensor for circulating tumor cell detection," in *2017 First IEEE MTT-S International Microwave Bio Conference (IMBIOC)*, 2017, pp. 1–4.

[43] S. Park, J. Hong, and S. e. a. Choi, "Detection of microorganisms using terahertz metamaterials," *Sci Rep*, vol. 4988, no. 4, p. 4988, May 2014.

[44] K. McClaning, *Wireless Receiver Design for Digital Communications*, ser. Telecommunications. Institution of Engineering and Technology, 2012. [Online]. Available: https://digital-library.theiet.org/content/books/te/sbte009e

[45] D. W. Vogt and R. Leonhardt, "Ultra-high Q terahertz whispering-gallery modes in a silicon resonator," *APL Photonics*, vol. 3, no. 5, p. 051702, May 2018, number: 5 Reporter: APL Photonics. [Online]. Available: http://aip.scitation.org/doi/10.1063/1.5010364

[46] I. M. White, H. Oveys, and X. Fan, "Liquid-core optical ring-resonator sensors," *Optics Letters*, vol. 31, no. 9, p. 1319, May 2006, number: 9 Reporter: Optics Letters. [Online]. Available: https://www.osapublishing.org/abstract.cfm?URI=ol-31-9-1319

[47] B. Little, S. Chu, H. Haus, J. Foresi, and J.-P. Laine, "Microring resonator channel dropping filters," *Journal of Lightwave Technology*, vol. 15, no. 6, pp. 998–1005, 1997.

[48] M. Z. U. Rahman, K. M. Krishna, K. K. Reddy, M. V. Babu, S. S. Mirza, and S. Y. Fathima, "Ultra-wide-band band-pass filters using plasmonic mim waveguide-based ring resonators," *IEEE Photonics Technology Letters*, vol. 30, no. 19, pp. 1715–1718, 2018.

[49] B. Laemmle, K. Schmalz, J. C. Scheytt, R. Weigel, and D. Kissinger, "A 125-GHz Permittivity Sensor With Read-Out Circuit in a 250-nm SiGe BiCMOS Technology," *IEEE Trans. on Microw. Theory and Techn.*, vol. 61, no. 5, pp. 2185–2194, 2013.

[50] A. Tang, Z. Xu, Q. J. Gu, Y.-C. Wu, and M. C. F. Chang, "A 144 GHz 2.5mW multi-stage regenerative receiver for mm-Wave imaging in 65nm CMOS," in *2011 IEEE Radio Freq. Integr. Circuits Symp.*, 2011, pp. 1–4.

[51] J.-Y. Chen, M. P. Flynn, and J. P. Hayes, "A Fully Integrated Auto-Calibrated Super-Regenerative Receiver in 0.13-μm CMOS," *IEEE J. of Solid-State Circuits*, vol. 42, no. 9, pp. 1976–1985, 2007.

[52] J. Li, A. More, S. Hao, and Q. J. Gu, "A 10 GHz Up-conversion Mixer with 13.6 dBm OIP3 Using Regulator-based Linearized Gm Stage and Harmonic Nulling," in *2018 IEEE/MTT-S International Microwave Symposium - IMS*, 2018, pp. 678–681.

[53] Y. Ye, B. Yu, and Q. J. Gu, "A 165 GHz OOK transmitter with 10.6% peak DC-to-RF efficiency in 65nm bulk CMOS," in *2016 IEEE MTT-S International Microwave Symposium - IMS*, 2016, pp. 1–4.

[54] J.-C. Chien, "A 1.8-ghz near-field dielectric plethysmography heart-rate sensor with time-based edge sampling," *IEEE Journal of Solid-State Circuits*, vol. 55, no. 3, pp. 615–628, 2020.

[55] S. Hao, T. Hu, and Q. J. Gu, "A 10-GHz Delay Line Frequency Discriminator and PD/CP-Based CMOS Phase Noise Measurement Circuit," *IEEE Trans. on Microw. Theory and Techn.*, vol. 65, no. 7, pp. 2361–2372, July 2017.

[56] S. A.-R. Ahmadi-Mehr, M. Tohidian, and R. B. Staszewski, "Analysis and Design of a Multi-Core Oscillator for Ultra-Low Phase Noise," *IEEE Trans. on Circuits and Syst. I: Regular Papers*, vol. 63, no. 4, pp. 529–539, April 2016.

[57] R. Kananizadeh and O. Momeni, "High-Power and High-Efficiency Millimeter-Wave Harmonic Oscillator Design, Exploiting Harmonic Positive Feedback in CMOS," *IEEE Trans. on Microw. Theory and Techn.*, vol. 65, no. 10, pp. 3922–3936, Oct. 2017.

[58] A. Ghorbani-Nejad, A. Nikpaik, A. Nabavi, A. H. Masnadi Shirazi, S. Mirabbasi, and S. Shekhar, "Optimum Conditions for Efficient Second-Harmonic Power Generation in mm-Wave Harmonic Oscillators," *IEEE Journal of Solid-State Circuits*, vol. 57, no. 7, pp. 2130–2142, July 2022.

[59] X. Yi, C. C. Boon, H. Liu, J. F. Lin, and W. M. Lim, "A 57.9-to-68.3 GHz 24.6 mW Frequency Synthesizer With In-Phase Injection-Coupled QVCO in 65 nm CMOS Technology," *IEEE J. of Solid-State Circuits*, vol. 49, no. 2, pp. 347–359, Feb. 2014.

[60] O. Memioglu, Y. Zhao, and B. Razavi, "A 300-ghz 52-mw cmos receiver with on-chip lo generation," *IEEE J. of Solid-State Circuits*, vol. 58, no. 8, pp. 2141–2156, 2023.

[61] D. B. Leeson, "Oscillator phase noise: A 50-year review," *IEEE Transactions on Ultrasonics, Ferroelectrics, and Frequency Control*, vol. 63, no. 8, pp. 1208–1225, 2016.